

Chapter One

Introduction

1.1. Introduction

In this chapter, a technological background is introduced. This includes the brief introduction of several key technologies, their great impact on the development of semiconductor lasers and an overview of the development of optically pumped vertical-external-cavity surface-emitting lasers. Based on the background, the motivation of the research work to be presented in this thesis is discussed. Finally the organization of this thesis is given. It contains the most important experimental results and analytical discussion of every chapter.

1.2. Technological background

Since the first report of the lasing action from a semiconductor laser, semiconductor lasers in different formats have been developed for more than 30 years and many of them have already been successfully transformed from laboratory devices only operating at cryogenic temperatures into commercial optoelectronic components capable of running continuously at room temperature. The great evolution is attributed to two main factors.

The first factor is the presence of many important optoelectronic applications. Because of the excellent properties, such as small size (several cubic millimeters), high efficiency (often as much as 50% or even more) and the long lifetime, semiconductor lasers have already entered into people's daily life. One major

application field of semiconductor lasers is the internet, which is based on optical fiber communication. By modulating the injection current of the lasers, gigahertz information transmission rates are now possible. Semiconductor lasers at 1.3 μm , where dispersion in the fiber is minimum, and at 1.5 μm , where optical fiber loss is minimum, thus experienced extensive development in order to quench the thirst for suitable laser sources. Another important application is the optical data storage devices. The world's hunger for high volume CD/DVD has driven the fast development of the laser devices at shorter wavelengths (from near infrared to blue). High power semiconductor lasers can be used in printers and photocopiers and even in many other areas such as line-of-sight communications, laser radar and fusing.

The second factor is the mature technologies on semiconductor growth and fabrications, which enable the possibility of growing high quality low dimensional semiconductor crystals for laser emission from ultraviolet to far infrared. In 1962, first semiconductor laser with p-n homojunctions was reported simultaneously by a number of laboratories [1-4]. However these early edge-emitting lasers had many problems, i.e. high threshold, low efficiency, pulsed output and only operating at cryogenic temperatures. In 1969, these problems were successfully solved after the first demonstration of an edge-emitting laser with heterostructure [5-6]. The growth of heterostructures was made possible by the crystal growth process of liquid phase epitaxy (LPE). LPE was an enabling technology for growing more complex but uniform structures which in turn lead to better carrier and optical confinement. This made continuous wave (CW) operation of edge-emitting lasers at room temperature possible. However, it was still difficult for growing uniform deposition over large area by using LPE. The small size of laser aperture significantly limited the maximum laser power. Large aperture laser structures with uniform material deposition was realised after the advent of two new growth technologies, metal organic chemical vapour deposition (MOCVD) and molecular beam epitaxy (MBE).

The direct effect of the conversion from LPE crystal growth technology to that of

MBE and MOCVD was the ability to control the crystal deposition to atomic layer accuracy and thereby the more advanced low dimensional heterostructures, such as quantum wells, strained quantum wells and quantum dots were used as gain media. These advanced gain structures are now widely employed in semiconductor lasers to greatly improve the laser performance, such as achieving much lower threshold and significant higher power.

Although edge-emitting lasers have been extensively developed and single edge-emitting laser now can give above 10W CW power at 970 nm [7] and about 0.4 W in a single transverse mode [8], there are still a few problems that set the limit for their applications. The heterosturcture gain region is transversely very thin for carrier confinement and laterally wide for output power. Hence this structure results in a highly astigmatic output beam, with full angle beam divergence of as much as 50° in the transverse dimension, which requires complex optics for collimation. The semiconductor wafer can not be characterised until most fabrication and packaging processes are finished since the facet mirrors are fabricated either by cleaving or etching. Lastly, it is hard to control the laser longitudinal modes. The cavity length of a typical edge-emitting laser is about 10^2 to $10^3 \lambda$. Hence it lases at multiple longitudinal modes. Although each of the above problems can be solved at least in part by designing special structures, the realization of those structures adds to the complexity and cost of the laser diodes.

Since the first proposition of a vertical-cavity surface-emitting laser (VCSEL), VCSELs by Iga in 1977, VCSELs have drawn much attention for the development and now have already replaced the traditional edge-emitting lasers in many areas. The structure of VCSEL is different from that of the edge-emitting semiconductor laser. The vertical cavity is formed by the surfaces distributed Bragg reflectors (DBR), and the laser output is taken from one of the DBR surfaces. The resonator axis of a VCSEL is in the vertical (epitaxial growth) direction which circumvents many problems arising from edge-emitting design. However the underlying principle

of operation of a VCSEL is the same as for an edge emitting laser. Both of them are electrically pumped. With the laser emission from the wafer surface, VCSELs can now have a symmetrical beam cross section. Furthermore, the very short cavity length (typically single wavelength thick), as compared with that of edge-emitting lasers (typically 300 μm and several μm in lateral size), not only makes VCSEL operation inherently single longitudinal mode, but also greatly reduce the lasing threshold which is directly proportional to the laser active volume [9]. Unlike an edge-emitting laser, the VCSEL mirrors are fabricated during the epitaxial growth and no cleaving or dry etching is required. The most significant limitation of the VCSEL is a lack of high power, with single transverse mode output typically less than 10 mW in conventional designs. This is due to the restricted lasing aperture (\sim 10 μm) which leads to relative low gain for the laser radiation. Higher power operation of VCESLs can be achieved by increasing the size of the emitting aperture. However this will excite higher order transverse modes. This drawback makes VCSELs unsuitable for the applications where both high power and good beam quality (diffraction limited circular beam profile) are needed, such as pumping fiber amplifiers in optical fiber communication industry or free space communications.

As a close cousin of VCSELs, vertical-external-cavity surface-emitting lasers (VECSELs) consist solely of the rear DBR and quantum well gain region. The top DBR of the VCSEL is replaced by an epitaxially grown antireflection (AR) coating and an additional external-cavity dielectric mirror as an output coupler. The standard cavity configuration is shown in Fig. 1.1.

The details on VECSEL operating principle and wafer design are discussed in Chapter Two. By optical pumping, VECSELs do not require p-n junctions or electrical contacts which significantly simplify growth and processing of the laser wafer and increases the device reliability. Also an un-doped semiconductor wafer will have much less optical losses caused by free carrier absorption [10]. As it can be easier to obtain uniform pumping at high carrier density over a large area in optically

pumped VECSELs than electrically injected VCSELs, VECSELs are potentially capable of generating higher laser power while the good beam quality can be kept due to the same surface emission design.

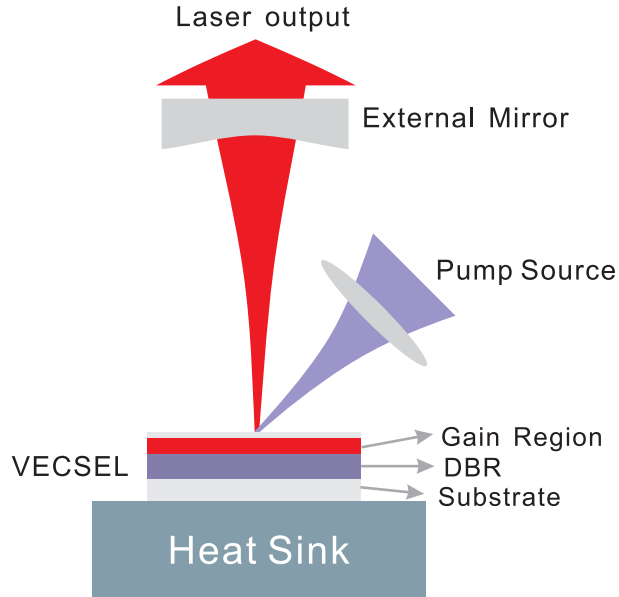


Fig. 1.1. Schematic setup of a optically pumped VECSEL.

Development of VECSEL

The first VECSEL operating at $1.5\mu\text{m}$ with both CW and mode locking operations was reported by WB Jiang et al. in 1991, where the InGaAs/InP multiple quantum well (MQW) gain region was grown on a gold-coated substrate and the CW laser power was 190mW at the operating temperature of 77K [11]. One year later, they demonstrated the first room temperature pulsed VECSEL which was based on GaAs/AlGaAs MQWs structure with rear DBR and synchronously pumped by a Nd:YAG laser [12]. In later years, continuous improvements have been made by their group for improving the performance of mode locked VECSELs [13-14]. In 1996, the first room temperature CW VECSEL based on GaAs/AlGaAs was reported by Sandusky et al [15]. However their device only delivered about $20\mu\text{W}$ with the incident pump power of 100mW. The thermal rollover of the output power was observed. Thermal effects in the gain region are believed responsible for the output

rollover, since no attempts have been made to heat sink the wafer beyond backside contact mounting to a copper block. In 1997, a landmark paper came out, where Kuznetsov et al. described the further improvements in VECSEL design, characterisation and operation of CW diode pumped VECSEL [16]. More than 0.5W average powers in a fundamental transverse mode beam were achieved. The thermal problems have been suppressed by employing the window-on-substrate structure, where the quantum wells were grown on the GaAs substrate and then the 30-layer DBR was grown over the quantum wells. Post processing is required to etch the substrate and solder the DBR side to a diamond heat sink. By using this technique, Chilla et al. [17] was able to generate a 30W high power 980nm VECSEL. This high power operation was realized at a price of relative low beam quality ($M^2=3$) due to the large pump spot (500-900 μm in diameter). The use of crystalline heatspreaders as a means of dissipating the heat in the VECSEL gain region was firstly reported by Alford and colleagues in 2002 [18], who obtained 1.5W output power with good beam quality. A sapphire heatspreader was optically contacted to the intra-cavity semiconductor surface by using the method of liquid capillary bonding [19].

In parallel with the power scaling, the external cavity allows the introduction of optical elements to control the laser output. The insertion of nonlinear crystals can realize intra-cavity frequency doubling and hence lead to the development of a new group of compact and visible sources. Since optically pumped VECSELS have a significant greater intra-cavity circulating power than the output power. This allows efficient intra-cavity frequency doubling of the laser power from the infrared into the visible wavelength range, especially in blue. The generation of 15W output power in a single longitudinal mode from a 488nm-VECSEL was reported by Chilla et al. at Coherent, who used an intra-cavity Type-I critically phase-matched Lithium Triborate (LBO) crystal with a multiple low brightness diode-array pumps [20]. Recently, a tunable watt-level blue-green VECSEL was demonstrated by Fan et al., who achieved over 1.3W CW blue-green power at 488nm with a 5nm tunability by

using LBO crystal [21]. The compact high power blue VECSELs have become the strong rival to the ion lasers and even replaced ion lasers in some applications.

The spectral bandwidth of VECSELs can be easily controlled by putting spectral narrowing elements (birefringent filter (BRF) and/or etalon) and thereby tunable single frequency laser sources are obtainable. Single frequency operations of VECSELs at 850nm and 980nm with high frequency stability (\sim 5kHz) have been reported by employing active locking techniques [22-23]

Moreover, the introduction of a semiconductor saturable absorber mirror (SESAM [24]) into the external cavity has led to the generation of some of the shortest pulse ever formed directly within a mode-locked semiconductor oscillator [25-26]. Owing to the great success of the invention of SESAM, passively mode locked VECSELs have been successfully developed, especially for the devices operating in $1\mu\text{m}$ wavelength region. Aschwanden and his colleagues have achieved 2.08W average output power in 4.7ps pulses at a repetition rate of 4GHz and 1.4W average output power in 6.1ps pulses at a repetition rate of 10GHz [28-29]. And the ongoing development is to push the repetition frequency to a much higher level (100GHz) while simultaneously improve the average output power of the mode locked VECSELs [30]. Although progress of passively mode locked VECSELs at wavelengths other than the $1\mu\text{m}$ region has not gained much momentum, first successful passive mode locking of an InP-based VECSEL operating at $1.5\mu\text{m}$ has been demonstrated with 13.5mW average output power in 6.5 ps pulses at a repetition rate of 1.34GHz [27]. These devices can possibly find their applications in laser display systems, optical clocking of integrated circuits.

Great efforts have also being made to search suitable material systems in order to extend the spectral coverage of the devices. The wavelengths and material systems developed for VECSELs so far, with references to the key results, are reviewed by Tropper et al [31] and summarised in Table 1.1. The VECSELs demonstrated in this

thesis are based on III-V semiconductors (InGaAs/GaAs and InAlGaAs/AlGaAs) for emission wavelengths in near infrared (980 nm and 850 nm).

Well/Barrier	DBR	Substrate	λ_{laser} (nm)	λ_{pump} (nm)
InGaN/GaN	SiO ₂ /HfO ₂	Al ₂ O ₃	390	335
InGaP	AlAs/AlGaAs	GaAs	660	514
AlGaAs/GaAs	AlGaAs/GaAs	GaAs	850-870	660-670
InGaAs/GaAsP	AlAs/GaAs	GaAs	960-1050	808, 830
GaInNAs/GaAs	AlAs/GaAs	GaAs	1320	810
InGaAs/InGaAsP	InAlAs/GaInAlAs InP/InGaAlAs Au layer	InP	1550	980, 1250
GaInAsSb/AlGaAsSb	GaSb/AlAsSb	GaSb	2300	830

Table 1.1. Material systems of gain region (well and barrier) and DBR for different spectral regions in which VECSELs have been fabricated, after [31]

1.3. Motivation

The research work presented in this thesis is concerned with the investigations of the different laser operations including active mode locking, single frequency and high power CW operation of the optically pumped VECSELs emitting in near infrared region.

Passively mode locked VECSELs always operate at high repetition frequencies and hence generate relatively low peak powers of the laser pulses. Active mode locking greatly reduces the repetition rate of the lasers and makes the generation of high peak power pulses from VECSELs possible. Short pulses with high peak power are attractive features in many applications such as nonlinear microscopy and nonlinear frequency conversion.

Because of their wavelength versatility and the inherent suitability for single mode operation, single frequency VECSELs can be developed to give high power narrow linewidth output at almost everywhere in the spectral region from far infrared to visible, which is difficult to achieve in the conventional solid state crystalline lasers. The narrow linewidth VECSELs are excellent laser sources for precision spectroscopic measurements.

980nm-VECSELs have already been well developed and the power of up to 30W is achieved. However VECSELs operating at other wavelength regions are still being developed. Besides the improvement of growth technologies, many other techniques can be employed to increase the laser output. Optical in-well pumping and multi-pass pump geometry are thus two of those techniques. In combination of these two techniques, high power 850nm-VECSEL is achieved.

1.4. Thesis outline

The structure of this thesis is organized in the following way.

Chapter Two firstly introduces the basic operation principle of the optically pumped VECSELs. This is followed by a detailed description on the design of the laser devices which includes the design of the MQW gain region, DBR mirror and the external laser cavity. The methods of thermal management are also discussed. Finally the mechanism of the optical in-well pumping is presented and the comparison between conventional barrier pumping and in-well pumping is discussed.

In Chapter Three, the theory of laser mode locking is presented. This includes a discussion of two main methods of the mode locking which are active mode locking and passive mode locking. Synchronous mode locking as a practical active mode locking technique is introduced. Since pulse duration is strongly affected by the dispersion, a good control of the laser dispersion is important. Therefore different techniques for dispersion management are presented.

Chapter Four presents the experimental results of synchronous mode locking of a

room temperature InGaAs/AlGaAs based VECSEL operating at ~980nm. The cavity detuning effects of the laser are studied and chirp compensation of the laser pulse is investigated. In the experiment, both fs pulse (70fs) and ps (3.6ps) pulse were used for synchronous pumping. The maximum average powers for fs pulse pumping and ps pulse pumping are 40mW and 27mW. The laser pulse duration was in the range of 10-40ps when the cavity length was detuned for both cases. And multiple pulsing was observed around the optimum cavity length. For ps pulse pumping, a negative dispersion was introduced by an extra-cavity grating pair and the duration of the compressed pulse was measured to be 185fs. The peak power was calculated to be 300W when 80MHz repetition rate of the laser was taken into account. For fs pulse pumping, laser pulses have different sign of dispersion for short cavity and long cavity. After compression, pulse duration of 244fs and 600fs were achieved by using a grating pair and an optical fiber respectively. The peak powers of both pulses were around 450W. The laser performance was also investigated when a BRF was inserted. The phenomenon of multiple pulses is much clearer and more strongly pronounced. The output pulse was shortened to be 2.7ps by employing a grating pair for the case of fs pumping.

Chapter Five is concerned with the development and characterisation of a room temperature InGaAs/AlGaAs based VECSEL operating at around 970nm. The physical mechanism of the spatial hole burning effect (SHB) is discussed. An introduction of a novel frequency stabilization technique based on a birefringent etalon is presented. Stable single mode operation was achieved by stabilizing intra-cavity birefringent etalon and at mean time locking the laser cavity to a Fabry-Perot interferometer (FPI). The maximum output power of the laser was 260mW. And a fine tuning range of 4GHz together with a coarse tuning range of 9nm was attained. The minimum laser linewidth was measured to be 45kHz. Much narrower linewidth can be expected by suppressing the electronic noises of the power supplies.

Chapter Six explores the possibility of the use of optical in-well pumping to decrease the thermal problems and hence increase laser power. This involves the characterisation of different laser chips and the optimization of the laser performance. Power degradation was observed in the lasers based on three new grown wafers. An old wafer which was designed for barrier pumping (described in Chapter Three) was instead characterised. The pump retro-reflection system was applied to increase the total pump absorption. After optimising the pumping angle, wavelength and laser operating temperature, a maximum power of 1.02W was achieved. The slope efficiency was measured to be 10.6%. Lastly, a discussion of the ways to improve laser efficiency in future design concludes the chapter.

A final conclusion of the presented work in this thesis is drawn in Chapter Seven. Major results together with an outlook of each experiment are also summarised.

1.5. Reference

- [1]. M. I. Nathan, W. P. Dumke, G. Burns, F. H. Dill Jr. and G. Lasher, "Stimulated emission of radiation from GaAs p-n junctions," Applied Physics Letters, Vol. 1, No. 3, pp. 62-64, 1962.
- [2]. R. N. Hall, G. H. Fenner, J. D. Kingsley, T. J. Soltys and R. D. Carlson, "Coherent light emission from GaAs junctions," Physical Review Letters, Vol. 9, No. 9, pp. 366-368, 1962.
- [3]. T. M. Quist, R. H. Rediker, R. J. Keyes, W. E. Krag, B. Lax, A. L. McWhorter and H. J. Zeiger, "Semiconductor maser of GaAs," Applied Physics Letters, Vol. 1, No. 4, pp. 91-92, 1962.
- [4]. N. Holonyak Jr. and S. Bevacqua, "Coherent (visible) light emission from Ga(As_{1-x}P_x) junctions," Applied Physics Letters, Vol. 1, No. 4, pp. , 83-83, 1962.
- [5]. I. Hiyashi, M. B. Panish and P. W. Foy, "A technique for the preparation of low-threshold room-temperature GaAs laser diode structures," IEEE Journal of Quantum Electronics, Vol. 5, No. 4, pp. 210-212, 1969.
- [6]. H. Kressel and H. Nelson, "Close-confinement gallium arsenide pn junction lasers with reduced optical loss at room temperature," RCA Review, Vol. 30, pp. 106-113, 1969.
- [7]. A. Al-Muhanna, L. J. Mawst, D. Botez, D. Z. Garbuzov, R. U. Martinelli, J. C. Connolly, "High-power (> 10 W) continuous-wave operation from 100-mu m-aperture 0.97-mu m-emitting Al-free diode lasers," Applied Physics Letters Vol. 73, No. 9, pp: 1182-1184, 1998.
- [8]. M Sagawa, T. Toyonaka, K. Hiramoto, K. Shinoda and K. Uomi, "High-power highly-reliable operation of 0.98-mu-m InGaAs-InGaP strain-compensated single-quantum-well lasers with tensile-strained InGaAsP barriers," IEEE Journal of Selected Topics in Quantum Electronics, Vol. 1, No. 2, pp. 189-195, 1995.
- [9]. H. Li, K. Iga, Vertical-Cavity Surface-Emitting Laser Devices, Springer-Verlag Berlin, 2002.

- [10]. L. J. Mawst, A. Bhattacharya, J. Lopez, D. Botez, D. Z. Garbuzov, L. DeMarco, J. C. Connolly, M. Jansen, F. Fang, and R. F. Nabiev, “8 W continuous wave front-facet power from broad-waveguide Al-free 980 nm diode lasers,” *Applied Physics Letters*, Vol. 69, No. 11, pp. 1532-1534, 1996.
- [11]. W. B. Jiang, S. R. Friberg, H. Iwamura, and Y. Yamamoto, “High powers and subpicosecond pulses from an external-cavity surface-emitting InGaAs/InP multiple quantum well laser,” *Applied Physics Letters*, Vol. 58, No. 8, pp. 807-809, 1991.
- [12]. W. B. Jiang, R. Mirin, and J. E. Bowers, “Mode-locked GaAs vertical cavity surface emitting lasers,” *Applied Physics Letters*, Vol. 60, No. 6, pp. 677-679, 1992.
- [13]. W. H. Xiang, S. R. Friberg, K. Watanabe, S. Machida, W. B. Jiang, H. Iwamura, and Y. Yamamoto, “Femtosecond external-cavity surface-emitting InGaAs/InP multiple-quantum-well laser,” *Optics Letters*, Vol. 16, No18, pp. 1394-1396, 1991.
- [14]. W. B. Jiang, M. Shimizu, R. P. Mirin, T. E. Reynolds, and J. E. Bowers, “Femtosecond Periodic Gain Vertical-Cavity Lasers,” *IEEE Photonics Technology Letters*, Vol. 5, No. 1, 1993.
- [15]. J. V. Sandusky, S. R. J. Brueck, “A CW external-cavity surface-emitting laser,” *IEEE Photonics Technology Letters*, Vol. 8, No. 3, pp. 313-315, 1996.
- [16]. M. Kuznetsov, F. Hakimi, R. Sprague, and A. Mooradian, “High-power (>0.5-W CW) diode-pumped vertical-external-cavity surface-emitting semiconductor lasers with circular TEM00 beams,” *IEEE Photonics Technology Letters*, Vol. 9, No. 8, pp. 1063-1065, 1997.
- [17]. J. Chilla, S. Butterworth, A. Zeitschel, J. Charles, A. Caparara, M. Reed, and L. Spinelli, “High power optically pumped semiconductor lasers,” *Solid State Lasers XIII: Technology and Devices*, Vol. 5332, pp. 143-150, 2004.
- [18]. W. J. Alford, T. D. Raymond, and A. A. Allerman, “” *Journal of Optical Society of America B-Optical Physics*, Vol. 19, No. 4, pp. 663-666, 2002.
- [19]. Z. L. Liau, “Semiconductor wafer bonding via liquid capillarity,” *Applied Physics Letters*, Vol. 77, No. 5, pp. 651-653, 2000.
- [20]. J. Chilla, S. Butterworth, A. Zeitschel, J. Charles, A. Caparara, M. Reed, and L. Spinelli, “High power optically pumped semiconductor lasers,” *Solid State Lasers XIII: Technology and Devices*, Vol. 5332, pp. 143-150, 2004.

- [21]. L. Fan, T. C. Hsu, M. Fallahi, J. T. Murray, R. Bedford, Y. Kaneda, J. Hader, A. R. Zakharian, J. V. Moloney, S. W. Koch, and W. Stoltz, “Tunable watt-level blue-green vertical-external-cavity surface-emitting lasers by intracavity frequency doubling,” *Applied Physics Letters*, Vol. 88, No. 25, pp. 251117, 2006.
- [22]. M. A. Holm, D. Burns, A. I. Ferguson, M. D. Dawson, “Actively Stabilized Single -Frequency Vertical-External-Cavity AlGaAs Laser,” *IEEE Photonics Technology Letters*, Vol. 11, No. 12, 1999.
- [23]. R. H. Abram, K. S. Gardner, E. Riis, and A. I. Ferguson, “Narrow linewidth operation of a tunable optically pumped semiconductor laser,” *Optics Express*, Vol. 12, No. 22, pp. 5434-5439, 2004.
- [24]. U. Keller, K. J. Weingarten, F. X. Kartner, D. Kopf, B. Braun, I. D. Jung, R. Fluck, C. Honninger, N. Matuschek, and Juerg Aus der Au, “Semiconductor saturable absorber mirrors (SESAM’s) for femtosecond to nanosecond pulse generation in solid-state lasers,” *IEEE Journal of Selected Topics in Quantum Electronics*, Vol. 2, No. 3, pp. 435-453, 1996.
- [25]. A. Garnache, S. Hoogland, A. C. Topper, I. Sagnes, G. Saint-Girons, and J. S. Roberts, “Sub-500-fs soliton-pulse in a passively mode-locked broadband surface-emitting laser with 100 mW average power,” *Applied Physics Letters*, Vol. 80, No. 21, pp. 3892-3894, 2002.
- [26]. S. Hoogland, A. Garnache, I. Sagnes, J. S. Roberts, and A. C. Tropper, “10-GHz Train of Sub-500-fs Optical Soliton-Like Pulses From a Surface-Emitting Semiconductor Laser,” *IEEE Photonics Technology Letters*, Vol. 17, No. 2, pp. 267-269, 2005.
- [27]. S. Hoogland, B. Paldus, A. Garnache, K. J. Weingarten, R. Grange, M. Haiml, R. Paschotta, U. Keller, and A. C. Tropper, “Picosecond pulse generation with a 1.5 μm passively mode locked surface emitting semiconductor laser,” *Electronics Letters*, Vol. 39, No. 11, pp. 846-847, 2003.
- [28]. A. Aschwanden, D. Lorenser, H. J. Unold, R. Paschotta, E. Gini, and U. Keller, “2.1- W picosecond passively mode-locked external-cavity semiconductor laser,” *Optics Letters*, Vol. 30, No. 3, pp. 272-274, 2005.
- [29]. Aschwanden, D. Lorenser, H. J. Unold, R. Paschotta, E. Gini, and U. Keller, “10 GHz passively mode-locked surface emitting semiconductor laser with 1.4-W average output power,” *Applied Physics Letters*, Vol. 86, No. 13, pp. 131120, 2005.

- [30]. D. Lorenser, “Picosecond VECSELs with repetition rates up to 50 GHz,” PhD thesis, Swiss Federal Institute of Technology Zurich, Switzerland, 2006.
- [31]. A. C. Tropper and S. Hoogland, “Extended cavity surface-emitting semiconductor lasers,” Progress in Quantum Electronics, Vol. 30, No. 1, pp. 1-43, 2006.

Chapter Two

Design of Optically Pumped VECSELs

2.1. Introduction

In the last chapter, the concept of an optically pumped VECSEL has been introduced. This chapter presents the operation principle of a VECSEL and the design characteristics of the device, which includes the semiconductor wafer design and laser cavity considerations.

2.2. Active Mirror Design

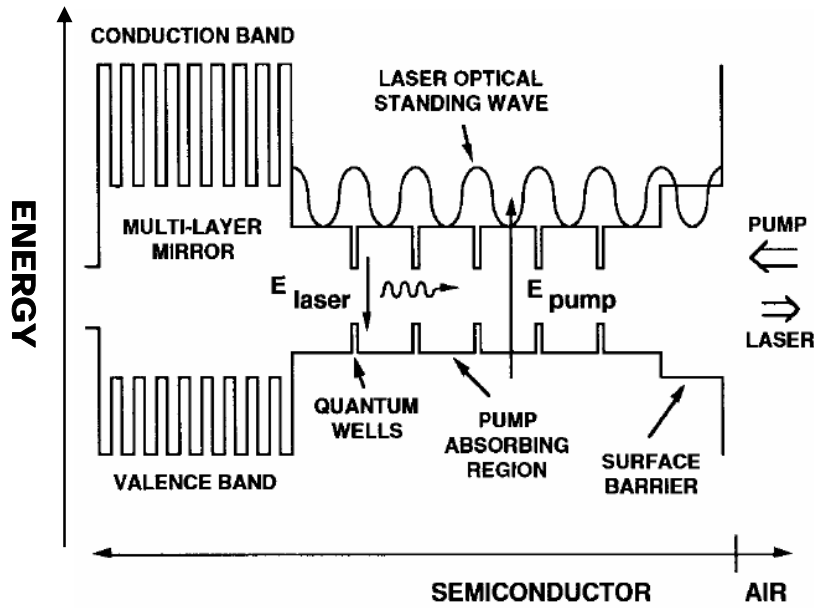


Fig. 2.1. Band-gap diagram and operating principles of the, after [1]

The basic cavity configuration of an optically pumped VECSEL has already been mentioned in the last chapter. The laser cavity is formed between the semiconductor active mirror and the external mirror. The structure of the active mirror is crucial to the overall performance of the laser device. Hence it is necessary and beneficial to understand the operating principles of the VECSEL and thereby to optimize the wafer design. Figure 2.1 shows the band-gap diagram of a VECSEL wafer and illustrates the laser operating principles. The whole wafer structure consists of two main regions: quantum well gain region and distributed Bragg reflector (DBR). Since the thickness of pump absorbing region or barriers is above 10 times of that of quantum wells, the pump radiation is mainly absorbed in barriers (pump can be solely absorbed in quantum wells (QWs) other than barriers which is named in-well pumping and will be discussed in the section 2.6). This pump absorption in the barriers will lead to the generation of free electrons and holes in conduction and valence band, respectively. Generated electrons and holes diffuse and are captured by the quantum wells with low energy band-gap. The gain for the laser radiation is

achieved through the recombination of those generated carriers. The top layer of the wafer is a window layer. It provides a surface barrier that prevents carriers from non-radiative recombination at the top surface of the wafer. The QWs are chosen to be placed at the antinodes of the laser optical standing wave which is formed in the sub-cavity between the DBR and semiconductor-air interface. The DBR, which is designed for almost 100% reflectivity of the laser light, is grown next to the gain region and serves as one of the laser cavity mirrors. This mirror can be either a semiconductor multilayer mirror grown directly on the wafer, which requires two lattice-matched materials with different refractive indices to be alternatively grown, or an externally deposited dielectric multilayer mirror.

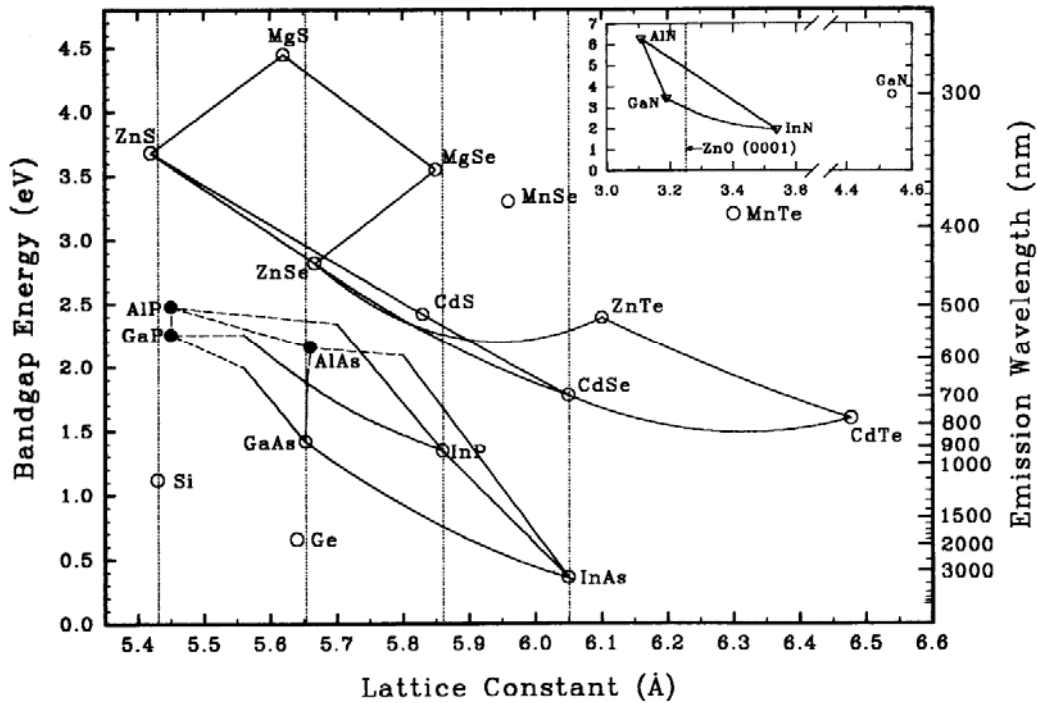


Fig. 2.2. Band-gap energy diagram and lattice constants for different compound semiconductors. The symbols indicate monatom and binary materials. “○/▽” indicate a direct bandgap and “●” indicates indirect. Lines indicate relations for common ternary and define boundaries for quaternary systems (— direct and -----indirect). Dotted lines indicate a lattice match to the common substrate materials Si, GaAs, InP and InAs). All values are for zincblende or cubic lattices except those for the nitride materials in the inset where “▽” refer to the a-axis of the wurtzite structure. after [2]

The laser emission wavelength dictates the type of material system. A large number of III-V and II-VI materials may be used in VECSEL devices. Many of these materials are limited to be only introduced into edge-emitting laser designs since their growth still requires much refinement. Fig. 2.2 is the diagram for band-gap energy and lattice constants of various semiconductor material systems of interest. It is important to note that except for narrow QWs, a close lattice match must be maintained to the substrate or a strain relieved buffer layer in order to keep high crystal quality. Ideally devices can be designed to operate at any wavelengths in the range of UV to infrared by choosing suitable material systems together with band-gap engineering of QWs. Broad spectral range and versatile characteristics of the devices can be obtained by combining more than two chemical elements to form ternary, quaternary or quinternary alloy. Current mature semiconductor material systems such as InGaAs-AlGaAs-GaAs, InGaAs-InGaAsP-GaAs, and InGaAsP-InP are available to make devices with a variety of wavelengths from visible to far infra-red of interests. The work reported in this thesis is based on InGaAs-AlGaAs-GaAs material system for emission wavelengths in near infrared region. The alloy AlGaAs is by far the most common semiconductor material simply due to the fact that AlAs and GaAs have the same lattice constant. It not only reduces the dislocations and hence allows high quality multilayer structures to be grown, but also negates the need for strain compensation and thereby simplifies the growing process.

2.2.1. Distributed Bragg Reflectors (DBRs)

DBRs consist of an alternating sequence of high and low refractive index layers with quarter-wavelength thickness, as shown in Fig. 2.3. DBR is required to have a wide high-reflectivity band or stop-band and constant phase change on reflection. This can be implemented using a few layer pairs. In order to obtain high reflectivity wide stop-band, the index contrast of the constituent materials is required to be high. An easy way to achieve this is to use all-dielectric DBRs deposited by vacuum

evaporation or sputtering. However this method adds to the complexity of the growing process as compared to the all-semiconductor mirrors, although the required number of layers is relatively high for keeping high reflectivity (>99.9%) due to the limited refractive index contrast. As Table 1.1 shows, the most frequent used all-semiconductor mirror is AlGaAs DBR. It is usually employed in VECSELs lasing in the red region from 650-660nm, in the near infrared region at around 850nm (*chapter six*) and 980nm (*chapter four and five*), by using wafer fusion AlGaAs can also be used for the devices operating at telecom wavelengths such as 1.3 and 1.5 μm , where InP substrate is used.

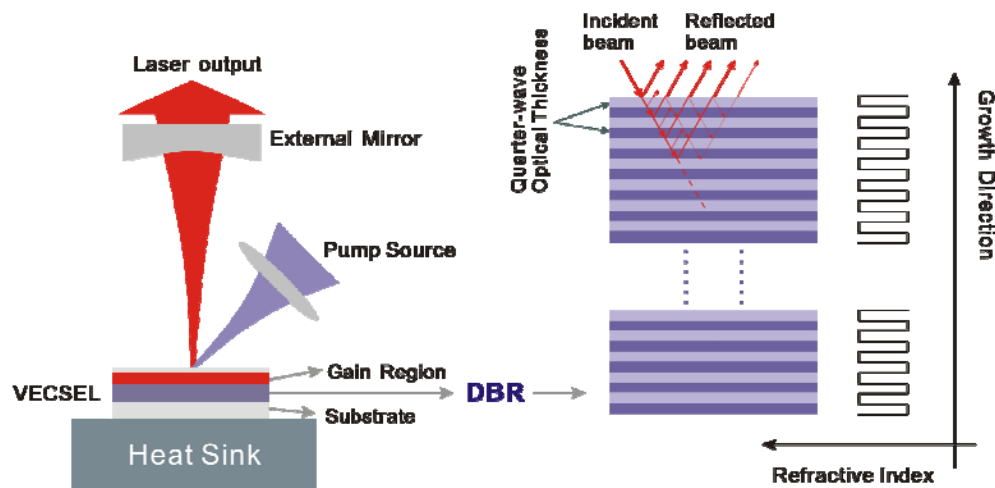


Fig. 2.3. Schematic setup of an optically pumped VECSEL and its DBR structure

2.2.1.1. Reflectivity spectrum of a DBR

The theory of an assembly of thin films is derived from Maxwell's equations of electromagnetism. In the plane wave approximation the optical properties of VECSELs mirrors have been analyzed using matrix methods and coupled-mode theory. The characteristic matrix for the i^{th} homogeneous layer of thickness d_i and refractive index n_i is given by [3]

$$M_i = \begin{bmatrix} \text{Cos}\left(\frac{2\pi}{\lambda} \cdot n_i \cdot d_i \cdot \text{Cos}(\theta_i)\right) & j \cdot \text{Sin}\left(\frac{2\pi}{\lambda} \cdot n_i \cdot d_i \cdot \text{Cos}(\theta_i)\right) / Y_i \\ j \cdot Y_i \cdot \text{Sin}\left(\frac{2\pi}{\lambda} \cdot n_i \cdot d_i \cdot \text{Cos}(\theta_i)\right) & \text{Cos}\left(\frac{2\pi}{\lambda} \cdot n_i \cdot d_i \cdot \text{Cos}(\theta_i)\right) \end{bmatrix} \quad (2.1)$$

where θ_i denotes the propagation angle in layer i , it follows the Snell's equation $n_0 \cdot \text{Sin}(\theta_0) = n_i \cdot \text{Sin}(\theta_i)$; $Y_i^{(s)}$ and $Y_i^{(p)}$ are the characteristic optical admittances for the s and p polarizations, and they can be expressed as [3]

$$Y_i^{(s)} = \sqrt{\epsilon_0 / \mu_0} \cdot n_i \cdot \text{Cos}(\theta_i) \quad (2.2)$$

$$Y_i^{(p)} = \sqrt{\epsilon_0 / \mu_0} \cdot n_i / \text{Cos}(\theta_i). \quad (2.3)$$

Hence the characteristic matrix for a series of films stacked upon each other from the bottom (N^{th} layer) to the top (1^{st} layer) is given by:

$$M = \prod_{i=1}^N M_i = \begin{bmatrix} M_{11} & M_{12} \\ M_{21} & M_{22} \end{bmatrix} \quad (2.4)$$

By multiplying the characteristic matrix of each layer, we can obtain the total characteristic matrix for the whole thin film stack, and thereby to be able calculate the reflection and transmission coefficients of the film by using following two equations:

$$r = \frac{Y_0 M_{11} + Y_0 Y_s M_{12} - M_{21} - Y_s M_{22}}{Y_0 M_{11} + Y_0 Y_s M_{12} + M_{21} + Y_s M_{22}} \quad (2.5)$$

$$t = \frac{2Y_0}{Y_0 M_{11} + Y_0 Y_s M_{12} + M_{21} + Y_s M_{22}} \quad (2.6)$$

where Y_0 and Y_s are the characteristic optical admittances for the air and the last layer (refer to eq. 2.2 and eq. 2.3 for s wave and p wave). The energy coefficients (reflectivity and transmissivity) are determined by

$$R = r \cdot r^* \quad (2.7)$$

$$T = \frac{\text{Re}[Y_s]}{\text{Re}[Y_0]} \cdot t \cdot t^* \quad (2.8)$$

Figure 2.4 displays an example of the numerically determined spectral reflectivity

$R(\lambda)$ for a DBR. A broad spectral plateau of high reflectivity, often denoted as a stop-band, appears around the Bragg wavelength or designed wavelength λ_B , the width of which can be roughly estimated from [4-5]

$$\Delta\lambda_{stop} \approx \frac{2\lambda_B \cdot \bar{\Delta n}_B}{\pi \langle \bar{n}_{group} \rangle} \quad (2.9)$$

The stop-band width is proportional to the refractive index step $\bar{\Delta n}_B = |\bar{n}_1 - \bar{n}_2|$ and the reciprocal of spatial average of the group index $\langle \bar{n}_{group} \rangle = \langle \bar{n} - \lambda \cdot d\bar{n}/d\lambda \rangle$. It has to be noted that only lossless mirrors or those with homogeneous absorption provide identical reflectivity spectra for waves incident from the top or bottom side

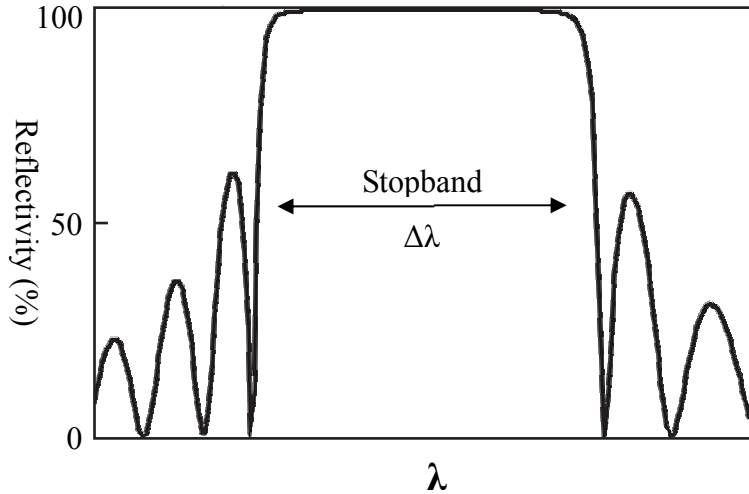


Fig. 2.4. Spectral dependence of the intensity reflection coefficient

2.2.2. Gain Region

The VECSEL gain region is designed to sit on the top of the DBR. It consists of multiple QWs spaced by barriers, as shown in Fig. 2.5.

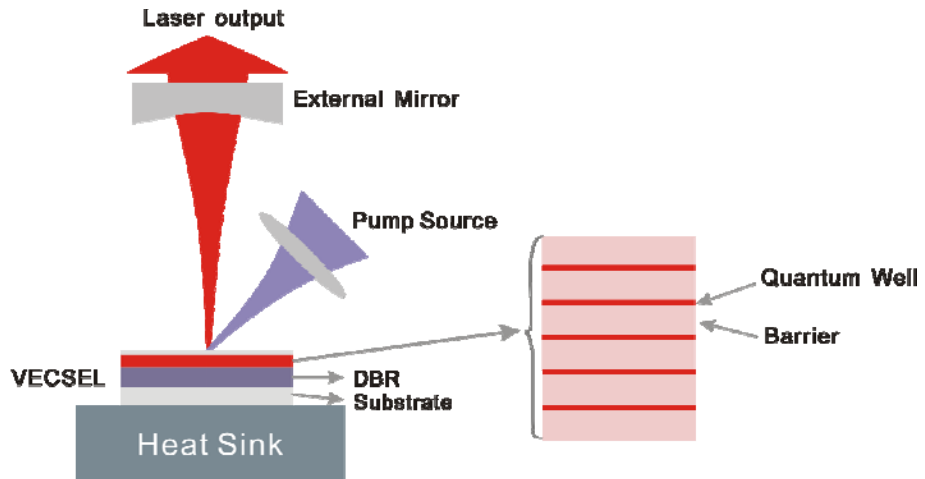


Fig. 2.5. Schematic setup of an optically pumped VECSEL and its gain structure

Two VECSELs with different gain regions are presented in this thesis. They are a strain compensated InGaAs/AlGaAs based 980nm VECSEL and an InAlGaAs/AlGaAs based VECSEL operating at 850nm. After choosing a suitable material system, the remaining issues for active region design are to determine the width and composition of the QWs to give the expected emission wavelength, and then to optimize the arrangement of the QWs.

2.2.2.1. Quantum wells

Figure 2.6 describes the energy eigenfunctions and eigenvalues of a finite one-dimensional square QW. The method for estimation of the energy levels in a square potential well is briefly presented in this section and the comprehensive description can be referred to [6].

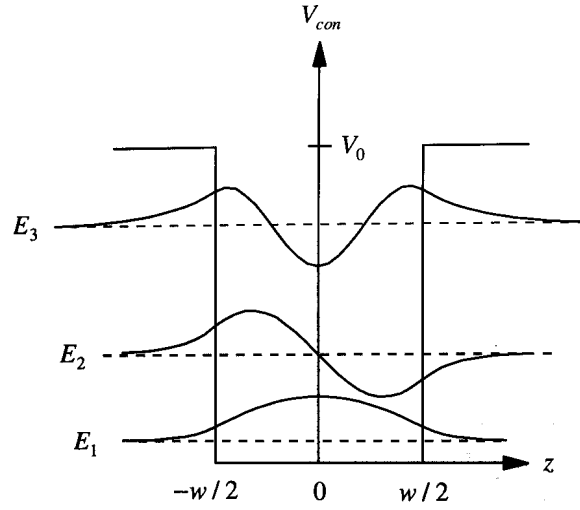


Fig. 2.6. Energy eigenfunctions and eigenvalues of a finite one-dimensional square QW. After [6]

The finite confinement potentials of a square well can be expressed as:

$$V_{con}(z) = \begin{cases} 0 & |z| < \omega/2 \\ V_c & |z| > \omega/2, \end{cases} \quad (2.10)$$

where z is the direction perpendicular to the surface of QW. In the xy plane there is no quantum confinement and the carriers can move freely. The electron eigenfunction is described as

$$\varphi_{n,k\perp}(r) = \phi_{k\perp}(r_\perp)\zeta_n(z), \quad (2.11)$$

where the z and transverse components $r_\perp(x, y)$ obey the Schrödinger equations

$$\left[-\frac{\hbar^2}{2m_z} \frac{d^2}{dz^2} + V_{con}(z) \right] \zeta_n(z) = \varepsilon_n \zeta_n(z) \quad (2.12)$$

and

$$-\frac{\hbar^2}{2m_\perp} \nabla_\perp^2 \phi_{k\perp}(r_\perp) = \varepsilon_{k\perp} \phi_{k\perp}(r_\perp), \quad (2.13)$$

where m_\perp and m_z are the effective masses for z direction and transverse direction.

Equation 2.13 describes a two dimensional free particle (i.e., no external potential and not interacting with other particles) with eigenfunctions.

$$\phi_{k\perp}(r_\perp) = \frac{1}{\sqrt{A}} e^{\pm ik \cdot r_\perp} \quad (2.14)$$

and eigenvalue

$$\epsilon_{k\perp} = \frac{\hbar^2 k_\perp^2}{2m_\perp}, \quad (2.15)$$

where A is the area of the QW. By solving Eq.2.12 and applying the boundary condition at the interfaces $\pm\omega/2$. The even states are given

$$\zeta_{2n}(z) = \begin{cases} B \cos(k_z z) & |z| \leq \omega/2 \\ Ce^{-K_z |z|} & |z| > \omega/2 \end{cases} \quad (2.16)$$

with the condition

$$\sqrt{\epsilon_z} \tan\left(\frac{\sqrt{m_z \epsilon_z}}{2\hbar^2} \omega\right) = \sqrt{V_c - \epsilon_z} \quad (2.17)$$

whose solution gives the energy of the even states.

Similarly the odd states wave functions are given by

$$\zeta_{2n-1}(z) = \begin{cases} A \sin(k_z z) & |z| \leq \omega/2 \\ -Ce^{-K_z |z|} & |z| > \omega/2 \end{cases} \quad (2.18)$$

with the condition

$$-\sqrt{\epsilon_z} \cot\left(\frac{\sqrt{m_z \epsilon_z}}{2\hbar^2} \omega\right) = \sqrt{V_c - \epsilon_z} \quad (2.19)$$

whose solution gives the energy of the odd states. Figure 2.6 illustrates the solutions for both even and odd states of a finite QW. Hence the total energy of the electron subjected to finite one-dimensional quantum confinement can be obtained by adding the motion energy in the xy plane and bound state energy in the z direction. Programs using this method can be used to calculate the conduction and valence band energies for lattice-matched GaAs/Al_xGa_{1-x}As wells.

However, devices with semiconductor heterostructures comprising two lattice matched materials could only operate in some limited spectral regions. In order to extend the spectral coverage of the laser devices, heterostructures with materials that

are not perfectly lattice matched can also be grown epitaxially. This leads to the concept of strain. Strain describes how big the mismatch between the lattice constants of two materials is. Too much strain would result in large dislocations and hence lead to many undesired defects, i.e. fractures, island formation. A critical thickness is thereby available to guarantee a stable epitaxial structure in which the materials are under elastic strain, to be obtained. If the thickness of the strained material exceeds this critical value, strain relieving misfit dislocations will propagate through the strain layer. The critical thickness for a layer to be grown on a substrate can be described as [2]

$$\varepsilon = \frac{b(1 - v \cos^2 \alpha)}{2\pi L_c (1 + v) \cos(\lambda)} \left[\ln\left(\frac{L_c}{b}\right) + 1 \right] \quad (2.20)$$

where b is the dislocation length, α is the angle between the slip plane normal vector and the Burgers vector of the dislocation, λ is the angle between the slip plane normal direction and its projection in the growth direction onto the interface plane of the epilayer and v is the Poisson ratio. Strain structure now is widely employed in QW devices, where thin QWs sandwiched by two relative thick barriers are grown on a substrate of barrier material. It let offer advantages of using a wide range of materials combinations and engineering a certain amount of the band structure and gain.

Both of the VECSELs developed in the work consist of compressive strained QWs (InGaAs/AlGaAs and InAlGaAs/AlGaAs). For the design of a strained QW, the strain induced change in energy gap, which depends on the deformation potentials, should be taken into account. Again, by programming the above model, the conduction and valence band energies for of a strained QW can be calculated.

2.2.2.2. Gain and threshold calculation

The following gain model [1] is used to calculate the optimal number of QWs in order to maximise the laser gain. The model uses a standard logarithmic gain relation given by

$$g = g_0 \ln \left(\frac{N}{N_0} \right) \quad (2.21)$$

where g_0 is the material gain parameter, N is the carrier density and N_0 is the transparency carrier density. The carrier density generated by the incident pump light can be expressed as

$$N = \frac{\eta_{abs} P_p}{h\nu N_w L_w A_p} \tau_c \quad (2.22)$$

η_{abs} is the pump absorption efficiency, $h\nu$ is the photon energy, A_p is the pump spot area, τ_c is the carrier lifetime which depends on the carrier density N , L_w is the QW thickness, and N_w is the number of QWs in the gain structure. The lasing threshold condition is

$$R_1 R_2 T_{loss} \exp(2\Gamma g_{th} N_w L_w) = 1 \quad (2.23)$$

where R and R are the cavity mirror reflectivities, T_{loss} is the round trip cavity loss, and Γ is the confinement factor which will be discussed in the following section. Hence by solving above equations Eq. 2.21-Eq. 2.23, the threshold carrier density N_{th} and threshold pump power P_{th} can be derived

$$N_{th} = N_0 \left(\frac{1}{R_1 R_2 T_{loss}} \right)^{(2\Gamma g_0 N_w L_w)^{-1}} \quad (2.24)$$

$$P_{th} = N_{th} \frac{h\nu N_w L_w A_p}{\eta_{abs} \tau_c} \quad (2.25)$$

2.2.2.3. Resonant Periodical Gain

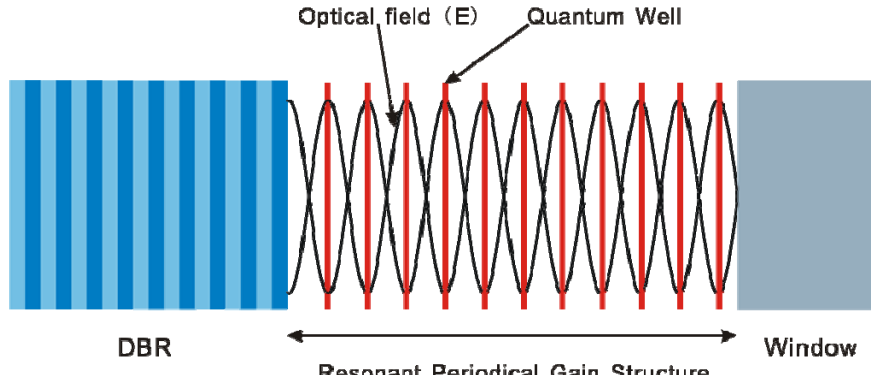


Fig. 2.7. Resonant periodical gain structure

The laser gain is provided by the multiple QW gain region where QWs are placed at the anti-nodes of the optical standing wave formed inside the semiconductor sub-cavity, as shown in Fig.2.7. This particular arrangement is called resonant periodic gain (RPG) structure [7-8]. The relation between confinement factor and the threshold gain can be described as [8]:

$$g_{th} = \frac{1}{\Gamma} \cdot \left(\alpha_i + \frac{1}{L} \cdot \ln(1/R) \right) \quad (2.26)$$

$$\Gamma = \Gamma_x \cdot \Gamma_y \cdot \Gamma_z \quad (2.27)$$

where R is the geometric mean mirror reflectivity, Γ is the confinement factor and α_i is the internal loss. Due to the large lateral dimensions ($>100\mu\text{m}$), the transverse confinement factor terms Γ_x and Γ_y are equal to unity. And Γ_z is the longitudinal confinement factor which is critical for VECSEL wafer design. It can be defined as

$$\Gamma_z = \frac{\int_{active} E^2(z) \cdot dz}{\int_L E^2(z) \cdot dz} \quad (2.28)$$

After applying the standing wave pattern of electric field $E(z) = E_0 \cdot \cos(kz)$ into Eq. 2.28 and integrate the equation, we could obtain the expression for Γ_z for the periodic gain structure

$$\Gamma_p = \frac{d}{L} \left(1 + \frac{\sin \left[\pi \left(\frac{t}{\lambda/2} \right) \right]}{\pi \left(\frac{t}{\lambda/2} \right)} \right) \equiv \frac{d}{L} \cdot \Gamma_r \quad (2.29)$$

where t is the thickness of the QW, d is the total thickness of the QWs and L is the total length for gain region; Γ_r is the relative confinement factor; λ stands for the laser wavelength. The above equation describes the longitudinal confinement factor of the RPG as a function of the length t of each active segment. The longitudinal confinement factor for the uniform gain structure (UGS) is obtained by setting $t = \lambda/2$ in the above equation. Hence relative confinement factor Γ_r equals to one for the UGS and it could approach to two for the RPG as long as the thickness of QW is thin. As Fig. 2.8 shows, the use of RPG structure can potentially double the laser longitudinal confinement factor and thereby reduce the laser threshold gain by a factor of two, when comparing with the uniform gain structure.

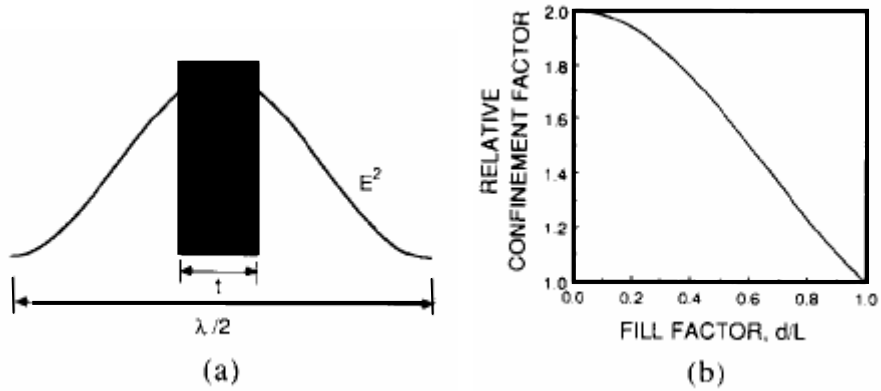


Fig. 2.8. the overlap between the optical standing wave and single QW (a) illustration of the overlap; (b) relative confinement factor as a function of fill factor defined to be d/L . [8]

In addition to the reduction of threshold or double the effective gain, RPG has another advantage over uniform gain structure. RPG can increase the mode selectivity. For the mode matching to the RPG structure $\Gamma_r \approx 2$; whereas for modes off resonances, $\Gamma=1$. By placing the active material only where it is most needed we eliminate the effects of spatial hole burning for the longitudinal mode. This property

could be helpful for the development of single longitudinal mode operation of VECSELs [9], which will be presented in chapter five.

2.2.3. Window layer

A large energy band-gap window layer is required to confine the excited carriers in the gain region in order to prevent the surface recombination. This is always achieved by using an AlGaAs layer with high Al fraction. Another function of the window layer is the control of the total thickness of the sub-cavity formed between the DBR and top surface of the wafer.

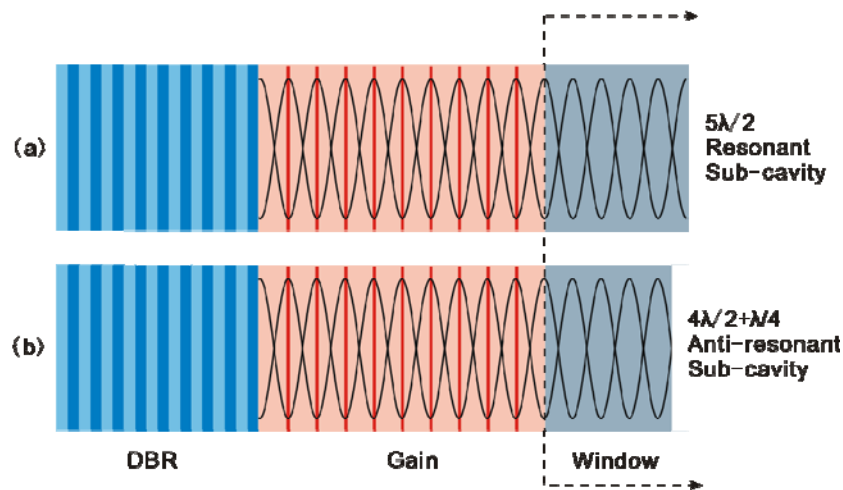


Fig. 2.9. Wafer structures with resonant sub-cavity (a) and anti-resonant sub-cavity (b)

Since the length of the RPG gain region is $m\lambda/2$, where λ is the RPG wavelength and m is a positive integer, so if the thickness of the window is controlled to be $n\lambda/2$ (n is a positive integer) then the total length of the sub-cavity is resonant to the RPG wavelength, as shown in Fig. 2.9(a). As we have discussed in last section the gain of each QW is strongly determined by the local intensity of the standing wave pattern it sees. It can be greatly enhanced by using the resonant RPG structure which leads to a much lower lasing threshold. If however, the window layer is grown to have thickness of $n'\lambda/2+\lambda/4$ (n' is a positive integer), the sub-cavity is then anti-resonant to the designed RPG wavelength, as illustrated in Fig. 2.9(b). Although the effective

gain is less than that of the resonant structure, anti-resonant RPG structure has the advantage of minimising the thermal sensitivity of the gain, and also without the spectral filtering effect caused by resonant cavity it can provide a larger bandwidth of the gain which is good for wavelength tuning and ultrashort pulse generation through mode-locking. The final capping layer (GaAsP), which is lattice matched to the window layer, is employed to avoid the oxidation of the layers with high fraction of Al and thereby reduce the potential of wafer degradation. Figure 2.10 shows the schematic of the reflectivities of both wafer structures (resonant RPG and antiresonant RPG). The laser operating wavelength matches well with one of the cavity resonances of the sub-cavity for the case of resonant RPG structure as shown in Fig. 2.10(a). While for antiresonant case in Fig. 2.10(b), laser operating wavelength is designed to stay between two resonances.

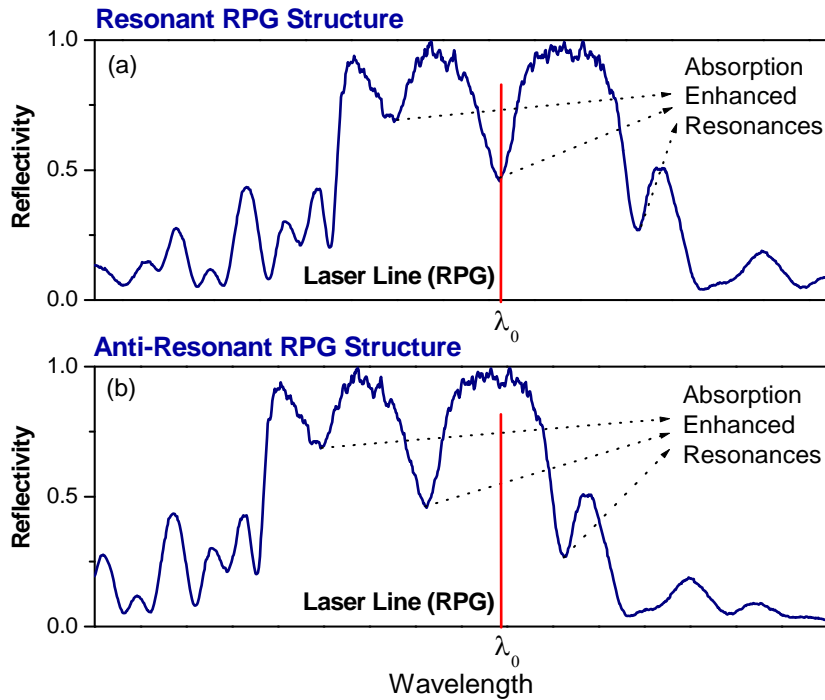


Fig. 2.10. Examples of the reflectivities for resonant (a) and antiresonant (b) RPG structures.

2.2.4. Two designed wafer structures

Based on the theoretical models described above, two wafers were designed and grown by commercial MOCVD. The details of the two wafer structures are introduced here. For an 850nm InAlGaAs/AlGaAs based VECSEL, the bandgap energy of $\text{Al}_x\text{Ga}_x\text{As}$ is given by $1.424+1.247x$ for $x < 0.45$ [10]. Hence, the aluminium fraction of the barriers should not be greater than 0.3 in order to guarantee that the bandgap of the barriers is smaller than the photon energy of the pump light, which is designed to be 670nm or photon energy of 1.85ev. And thereby $\text{Al}_{0.26}\text{Ga}_{0.74}\text{As}$ is chosen for the barriers. The $\text{In}_{0.1}\text{Al}_{0.115}\text{GaAs}$ QW with thickness of 10nm was thus determined for a laser emission wavelength of 850nm or photon energy of 1.46ev. The optimal number of QWs was found to be 17. Since the QW material is not perfectly lattice matched to the barrier material, strain compensation layers ($\text{Al}_{0.115}\text{GaIn}_{0.1}\text{AsP}_{0.18}$) are hence required to relieve the strain of the whole structure. Each QW sandwiched by two strain compensating layers is thus placed at the antinode of the optical standing wave inside the sub-cavity to form the RPG structure. The total thickness of the sub-cavity is designed to be antiresonant to the laser wavelength through controlling the length of window layer ($\text{Al}_{0.5}\text{Ga}_{0.5}\text{As}$).

Similar process was used for a wafer design based on InGaAs/AlGaAs material system operating at 980nm. The wafer was also grown by a commercial MOCVD. Barriers were chosen to be $\text{Al}_{0.04}\text{Ga}_{0.96}\text{As}$ for a pump wavelength of 808nm. $\text{In}_{0.15}\text{Ga}_{0.85}\text{As}$ QWs with thickness of 8nm were designed for a laser emission wavelength of 980nm. Strain compensation layer was determined to be $\text{GaAs}_{0.92}\text{P}$ with thickness of 2.9nm. Total sub-cavity of the wafer was antiresonant to the emission wavelength.

The two wafer structures used in this thesis, 850nm wafer and 980nm wafer, are shown in table 2.1 and table 2.2, respectively.

850 nm wafer

Layer No	Material	Mole Fraction (x)	Thickness (microns)	Purpose
14	GaAsP(x)	0.10	0.0200	Cap
13	Al(x)GaAs	0.5	0.309	Window
12	Al(x)GaAs	0.26	0.1123	Barrier
11	Al(0.115)GaIn(0.1)AsP(0.18)		0.0050	Strain comp. layer
10(x16)	In(0.1)Al(0.115)GaAs		0.0100	QW
9(x16)	Al(0.115)GaIn(0.1)AsP(0.18)		0.0050	Strain comp. layer
8(x16)	Al(x)GaAs	0.26	0.1017	Barrier
7(x16)	Al(0.115)GaIn(0.1)AsP(0.18)		0.0050	Strain comp. layer
6	In(0.1)Al(0.115)GaAs		0.0100	QW
5	Al(0.115)GaIn(0.1)AsP(0.18)		0.0050	Strain comp. layer
4	Al(x)GaAs	0.26	0.1123	Barrier
3	Al(x)GaAs	1	0.0698	DBR
2	Al(x)GaAs	0.18	0.0599	DBR
1	GaAs	0	0.5	Buffer

Table 2.1, Designed 850nm wafer structure

980 nm wafer

Layer No	Material	Mole Fraction (x)	Thickness (microns)	Purpose
10	GaIn(x)P	0.48	0.05	Cap
9	GaAs		0.0030	Window
8	Al(x)GaAs	0.3	0.3857	Window
7	Al(x)GaAs	0.06	0.2850	Barrier
6(x14)	Ga In(x)As	0.15	0.0080	QW
5(x14)	GaAs(x)P	0.92	0.00291	Strain comp. layer
4(x14)	Al(x)GaAs	0.06	0.1030	Barrier
3(x30)	AlAs		0.0826	DBR
2	GaAs		0.0695	DBR
1	GaAs		0.5000	Substrate

Table 2.2, Designed 980nm wafer structure

2.3. Laser Cavity Design

The external VECSEL cavity can be designed by using the ABCD law [11], which describes the transformation of a Gaussian beam propagating inside the resonator. The complex parameter of a Gaussian beam is expressed as

$$\frac{1}{q} = \frac{1}{R} - i \frac{\lambda}{\pi \omega^2 n} \quad (2.30)$$

where R is the radius of curvature of the wavefront and ω is the Gaussian beam radius. In order to oscillate stably in a resonator, the cavity eigenmodes need to follow the self-consistency condition, which requires that the oscillating mode should reproduce itself after each cavity round trip. This can be described as

$$q_s = \frac{Aq_s + B}{Cq_s + D} \quad (2.31)$$

where q_s is the beam parameter at an arbitrary reference plane and A, B, C, D are the elements of the transformation matrix of the resonator. By solving $1/q_s$ and applying the condition $AD-BC=1$, we obtain the stability condition for a confined beam

$$\left| \frac{D+A}{2} \right| < 1 \quad (2.32)$$

and the complex beam parameter for a steady state eigenmode is given by

$$\frac{1}{q_s} = \frac{D-A}{2B} - i \frac{\sqrt{1 - [(D+A)/2]^2}}{B} \quad (2.33)$$

By comparing eq.2.30 with eq. 2.33, the radius of curvature R and the beam radius at that reference plane can thereby be determined as

$$R_s = \frac{2B}{D-A} \quad (2.34)$$

$$\omega_s = \left(\frac{\lambda}{\pi n} \right)^{1/2} \frac{B^{1/2}}{\left[1 - [(D+A)/2]^2 \right]^{1/4}} \quad (2.35)$$

Following above method, beam parameters at other planes can be obtained and thus the beam radius ω and the radius of curvature R at any planes in the laser resonator

are known. Three cavity configurations are employed in the thesis. In Chapter Four, a three-mirror cavity design was employed for the investigations on a synchronously pumped VECSEL. The single frequency VECSEL to be presented in Chapter Five is based on a compact four-mirror cavity configuration. In Chapter Six, a simple two-mirror cavity is used in an optically in-well pumped VECSEL.

2.3.1. Two-mirror cavity

Since only one external mirror is required, two-mirror cavity is considered to be the simplest cavity configuration for VECSELs, as shown in Fig. 2.11.

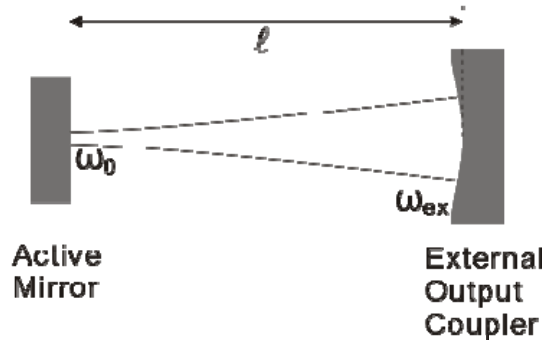


Fig. 2.11, Two-mirror cavity configuration

The VECSEL resonator forms between an active mirror and an external curved output coupler. The beam radius on the active mirror and external output coupler can be determined respectively by using the above method to be [11]

$$\omega_0 = \left(\frac{\lambda}{\pi n} \right)^{1/2} \left(\frac{l}{2} \right)^{1/4} \left(R - \frac{l}{2} \right)^{1/4} \quad (2.36)$$

$$\omega_{ex} = \left(\frac{\lambda l}{2\pi n} \right)^{1/2} \left[\frac{2R^2}{l(R-l/2)} \right]^{1/4} \quad (2.37)$$

where l is the for external cavity length, λ is the laser wavelength, n is the refractive index of the air and R is the radius of curvature of the wavefront.

Although this cavity configuration could enable the introduction of optical elements into the cavity, it is not used widely for many applications, i.e. single frequency and mode locking. This is because of two main reasons. First, the walk-off loss [12]

caused by the etalon can be expressed as $l = [R(1 - R^2)^2] \cdot (2t\theta / n\omega_0)^2$, where R is the reflectivity of the etalon, t is the etalon thickness, θ is the tilting angle of the etalon and ω_0 is the spot size of the Gaussian mode on the etalon. Therefore in two mirror cavity the significant change of the laser spot size on the etalon along the cavity axis would result very much walk-off loss in the inserted etalons which are required for single frequency operation. Secondly, two-mirror cavity has extremely tight tolerance on the cavity length detuning. Even slightly change on the cavity length could make the laser unstable. Hence it is not suitable for the active mode locking where proper detuning is essential to match the external modulation frequency. Three-mirror cavity configuration is therefore employed to improve the laser performance.

2.3.2. Three-mirror cavity

Figure 2.12 shows the schematic of a three-mirror resonator. It consists of an active mirror, a curved mirror with focal length of f and a plane output coupling mirror.

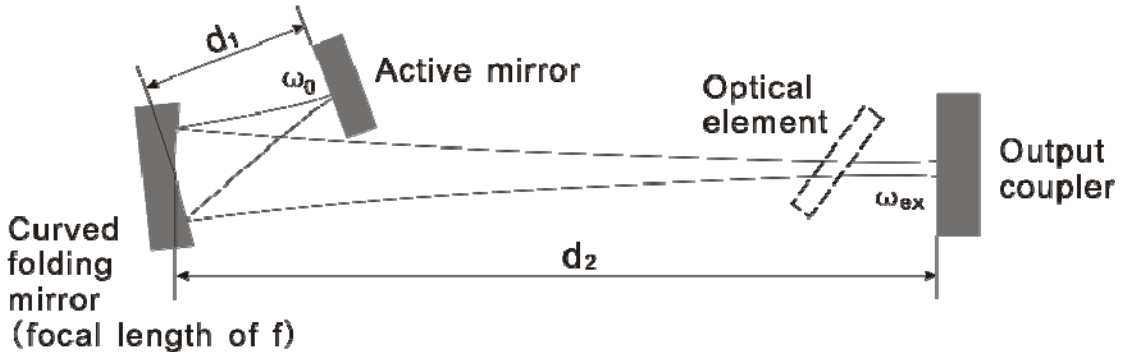


Fig. 2.12. Three-mirror configuration

The beam radius on the active mirror and the output coupler can be expressed as [13]

$$\omega_0^4 = \left(\frac{\lambda}{\pi}\right)^2 \left[f^2 \left[(d_1 - f) / (d_2 - f) \right] - (d_1 - f)^2 \right] \quad (2.38)$$

$$\omega_{ex}^4 = \omega_0^2 \left[\frac{(d_2 - f)}{(d_1 - f)} \right] \quad (2.39)$$

where ω_0 and ω_{ex} are the beam radius at active mirror and output coupler respectively, d_1 and d_2 are the length of the two arms of the cavity, f is the focal length of the

curved mirror corresponding to half of the radius of curvature R. In this configuration the curved mirror working as an intra-cavity lens can focus the laser radiation to a very small spot on the gain region and hence reduce the threshold. Different spot sizes are easily obtainable by varying the length of the first arm d_1 . Further more since the d_1 is always set to close to the focal length of the curved mirror, laser beam is hence almost collimated in the second cavity arm, where different optical elements can be inserted. Three-mirror thus has a larger stability range when compared to two-mirror cavity. The stability condition can be described as [13]

$$f < d_1 < \frac{f^2}{d_2 - f} + f . \quad (2.40)$$

This provides a significant cavity length adjustment which is desired for the active mode locking operation.

2.3.3. Four-mirror cavity

Four-mirror cavity or focusing cavity is a more complicated cavity configuration. As shown in Fig. 13a, the Z-shaped cavity consists of four mirrors including two plane mirrors and two concave mirrors. Thus a tight focus can be obtained between the two concave mirrors. This cavity configuration with a tight focus in the center is essential for many applications such as Kerr lens mode locking, intra-cavity nonlinear frequency conversion where nonlinear crystal can be placed at the focus. Comparing with the three-mirror cavity, four-mirror cavity is more suitable for a compact cavity design.

In order to simplify the calculation, the four-mirror cavity can be considered to be equivalent to a two-mirror cavity. This is due to the fact that each symmetric optical system is equivalent to a lens positioned at a distance d from the old reference plane [xxx]. Therefore, the resonator arms (end mirror L1, R1; end mirror L2, R2) shown in Fig. 2.13b are equivalent to two concave mirrors (R'_1 and R'_2) with distance of d_1

and d_2 to the reference planes shown in Fig. 2.13c. Two cavity parameters R'_1, d_1, R'_2, d_2 can be described by using original cavity parameters (R_1, R_2, L_1, L_2, L) as

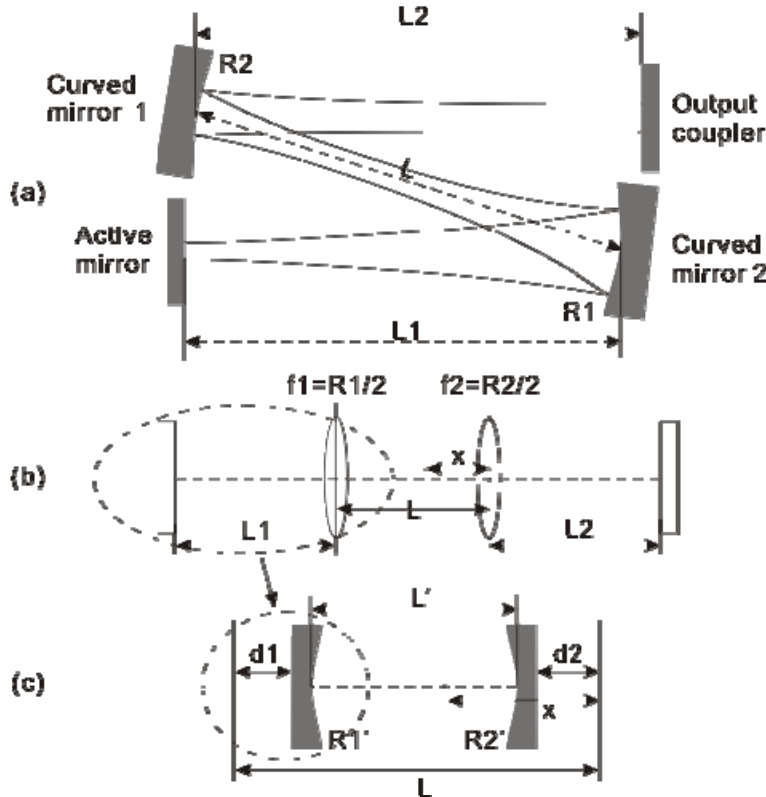


Fig. 2.13. Four mirror cavity configuration

$$d_1 = -\frac{R_1}{2} \frac{1}{1 - R_1/(2L_1)} \quad (2.41)$$

$$R'_1 = -\left(\frac{R_1}{2}\right)^2 \frac{1}{L_1 \left[1 - R_1/(2L_1)\right]} \quad (2.42)$$

$$d_2 = -\frac{R_2}{2} \frac{1}{1 - R_2/(2L_2)} \quad (2.43)$$

$$R'_2 = -\left(\frac{R_2}{2}\right)^2 \frac{1}{L_2 \left[1 - R_2/(2L_2)\right]} \quad (2.44)$$

The relation between the folding cavity length L and the equivalent two-mirror cavity length L' can be expressed by

$$L = \frac{R_1 + R_2}{2} - (R'_1 + R'_2) + L' \quad (2.45)$$

Hence, by using ABCD matrices described in the beginning of section 2.3, the beam waist of the two-mirror cavity is thus determined as

$$\omega_0^4 = \left(\frac{\lambda}{\pi}\right)^2 \frac{L(R'_1 - L)(R'_2 - L)(R'_1 + R'_2 - L)}{(R'_1 + R'_2 - 2L)^2} \quad (2.46)$$

This configuration is used for the development of a compact single frequency VECSEL which will be discussed in Chapter Five.

2.4. Thermal management

Thermal management of optically pump VECSELs have been extensively studied since the first VECSEL was reported. In a standard VECSEL gain region, thin QWs are surrounded by thick barriers, pump photons are absorbed in those barriers whose bandgap energy is designed to be much higher than that of the QWs. The generated free carriers then drop into and are confined in the QWs. This so called barrier pumping would lead to a large quantum defect - the difference in energy between pump and laser, and the extra energy then becomes the main source for the heat deposited in the gain region. As the temperature rises in the gain region, the effective gain reduces and the output power rolls over [1, 14]. This thermal rollover effect can be attributed to two main effects [1]: firstly, the peak gain from the individual QWs decreases as the temperature rises; secondly, the reduced bandgap energy of the QWs induced from the temperature rise causes the red-shifting of the photoluminescence wavelength and the QW gain peak. The RPG wavelength and the subcavity resonance also shift to longer wavelength due to the fact that the refractive index of semiconductors increases with temperature. Those two wavelengths (gain peak and RPG wavelength) shift at different rates, which are $0.3\text{nm}/^\circ\text{C}$ and $0.1\text{nm}/^\circ\text{C}$ respectively. The difference in the shifting rate would result in the spectral misalignment of the gain peak and RPG wavelength, and thereby the thermal rollover of laser output. A widely used method to delay thermal rollover induced from the misalignment of two wavelengths and thereby to improve the output power is to design a structure

with offset gain, which means that the RPG wavelength and the peak wavelength of the gain are designed to coincide at the operating temperature. However, this design can only be satisfied at one specific temperature and the laser temperature increases with the pump power, so an efficient technique to extract waste heat from the gain region of the device is still crucial for the high power operation of the VECSELs. It can be achieved by liquid capillary bonding [15] with a high thermal conductivity crystal on the top of emitting surface or by thinning or complete removing the substrate from the structure. The investigations and comparisons on these two methods have shown that the heatspreader approach is potentially more robust for removing waste heat from VECSELs [16]. By using heatspreaders, the thickness of the substrate and the DBR conductivity are not considered to be critical factors and hence there is no limitation on the materials, which means heatspreaders can be potentially used to enable the high operation of VECSELs at any wavelengths. In addition, no post-growth etching and processing makes heatspreader a much simpler way for implementation. Due to the highest thermal conductivity of any solid [17], single crystal diamonds therefore are the best choices to be served as heatspreaders.

2.5. Liquid capillary bonding

In the work of this thesis, heat dissipation of the VECSELs is achieved by using diamond heat spreaders via liquid capillary bonding. The analytical model for this technique was proposed by Z. L. Liau in 2000 [15]. The whole experimental process for the bonding is illustrated in Fig. 2.14. A 3mm x 3mm sample was cleaved off from a VECSEL wafer. Both sample and diamond are needed to be thoroughly cleaned by using methanol. The diamond is placed onto the top surface or emitting surface of the sample. One drop of methanol or deionised water is placed to one side of the edges of the sample and diamond. The liquid will flow to the sample and fill the airgap between the two surfaces of the diamond and sample. At this time, interference fringes of the liquid thin film can be watched from the top surface of the

diamond. Finally pressure is required to keep two elements bonding tightly till the liquid is completely evaporated from the gap. This can be known simply by monitoring the interference fringes. The fringes gradually pushed out and eventually the entire sample become fringeless except for some damaged spots. Sometimes sample or diamond's surface is not very flat. This means the sample can only be partially bonded (fringes can still be observed in some parts). Partially bonding can be compensated by adjusting the VECSEL holder so as to apply proper mechanical pressure to the sample.

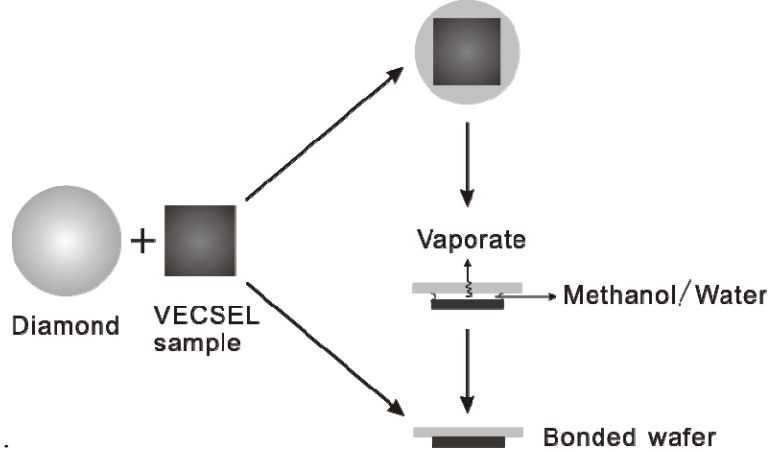
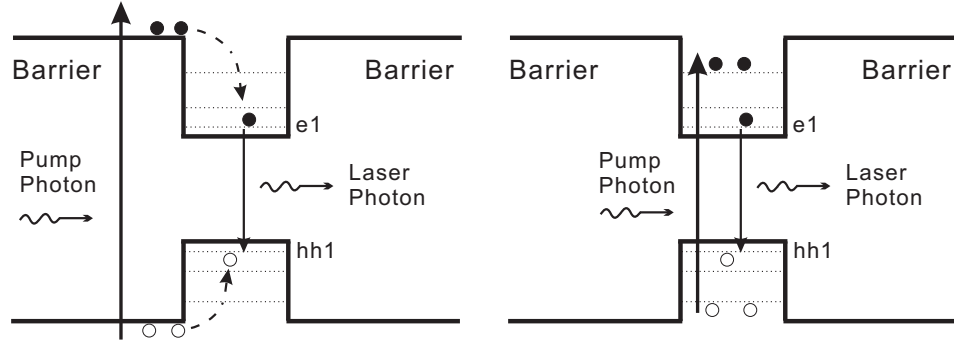


Fig. 2.14. Schematic of liquid capillary bonding of a semiconductor wafer sample with a diamond

2.6. Optical in-well pumping

The discussion above has shown that a good thermal management is essential to the high power operation of the VECSELs. Besides the capillary bonding and substrate removing, an alternative way is to pump the QWs directly. As Fig. 2.15 shows, conventional barrier-pumping design of VECSELs requires a large difference in energy between a pump and a laser photon and thereby a large quantum defect (typically 20%), which seems to be the biggest influence on the heat generated in the device. Hence in order to address the thermal problem in the first place, minimising the energy difference between pump and laser would be highly desirable and the idea of In-well pumping was born [18].



(a) Barrier pumping

(b) In-well pumping

Fig. 2.15. Operating principle of barrier pumping and in-well pumping

In this pumping concept, the pump photon energy is chosen to be smaller than the band-gap energy of the barriers but larger than that of the QWs. Hence the entire pump light is absorbed in the QWs directly and much less heat in the gain region would be expected. In addition to the heat suppression, In-well pumping also offers an advantage of enabling the operation of shorter wavelength VECSELs possible than the conventional barrier pumping VECSELs. However the accompanied problem for in-well pumping is the low pump absorption due to the smaller volume of the QW regions. The possible ways to handle the problem are: First, to increase passes of the pump beam through the gain region by designing a suitable pump recycling optics as used in solid state lasers [19]; Second, to design a special wafer structure to enhance the absorption, such as to make the sub-cavity of the wafer to be resonant to both of laser and pump frequency and to widen the thickness of the QWs. The details on operation of In-well pumping of an 850nm VECSEL will be discussed in Chapter Six, and the way to optimise the laser system is also investigated there.

2.7. References

- [1]. M. Kuznetsov, F. Hakimi, R. Sprague, and A. Mooradian, “High-power ($>0.5\text{-W}$ CW) diode-pumped vertical-external-cavity surface-emitting semiconductor lasers with circular TEM₀₀ beams,” IEEE Photonics Technology Letters, Vol. 9, No. 8, pp. 1063-1065, 1997.
- [2]. T. E. Sale, Vertical Cavity Surface Emitting Lasers, Research Studies Press LTD, 1995.
- [3]. H. Li, K. Iga, Vertical-Cavity Surface-Emitting Laser Devices, Springer-Verlag Berlin, 2002.
- [4]. P. Yeh, Optical Waves in Layered Media, J. Wiley & Sons New York, 1988.
- [5]. K. J. Ebeling, Integrated Optoelectronics, Springer-Verlag Berlin, 1993.
- [6]. W. W. Chow and S. W. Koch, Semiconductor-Laser Fundamentals Physics of the Gain Materials, Springer-Verlag Berlin 1999.
- [7]. M. Y. A. Raja, S. R. J. Brueck, M. Osinsky, C. F. Schaus, J. G. McInerney,, T. M. Brennan, and B. E. Hammons, “Resonant periodic gain surface-emitting semiconductor lasers,” IEEE Journal of Quantum Electronics, Vol. 25, No. 6, pp. 1500-1512, 1989.
- [8]. S. W. Corzing, R. S. Geels, J. W. Scott, R. H. Yan, and L. A. Coldren, “Design of Fabry-Perot surface-emitting lasers with a periodic gain structure,” IEEE Journal of Quantum Electronics, Vol. 25, No. 6, pp. 1513-1524, 1989.
- [9]. R. H. Abram, K. S. Gardner, E. Riis, and A. I. Ferguson, “Narrow linewidth operation of a tunable optically pumped semiconductor laser,” Optics Express, Vol. 12, No. 22, pp. 5434-5439, 2004.
- [10]. S. Adachi, “GaAs, AlAs, and Al_xGa_{1-x}As: Material parameters for use in research and device applications,” Journal of Applied Physics, Vol. 58, No. 3, pp. R1-R29, 1985.
- [11]. A. Yariv, Optical Electronics 3^{ed}, CBS College Publishing, 1985.
- [12]. W. R. Leeb, “Losses introduced by tilting intracavity etalons,” Applied Physics, Vol. 6, No. 2, pp. 267-272, 1975.
- [13]. H. Kogelnik and T. Li, “Laser beams and resonators,” Vol. 5, No. 10, Applied Optics, pp. 1550-1567, 1966.

- [14]. D. B. Young, J. W. Scott, F. H. Peters, M. G. Peters, M. L. Majewski, B. J. Thibeault, S. W. Corzine, and L. A. Coldren, “Enhanced performance of offset-gain high barrier vertical-cavity surface-emitting lasers,” IEEE Journal of Quantum Electronics, Vol. 29, pp. 2013-2021, 1993.
- [15]. Z. L. Liau, “Semiconductor wafer bonding via liquid capillarity,” Applied Physics Letters, Vol. 77, No. 5, pp. 651-653, 2000.
- [16]. A. J. Kemp, G. J. Valentine, J. M. Hopkins, J. E. Hastie, S. A. Smith, S. Calvez, M. D. Dawson, and D. Burns, “Thermal Management in Vertical-External-Cavity Surface-Emitting Lasers: Finite-Element Analysis of a Heatspreadter Approach,” IEEE Journal of Quantum Electronics, Vol. 41, No. 2, pp. 148-155, 2005.
- [17]. L. H. Wei, K. P. Kuo, R. L. Thomas, T. R. Anthony, and W. F. Banholzer, “Thermal-conductivity of isotopically modified single-crystal diamond,” Physical Review Letters, Vol. 70, No. 24, pp. 3764-3767, 1993.
- [18]. A. Giesen, S. -Sbeyertt, and U. Brauch, “Laser amplifier system,” EU Patent Application WO 03/100 922 A2, May 20, 2003.
- [19]. A. Giesen, H. Hugel, A. Voss, K. Wittig, U. Brauch, and H. Opower, “Scalable concept for diode-pumped high-power solid-state lasers,” Applied Physics B, Vol. 58, No. 5, pp.365-372, 1994.

Chapter Three

Laser mode locking and dispersion management

3.1. Introduction

Mode locking is an efficient way for the generation of ultrashort pulses from laser sources. In this chapter the basic principle of the laser mode locking is introduced. Different techniques including active mode locking and passive mode locking are described. Since dispersion has an important impact on the propagation of the laser pulses, a well management of the pulse dispersion can thus lead to a better control of the pulse duration. Five widely used techniques for dispersion management are introduced here.

3.2. Laser mode locking

Without frequency selective elements inside the cavity, a free-running laser normally oscillates on many cavity modes within the gain profile of the active medium, as shown in Fig. 3.1. Since there is no definite phase relations between those equally spaced cavity modes (frequency spacing $\Delta\nu$ equals to laser repetition frequency $c/2L$, where c is the optical velocity and L is the cavity length), the laser radiation in the time domain equals to the sum of the intensities of all laser oscillating modes and hence is an incoherent light with infinite series of identical bursts spaced with $\Delta t = 2\pi/\Delta\nu$. However, if a modulation with a frequency of $c/2L$ is applied to the laser so as to couple all laser modes and force them to oscillate in phase, then in the time domain all laser waves at different frequencies will interfere constructively

resulting in an intense and short burst of light. This process is named “mode locking or phase locking”. As Fig. 3.1 shown, the time spacing between two laser pulses equals to the laser cavity round trip time and the width of the pulse is inverse proportional to the bandwidth of the laser gain spectrum. Therefore, the laser pulse duration is inherently determined by the number of oscillating modes of the laser gain bandwidth. The broader the gain bandwidth is the shorter the laser pulse will be.

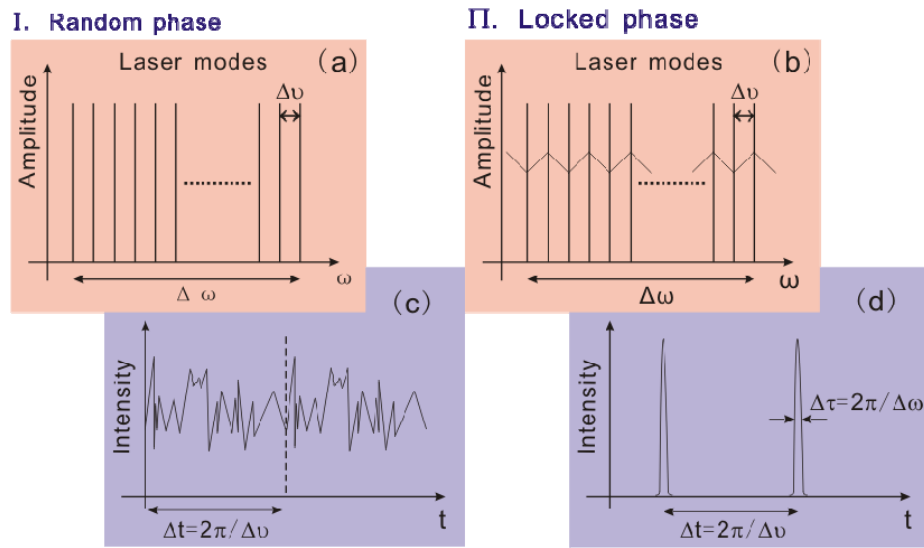


Fig. 3.1. Comparisons of the laser output for the modes with random phase in frequency domain (a) and in time domain (c), and the modes with the same phase in frequency domain (b) and in time domain (d).

This kind of modulation required for mode locking could be applied externally as in the case of active mode locking to the laser cavity loss or gain at either the fundamental or a higher harmonic of the cavity longitudinal mode frequency. Or the modulation can be applied passively to the laser radiation itself by using an intensity dependent saturable absorber as in the case of passive mode locking.

3.2.1. Active mode locking

To attain active mode locking, an external modulation is applied to periodically modulate either cavity losses or the roundtrip phase change. The modulation can be

provided by the output of other mode-locked lasers through gain modulation which is termed synchronous mode locking. It can also be achieved directly by placing an intra-cavity acousto-optic (amplitude modulation AM mode locking) or electro-optic devices (frequency modulation FM mode locking) at one end of the cavity, as shown in Fig. 3.2.

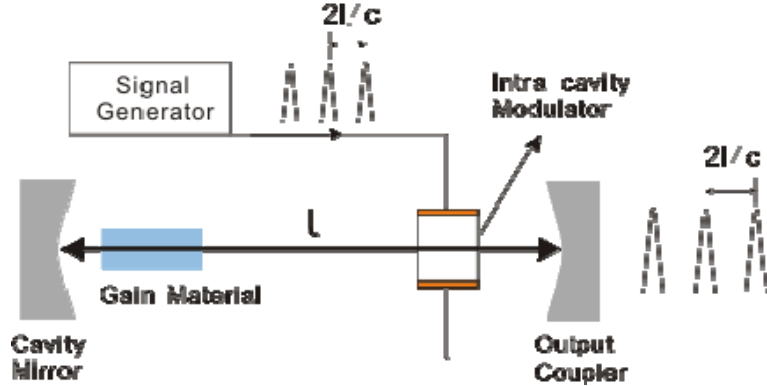


Fig. 3.2. Schematic setup for active mode locking of a laser

When the modulation frequency is synchronized with the cavity repetition rate ($c/2l$) of the laser cavity, the intra-cavity modulator acts like a fast shutter, which blocks the light all the times except when the pulse are about to cross it and opens for the duration of the pulse (usually in picoseconds), as shown in Fig. 3.2. The cavity roundtrip time is of the order of nanoseconds for most solid state bulk lasers. This corresponds to externally modulation frequencies of hundreds of MHz. Although repetition rate as high as a few of GHz has been obtained in active mode-locked lasers, active mode locking is not suitable for generating pulses with high repetition rate (10's GHz) simply due to the limited speed of driving electronics of the devices. Hargrove et al. achieved the first active mode locking on He-Ne lasers through internal loss modulation inside the resonator [1]. The analytic theory of active mode locking was firmly established and can be refer to [2-3].

The pulse-shortening rate (PSR) is always used for evaluating the effects of a modulator on the pulse shortening ($\Delta\tau/\tau$) per pass. It is expressed as [5]

$$\frac{\Delta\tau}{\tau} = \frac{m \cdot \omega_m^2 \cdot \tau^2}{4} \quad (3.1)$$

where $\Delta\tau$ is defined as a decrease in pulse width, m and ω_m are the modulation amplitude and frequency, respectively. As the pulse gets shorter, the effectiveness of the modulator in terms of PSR reduces significantly. This is a key difference between active mode locking and passive mode locking.

The steady state pulse width can be described as [5]

$$\tau = \sqrt{\frac{1}{\omega_g \cdot \omega_m}} \left(\frac{8g}{m} \right)^{\frac{1}{4}} \quad (3.2)$$

Thus, the pulse-width varies inversely with the square root of the gain bandwidth ω_g and the modulation frequency ω_m . Therefore, due to the limitation of the modulation frequency and the laser gain bandwidth, pulse width of an active mode-locked laser is always in the ps regime.

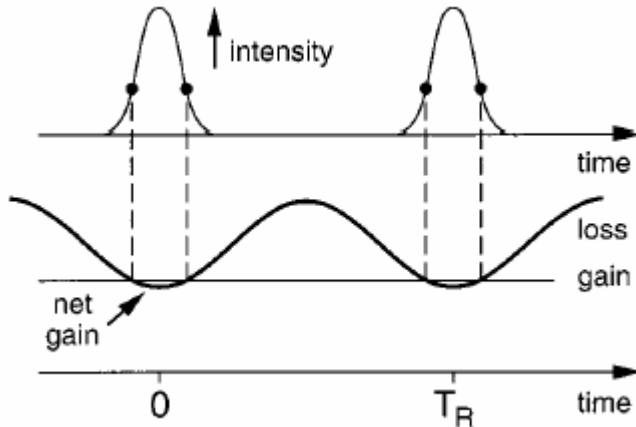


Fig. 3.3. Pulse formation from an actively mode locked laser in the time domain and the time dependence of net gain. After [4]

Synchronous mode locking

Synchronous mode locking is a technique to generate short pulses by exciting the gain medium at a repetition rate synchronized with the cavity mode spacing. As shown in Fig. 3.4, this can be done by using either one of two methods. First one is

for electrical pumping. In electrically pumped semiconductor lasers, laser gain is periodically modulated by applying the modulated input current. This modulated signal can be achieved by employing a frequency synthesiser and a radio frequency (RF) amplifier. Since the modulation frequency is limited by the speed of electronic devices to hundreds of MHz or a few of GHz, this technique is thus only suitable for semiconductor lasers with external cavity, such as VECSEL, which have relative low cavity frequency.

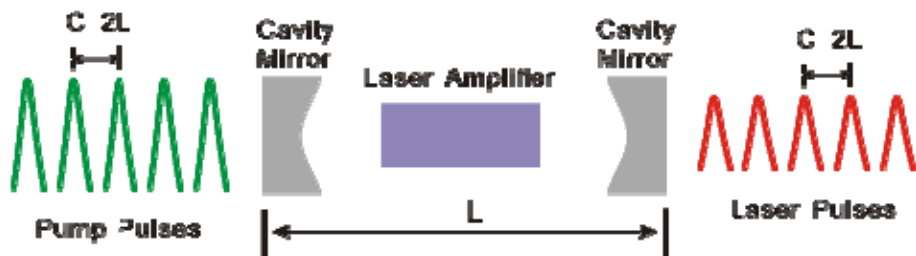


Fig.3.4. Schematic setup of a synchronously mode locked laser

The other method is for optical pumping. Mode locking can be promoted by using another pulsed laser (mode locked laser or gain switched semiconductor laser) that emits pulses at the round trip rate of the cavity to be pumped. The laser gain exceeds the cavity loss and hence generates laser pulses only when the pump pulses reach and pass through the gain medium. Therefore it is essential to precisely control the laser cavity so as to guarantee both laser cavity and pump cavity have the same length or the cavity repetition frequency. The main advantage of synchronous mode locking over other active mode-locking techniques is that when the carrier upper-state lifetime is not longer than the inverse pulse repetition rate, i.e. ns upper-state life time for semiconductor laser media, the laser gain is not wasted between two consecutive pulses. Hence synchronous mode-locking can be applied to a broader range of gain media which have too short a lifetime to be practical in CW operation. For instance, laser dyes such as styryl 8, 9, and 14 are quite efficient when pumped with short pulses [6]. However this is not the case for most doped insulator crystal

based gain media with carrier upper-state life time of microseconds which greatly exceeds the laser cavity round trip time.

The study of cavity length detuning effects is of great interest for a better understanding and a better controlling of pulsed laser systems. Related studies have been performed for conventional synchronously pumped systems [7-9]. The output laser pulsewidth and pulse intensity is already found to be critically dependent upon the laser cavity length [10-12].

3.2.2. Passive mode locking

Compared with active mode locking, no external modulation is needed for passive mode locking. However the mode locking is achieved by incorporating a saturable absorber into the laser cavity. Since the saturable absorber can modulate the cavity loss much faster (the shorter the intra-cavity pulse the faster the cavity loss modulation will be) than electronic modulators, passively mode locked lasers can generate much shorter pulses than the pulses from actively mode locked lasers.

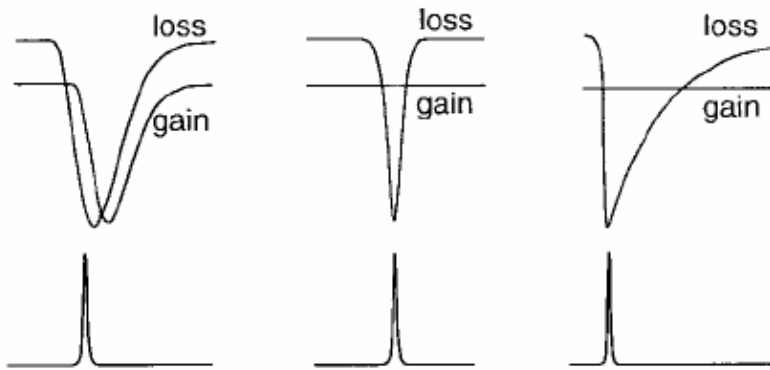


Fig.3.5. Pulse-shaping gain and loss dynamics for (a) passive mode locking with a slow saturable absorber and dynamic gain saturation; (b) passive mode locking with a fast saturable absorber; (c) passive mode locking with a slow saturable absorber plus solution formation. After [13]

The physical mechanisms for passive mode locking can be described by using three fundamental models [13]: slow saturable absorber mode locking with dynamic gain

saturation [Fig. 3.5 (a)] [14], fast saturable absorber mode locking [Fig. 3.5 (b)] [15-16], and soliton mode locking [Fig. 3.5 (c)] [17-19].

- ❖ Passive mode-locking with a slow saturable absorber is able to generate pulses which are shorter than the absorption recovery time of the saturable absorber [20]. The pulse shaping is achieved by the combined action of both the saturable absorber arid a saturable amplifier. All laser gain media exhibit some degree of saturation in operation which leads to gain competition, and also to both pulse compression and line-width-narrowing after many cavity transits.
- ❖ The physical mechanism of the fast saturable absorber [21] is based on optical Kerr effect [22]. This effect may lead to a non-linear intensity-dependent refractive index, described by $n = n_0 + n_2 \cdot I$, in the optical components of the laser cavity, and thereby promote self-mode-locking through the effects of self phase modulation (SPM) or self-focusing. Both phenomena (SPM and self-focusing) are a consequence of different parts of an optical signal experiencing different refractive indices and therefore different non-linear phase shifts, resulting in an instantaneous intensity-dependent loss for the intracavity laser radiation. Two practical techniques, additive pulse mode-locking (APM) [23] and Kerr lens mode locking (KLM) [24-26], are based on the effect of SPM and of self focusing respectively.
- ❖ The pulse formation in soliton mode locking [17-19] is dominated by the balance of group velocity dispersion (GVD) and SPM. The net gain can remain open for more than ten times longer than the ultrashort pulse, depending on the specific laser parameters [18]. An additional loss mechanism, such as a saturable absorber [17, 19] or an acousto-optic modulator [27-28], is desired to start the pulse formation process and stabilize the soliton.

3.3. Dispersion Compensation

Ultra-short pulses (sub-picosecond) generated from mode-locked lasers described in the above sections can be broadened by the undesired dispersion introduced from the laser gain element and other optical components. While the naturally occurring dispersion is usually positive (i.e., normal dispersion), the desired dispersion may either be close to zero or even anomalous (for the formation of quasi-soliton pulses in the cavity). Such dispersion values can be achieved by introducing optical components with anomalous dispersion. Such components are usually either special dispersive dielectric mirrors (e.g. in the form of monolithic Gires-Tournois interferometers (GTIs) or chirped mirrors), or prism pairs. Dispersion compensation can also be used outside laser cavities by using grating pair or optical fiber. In the following sections, I will briefly introduce these devices which are current widely used for dispersion management.

3.3.1. Diffraction gratings

For a long time angular dispersion has been advantageously used to resolve spectra or for spectral filtering, utilizing the spatial distribution of the frequency components behind the dispersive element [29]. 1969, Treacy found that this kind of angular dispersion induced from diffraction gratings can be used for introducing GVD and hence for compression of chirped pulses. Since then, devices (e.g. gratings, prisms) based on this concept have been well developed and widely used for laser dispersion management in both intra- and extra-cavity configurations.

Grating pair is a common device to compensate the positive GVD of the laser pulse. In most cases, one wishes to control GVD, and at the same time avoid the beam divergence introduced by angular dispersion. The simplest practicable solution to this problem consists of two identical elements arranged as in Fig. 3.6 for zero net angular dispersion. The first grating serves as a disperser producing GVD while the

second grating produces a parallel output ray. A linearly positive chirped pulse experiences negative dispersion by propagating through this arrangement. The frequency components of the pulse travel different optical path lengths, which results in the readjustment of the phases of those frequency components and thus recompresses the temporal envelop of the incident chirped pulse.

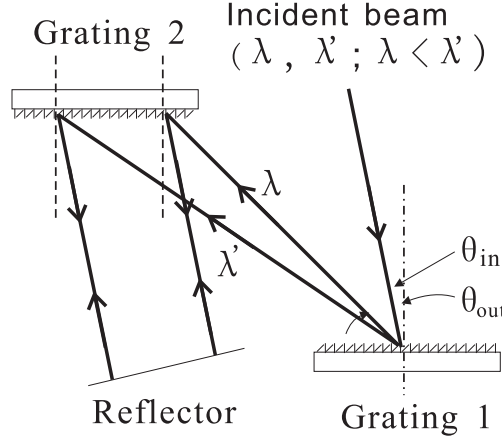


Fig. 3.6. Arrangement of diffraction gratings in the near Littrow configuration for pulse compression.

According to Treacy's results [30], the quadratic phase contribution or GVD of a grating pair system can be described as

$$GVD = \frac{\partial^2 \Phi}{\partial \omega^2} = -\frac{\lambda^3 b}{2\pi c^2 d^2 \cdot \left(1 - [\lambda/d - \sin(\theta_{in})]^2\right)^{\frac{3}{2}}} \quad (3.3)$$

Where c is the speed of light, b is the normal distance between two gratings, λ is the central wavelength of the pulse spectrum, d is the grating constant (line spacing), and θ_{in} is the incident angle which can be used to determine the diffraction angle by

$$\theta_{out} = a \sin \left[\left(\frac{\lambda}{d} \right) - \sin(\theta_{in}) \right] \quad (3.4)$$

Both θ_{in} and θ_{out} are assumed on the same side of the grating normal.

By using Eq. (3.3) and (3.4), we could find a suitable combination of parameters (grating constant, angle of incidence, normal distance between the gratings and the

laser wavelength) which can produce the desired amount of GVD to compensate the dispersion of the chirped pulse. It is clear from the geometry illustrated in Fig. 3.6 that the beam passing through the two gratings is not only spectrally but is also spatially dispersed, which is a result of angular dispersion of the beam's individual components introduced by the first grating. The transverse displacement of the spectral components at the output of the second grating can be compensated by using two pairs of gratings in sequence or by sending the beam once more through the first grating pair.

3.3.2. Prisms

Another widely used optical device based on the angular dispersion, is prism sequence (normally of 2 or 4 prisms). Because of their low insertion loss and continuously adjustable GVD, prism sequence is now a common component in femtosecond laser systems for controlling the net dispersion of the laser cavity. The simplest practicable configuration is shown in Fig. 3.7.

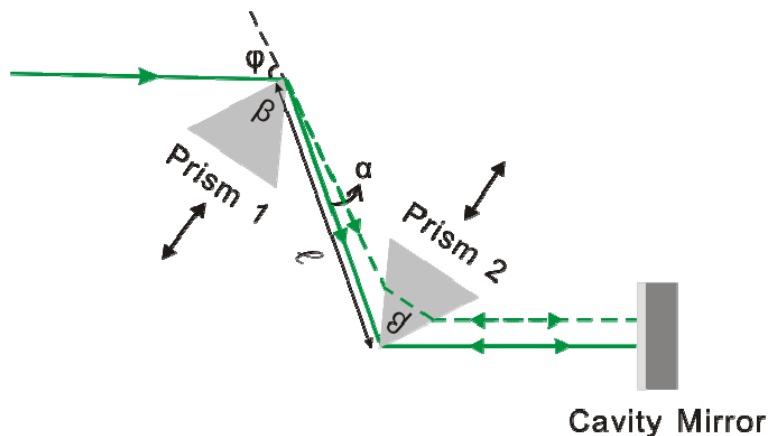


Fig. 3.7. Schematic setup of two prism sequence with adjustable GVD

It consists of two identical prisms and a cavity mirror. The first prism disperses the laser light and hence produces GVD while the second one produces a parallel output ray. However single pass through the two prisms would result in transverse displacement of spectral components. In order to compensate this displacement and

reunite all spectral components spatially, one can either use a reflector to feed the output light back to the prism pair or use four identical prisms. As shown in Fig. 3.7, if the cavity mirror is used as an end mirror which does not transmit any light, only one prism pair is needed. However, if the cavity mirror serves as an output coupling mirror, then four prisms are required to avoid the transverse displacement. A knife-edge or a slit can also be introduced into spatially dispersed beam between the second prism and the cavity mirror to enable wavelength tuning.

For minimum deviation and Brewster-angle incidence, the GVD as a function of frequency introduced by an intra-cavity prism pair is given as [31]

$$GVD = \frac{d^2\phi_p}{d\omega^2} = \frac{\lambda^3}{2\pi^2 c^2} \left(\frac{d^2P}{d\lambda^2} + l_p \frac{d^2n}{d\lambda^2} \right) \quad (3.5)$$

where $\frac{\lambda^3}{2\pi^2 c^2} \frac{d^2P}{d\lambda^2}$ is the angular dispersion and P is the total optical path length,

$\frac{\lambda^3}{2\pi^2 c^2} \cdot l_p \cdot \frac{d^2n}{d\lambda^2}$ is the material dispersion induced from the intra-prism material and

l_p is the intra-prism path length; n is the refractive index at different wavelength λ .

The term $\frac{d^2P}{d\lambda^2}$ is described as

$$\frac{d^2P}{d\lambda^2} = 4 \left[\frac{d^2n}{d\lambda^2} + (2n - n^{-3}) \left(\frac{dn}{d\lambda} \right)^2 \right] \cdot l \sin(\alpha) - 8 \left(\frac{dn}{d\lambda} \right)^2 \cdot l \cos(\alpha) \quad (3.6)$$

The first and second derivatives of the refractive index with respect to wavelength $\frac{dn}{d\lambda}$ and $\frac{d^2n}{d\lambda^2}$ can be calculated by differentiating the Sellmeier formula for $n(\lambda)$ [32].

3.3.3. Gires-Tournois Interferometer (GTI)

A GTI is an optical standing-wave cavity designed to generate chromatic dispersion [33]. The front mirror is partially reflective, while the back mirror has a high

reflectivity, as shown in Fig. 3.8.

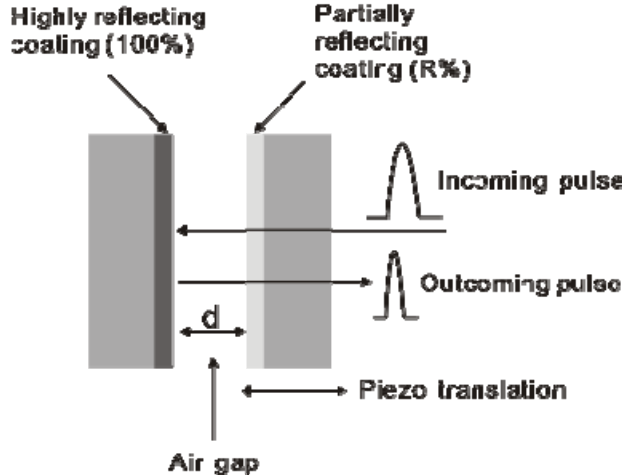


Fig. 3.8. Schematic structure of a typical Gires-Tournois Interferometers

If no losses occur in the cavity, the power reflectivity is unity at all wavelengths. However due to the fact that different component waves pass a different number of times between two mirrors and therefore experience different delays, the phase of the reflected light is thus frequency-dependent causing group delay dispersion (GDD) The amount of dispersion can be calculated by using following equation [33]:

$$\frac{\partial^2 \Phi}{\partial \omega^2} = -\frac{2(1-R) \cdot \sqrt{R} \cdot (2d/c)^2 \cdot \sin(\varphi - \omega(2d/c))}{[1 + R - 2\sqrt{R} \cdot \cos(\varphi - \omega(2d/c))]^2} \quad (3.7)$$

where R is the reflectivity of the front surface, d is the thickness of the air gap, c is the optical velocity and φ accounts for the phase change at the highly reflecting surface. The phase change of reflected light and the GDD as well as higher-order dispersion is negligible. No dispersion exists exactly on resonance or anti-resonance. However positive or negative dispersion can be obtained between these points. Ideally, GTI is operated near a minimum of the GDD, and the usable bandwidth is some fraction of free spectral range, which is inversely proportional to the cavity length d . According to Eq 3.7, the maximum amount of GDD scales with the square of the cavity length. Therefore, tunable dispersion can be obtained simply by varying

the thickness of the air gap. However careful stabilization is required to avoid unwanted drifts. GTI can also be designed to be monolithic structure without air gap. This kind device is demonstrated to be more stable but in general less tenability of GDD. The monolithic designs can be based on thin films of dielectric media like TiO₂ and SiO₂. The main drawbacks of the GTI are the fundamentally limited bandwidth (for a given amount of GDD) and the limited amount of control of higher-order dispersion.

3.3.4. Self-phase modulation (SPM)

In the transparent region of many materials, the refractive index depends nonlinearly on the propagating field. This implies refractive index varying in time and space. For temporal variation, different parts of the pulse thus experience different refractive indices which lead to a phase change across the pulse and thus a pulse chirp. We call this process self-phase modulation (SPM). The nonlinear index of a material which depends on the time dependence of a light pulse intensity envelope can be described as [34]

$$n(t) = n_0 + n_2 \cdot |\tilde{\xi}(t)|^2 = n_0 + \bar{n}_2 \cdot I(t) \quad (3.8)$$

where $\bar{n}_2 = 2n_2 / (\epsilon_0 c n_0)$, $\tilde{\xi}(t)$ is the slowly varying envelope and $I(t)$ is the intensity, n_2 is the nonlinear index coefficient describing the strength of the coupling between the electric field and the refractive index. The order of magnitude of the coefficient n_2 (in units of cm²/W) is 10⁻¹⁶ to 10⁻¹⁴ in glasses, 10⁻¹⁴ to 10⁻⁷ in doped glasses, 10⁻¹⁰ to 10⁻⁸ in organic materials, and 10⁻¹⁰ to 10⁻² in semiconductors. The electric field is expressed by [34]

$$\tilde{\xi}(t) = \xi_0 \cdot e^{i(\omega_0 t + \Phi(t))} \quad (3.9)$$

$$\Phi(t) = -k(t)d = -\frac{2\pi}{\lambda_0} n(t) \cdot d \quad (3.10)$$

where ω_0 and λ_0 are the angular frequency and wavelength, $\Phi(t)$ is the phase change

by SPM after passing a medium of length d . The instantaneous frequency, being the time derivative of the phase can be written as [34]

$$\omega(t) = \frac{\partial}{\partial t}(\omega_0 t + \Phi(t)) = \omega_0 - \frac{\omega_0}{c} \frac{\partial n(t)}{\partial t} d \quad (3.11)$$

From Eq. 3.11 we see that the phase modulation induced by SPM is different from that of GVD, which broadens the pulse duration but remains the spectrum unaffected. SPM generates new frequency components and broadens the pulse spectrum but keeps the pulse envelope (pulse duration) unchanged since SPM itself is not a dispersive effect.

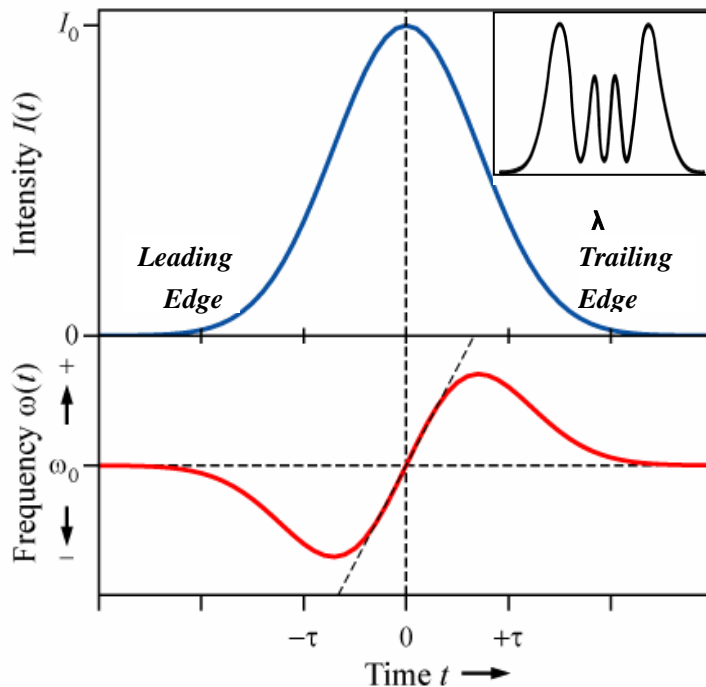


Fig. 3.9. Unchirped laser pulse profile (upper one) and the instantaneous frequency of the pulse experienced SPM. The inset is an example of the channelled spectrum caused by SPM. After [35]

Fig. 3.9 gives the examples of the chirp and spectrum of self-phase modulated pulses. The new frequency components are created in both leading edge and trailing edge of the pulse envelope. For a positive nonlinear refractive index n_2 , the central part of the laser pulses is upchirped (higher frequencies travel more slowly than lower frequencies). The channelled spectrum is caused by the constructive/destructive interference of pairs of waves with identical frequencies created at two different time

delays. Since the central part (contains most of the energy) of the pulse is linear chirped, pulse compression can be obtained by using optical devices providing linear dispersion with opposite sign.

3.3.5. Optical fiber

The chromatic dispersion in single mode fibers can be used to compress the linearly chirped laser pulses. The chromatic dispersion consists of material dispersion and waveguide dispersion. Since waveguide contribution to the dispersion is relative small compared with material contribution except near the zero-dispersion wavelength where two become comparable [36], we therefore can neglect waveguide effect here. If the propagating laser field is strong enough, the refractive index will change nonlinearly with the field. This is known as self-phase modulation of fibers, which has been reviewed in [37]. Therefore, when the ultra-short pulses with high peak powers propagate through a fiber, the effects associated with the interplay of the dispersion and SPM must be considered. The dispersion parameter of silica fibers can be expressed as [38]

$$k'' = \frac{d^2 k}{d\omega^2} = -\frac{D_\lambda \lambda^2}{2\pi c} \quad (3.12)$$

D_λ (ps/nm km) is the dispersion coefficient of an optical fiber. It describes the group delay in ps per nm wavelength per km propagation distance. Figure 3.10 shows the wavelength dependence of the dispersion coefficient of silica glass. It is shown that zero-dispersion wavelength is around $1.3\mu\text{m}$. The dispersion coefficient for wavelength around $1\mu\text{m}$ is about -50ps/nm km .

The behaviour of ultra-short pulses propagating through single-mode fibers is different in the spectral range where $k''>0$ ($D_\lambda<0$) and $k''<0$ ($D_\lambda>0$). The spectral range where $k''>0$ is known as normal dispersion regime while the range where $k''<0$ is known as anomalous dispersion regime. Since the GVD has the same sign (positive dispersion) as the chirping induced by SPM in the normal dispersion regime,

the pulses would either be subsequently broadened or compressed after propagating a fiber with certain length. However for anomalous dispersion, soliton shaping may occur due to the opposite sign of the GVD and the chirp produced from SPM.

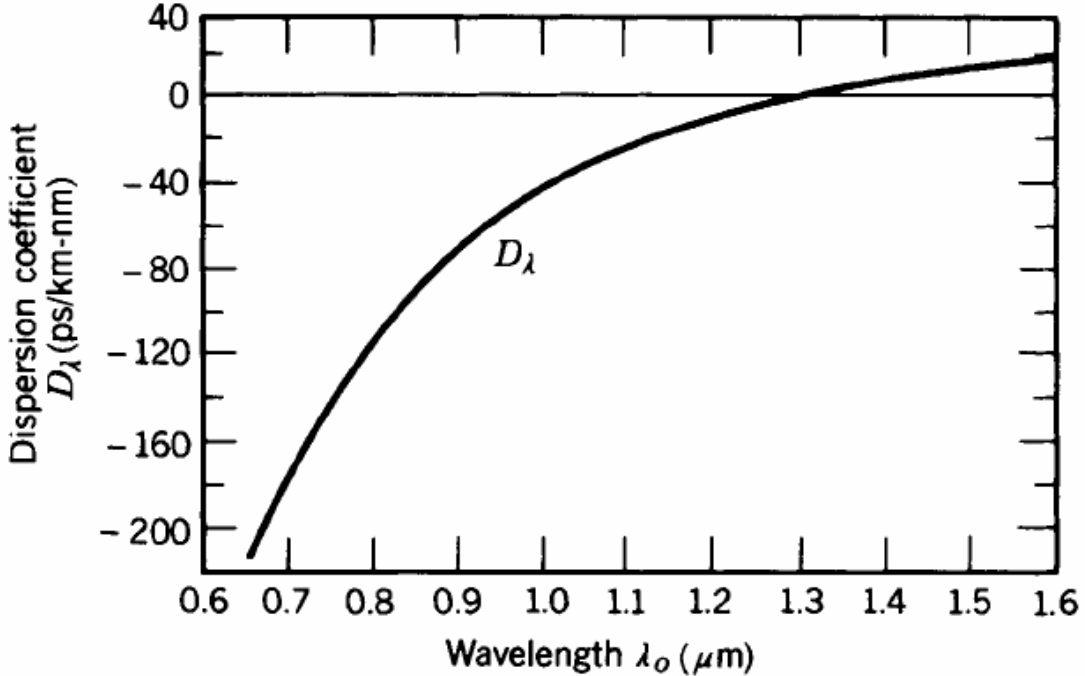


Fig.3.10. Dispersion coefficient D_λ of silica glass as a function of wavelength. After [38]

3.4. Conclusion

In conclusion, the theory of laser mode locking has been introduced. Two main categories of mode locking, active mode locking and passive mode locking, are discussed. The theory of synchronous mode locking which will be used in next chapter is also discussed. The broadening or shortening of laser pulses can be achieved by changing the dispersion of the optical elements where pulses are propagating through. Hence the physical mechanisms of five practical techniques are described. In chapter three, some techniques of laser mode locking and dispersion management described in this chapter will be applied to a typical optically pumped VECSEL so as to enable ultrashort pulse formation.

3.5. Reference

- [1]. L. E. Hargrove, R. L. Fork, and M. A. Pollack, "Locking of He-Ne laser modes induced by synchronous intra-cavity modulation," *Applied Physics Letters*, Vol. 5, No. 1, pp. 4-6, 1964.
- [2]. H. A. Haus, *Waves and Fields in Optoelectronics*, Prentice-Hall Publishing, 1984.
- [3]. D. J. Kuizenga and A. E. Siegman, "Modulator frequency detuning effects in the FM mode-locked laser," *IEEE Journal of Quantum Electronics*, Vol. 6, No. 12, pp. 803-808, 1970.
- [4]. H. A. Haus, "Mode-Locking of Lasers," *IEEE Journal on Selected Topics in Quantum Electronics*, Vol. 6, No. 6, pp. 1173-1185, 2000.
- [5]. E. P. Ippen, "Principles of passive mode locking," *Applied Physics B*, Vol. 58, No. 3, pp. 159-170, 1994.
- [6]. J. C. Diels and W. Rudolph, *Ultrashort Laser Pulse Phenomena-Fundamentals, Techniques and Applications on a Femtosecond Time Scale*, Academic Press Inc., 1996.
- [7]. C. P. Auschnitt, R. K. Jain, and J. P. Heritage, "Cavity length detuning characteristics of the synchronously mode-locked CW dye laser," *IEEE Journal of Quantum Electronics*, Vol. 15, No. 9, pp. 912-917, 1979.
- [8]. S. L. Shapiro, R. R. Cavanagh, and J. C. Stephenson, "Streak-camera observations of the pulse emission from a synchronously pumped continuous-wave mode-locked dye laser," *Optics Letters*, Vol. 6, No. 10, pp. 470-472, 1981.
- [9]. P. G. May, W. Sibbett, K. Smith, J. R. Taylor, and J. P. Willson, *Optics Communications*, Vol. 42, No. 4, pp. 285-290, 1982.
- [10]. C. P. Ausschnitt and R. K. Jain, "Pulse-width dependence on intra-cavity bandwidth in synchronously mode-locked CW dye-lasers" *Applied Physics Letters*, Vol. 32, No. 11, pp. 727-730, 1978.
- [11]. J. P. heritage and R. K. Jain, "Subpicosecond pulses from a tunable CW mode-locked dye laser," *Applied Physics Letters*, Vol. 32, No. 2, pp. 101-103, 1978.
- [12]. R. K. Jain and C. P. Ausschnitt, "subpicosecond pulse generation in a

- synchronously mode-locked CW rhodamine OG dye laser," Optics Letters, Vol. 2, No. 5, pp. 117-119, 1978.
- [13]. U. Keller, K. J. Weingarten, F. X. Kartner, D. Kopf, B. Braun, I. D. Jung, R. Fluck, C. Honninger, N. Matuschek, and J. A. derAu, "Semiconductor saturable absorber mirrors (SESAM's) for femtosecond to nanosecond pulse generation in solid-state lasers," IEEE Journal of Quantum Electronics, Vol. 2, No. 3, pp. 435-453, 1996.
 - [14]. G. H. C. New, "Mode-locking of quasi-continuous lasers," Optics Communications, Vol. 6, No. 2, pp. 188-192, 1972./ H. A. Haus, "Theory of mode locking with a slow saturable absorber," IEEE Journal of Quantum Electronics, Vol. 11, No. 9, pp. 736-746, 1975.
 - [15]. H. A. Haus, "Theory of mode locking with a fast saturable absorber," Journal of Applied Physics, Vol. 46, No. 7, pp. 3049-3058, 1975.
 - [16]. H. A. Haus, J. G. Fujimoto, and E. P. Ippen, "Structures for additive pulse mode locking," Journal of Optical Society of America B, Vol. 8, No. 10, pp. 2068-2076, 1991.
 - [17]. F. X. Kartner, and U. Keller, "Stabilization of soliton-like pulses with a slow saturable absorber," Optics Letters, Vol. 20, No. 1, pp. 16-18, 1995.
 - [18]. I. D. Jung, F. X. Kartner, L. R. Brovelli, M. Kamp, and U. Keller, "Experimental verification of soliton mode locking using only a slow saturable absorber," Optics Letters, Vol. 20, No. 18, pp. 1892-1894, 1995.
 - [19]. F. X. Kartner, I. D. Jung, and U. Keller, "Soliton mode locking with saturable absorbers: Theory and experiments," IEEE Journal of Selected Topics in Quantum Electronics, Vol. 2, No. 3, pp. 540-556, 1996.
 - [20]. J. A. Valdmanis and R. L. Fork, "Design considerations for a femtosecond pulse laser balancing self phase modulation, group velocity dispersion, saturable absorption, and saturable gain," IEEE Journal of Quantum Electronics, Vol. 22, No. 1, pp. 112-118, 1986.
 - [21]. D. E. Spence, P. N. Kean, and W. Sibbett, "60-fsec pulse generation from a self-mode-locked Ti:Sapphire laser," Optics Letters, Vol. 16, No. 1, pp. 42-44, 1991.
 - [22]. A. E. Siegman, Lasers, Oxford University Press, 1986, pp.1061-1070.
 - [23]. E. P. Ippen, H. A. Haus, and L. Y. Liu, "Additive pulse modelocking," Journal of Optical Society of America B, Vol. 6, No. 9, pp. 1736-1745, 1989.

- [24]. J. Zhou, G. Taft, C. P. Huang, M. M. Murnane, H. C. Kapteyn, and I. P. Christov, “Pulse evolution in a broad-bandwidth Ti:Sapphire laser,” Optics Letters, Vol. 19, No. 15, pp. 1149-1151, 1994.
- [25]. A. Stingl, M. Lenzner, C. Spielmann, F. Krausz, and R. Szipocs, “sub-10-fs mirror-controlled Ti:Sapphire laser,” Optics Letters, Vol. 20, No. 6, pp. 602-604, 1995.
- [26]. L. Xu, C. Spielmann, F. Krausz, and R. Szipocs, “Ultrabroadband ring oscillator for sub-10-fs pulse generation,” Optics Letters, Vol. 21, No. 16, pp. 1259-1261, 1996.
- [27]. F. X. Kartner, D. Kopf, and U. Keller, “Solitary pulse stabilization and shortening in actively mode-locked lasers,” Journal of Optical Society of America B, Vol. 12, No. 3, pp. 486-496, 1995.
- [28]. D. Kopf, F. Kartner, K. J. Weingarten, and U. Keller, “Pulse shortening in a Nd: glass laser by gain reshaping and soliton formation,” Optics Letters, Vol. 19, No. 24, pp. 2146-2148, 1994.
- [29]. J. C. Diels and W. Rudolph, Ultrashort Laser Pulse Phenomena-Fundamentals, Techniques, and Applications on a Femtosecond Time Scale, Academic Press Inc., 1996.
- [30]. E. B. Treacy, “Optical pulse compression with diffraction gratings,” IEEE Journal of Quantum Electronics, Vol. 5, No. 9, pp. 454-458, 1969.
- [31]. R. L. Fork, O. E. Martinez, and J. P. Gordon, “Negative dispersion using pairs of prisms,” Optics Letters., Vol. 9, No. 5, 1984.
- [32]. M. Bass, E. W. V. Stryland, D. R. Williams, and W. L. Wolfe, Handbook of Optics- Fundamentals Techniques and Design, 2ed Eds, McGraw-Hill Inc., 1995.
- [33]. F. Gires, and P. Tournois, “Interferometer utilisable pour la compression d’impulsions lumineuses modules en fréquence,” Comptes Rendus de l’Académie des Sciences, Vol. 258, No. 5, pp. 6112-6115, 1964.
- [34]. J. C. Diels and W. Rudolph, Ultrashort Laser Pulse Phenomena-Fundamentals, Techniques and Applications on a Femtosecond Time Scale, Academic Press Inc., 1996.
- [35]. Wikipedia, http://en.wikipedia.org/wiki/Self-phase_modulation.
- [36]. H. Murata and N. Inagaki, “Low-Loss Single-Mode Fiber Development and

- splicing Research in Japan," IEEE Journal of Quantum Electronics, Vol. 17, No. 6, pp. 835-849, 1981.
- [37]. G. P. Agrawal, Nonlinear Fiber Optics, 3rd Eds, Academic Press, 2001.
- [38]. J. C. Diels and W. Rudolph, Ultrashort Laser Pulse Phenomena-Fundamentals, Techniques and Applications on a Femtosecond Time Scale, Academic Press Inc., 1996.
- [39]. B. E. A. Saleh, M. C. Teich, Fundamentals of Photonics, John Wiley & Sons Inc., 1991.

Chapter Four

Synchronous mode-locking of VECSEL

4.1. Introduction

This chapter describes the behavior of a room temperature synchronously mode-locked VECSEL operating at 980nm. The cavity detuning effects of the laser are studied and discussed. Chirp compensation of the laser pulse is explored. Multiple pulsing was observed and the origin of this phenomenon was studied.

4.2. Overview

Optically pumped VECSEL combine the advantages of multiple quantum well semiconductor lasers with optical pumping. Hence, they have the potential to generate high output powers with excellent beam quality. VECSEL technology is maturing rapidly and is finding applications in many diverse areas of science ranging from high-resolution spectroscopy through to medical imaging [1]. The broad gain bandwidth associated with the multiple quantum well system means that the VECSEL should be an ideal source for the production of ultrashort pulses. To date most research effort aimed at the generation of ultrashort pulses from VECSEL systems has concentrated on the passive mode-locking approach with a semiconductor saturable absorbing mirror (SESAM) acting as the mode-locking element [2]. With this approach sub-picosecond pulses have been generated with repetition rates in the 10's GHz regime [3]. Such high repetition rates are ideal for communications applications, however the low peak power (\sim 10W) associated with

the generated pulses, which is a direct consequence of the high repetition rate, makes the passive mode-locking approach using a SESAM unsuitable for many other applications such as two-photon fluorescence microscopy for biological imaging, or frequency conversion applications, where high peak powers are needed. Furthermore, low repetition rates in the hundred of MHz range are beneficial in the biological imaging applications due to the lifetimes of the typical dyes used.

An alternative mode-locking technique is required in order to generate ultrashort pulses at low repetition rates from a VECSEL system. The most obvious approach is to use an active mode-locking technique whereby an external drive signal is used to induce the necessary mode coupling to produce the desired short pulse [4]. However, the carrier lifetime in a VECSEL is of the order of nanoseconds making active mode-locking somewhat problematic. First, the average power drops in proportion to the drop in repetition rates for round trip times that are greater than the storage time. Second the system has a propensity to multiple pulsing for repetition rates lower than the inverse of the storage time.

Some of these problems can be overcome by the use of synchronous pumping where the pump laser is mode-locked and a VECSEL cavity length is matched to the pump laser repetition rate. Synchronous pumping of VECSELs should be an attractive option for generating high peak power pulses and indeed it has shown previously that it is possible to synchronously mode-lock a vertical cavity semiconductor laser in an external cavity configuration based on GaAs (wavelength of 880-890nm) or InGaAs/InP (wavelength of $1.5\mu\text{m}$) material [5-7, 23]. In most of those systems the gain medium comprised of many (120-200) quantum wells [5-7] and - at least in the case of the InGaAs/InP material - the laser operation temperature was very low (77K). In this communication we describe our work on the synchronous mode-locking of a room temperature VECSEL at 980nm with a gain medium containing 14 single quantum wells placed in a resonant periodic gain structure. We find that, although the pulses are severely chirped by self-phase modulation (SPM), it

is possible to externally compress that pulses to a duration of less than 200fs. The dependence of the laser characteristics on detuning is systematically investigated in order to identify the potentials of the scheme.

4.3. Experimental Setup

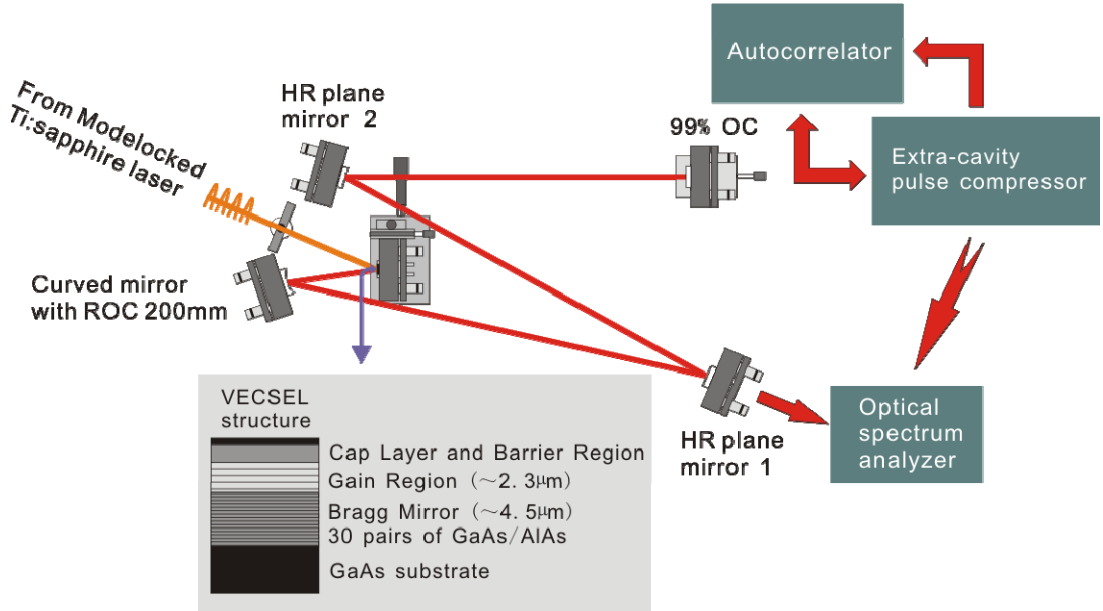


Fig. 4.1. Experimental setup for the mode-locking of a VECSEL synchronously pumped by a Ti:Sapphire laser (ROC radius of curvature); the schematic structure of the VECSEL sample is shown at the bottom, the thickness of the gain region, bragg mirror is around $2.3\mu\text{m}$ and $4.5\mu\text{m}$ respectively.

The semiconductor wafer sample used as the gain medium in this work was grown by a commercially MOCVD to our specifications. The mirror-on-substrate structure of the wafer and the set-up of the resonator are both shown in Fig. 4.1. A highly reflective (HR) DBR, made from 30 GaAs-AlAs layers, was deposited onto a GaAs substrate. On top of this HR mirror a gain region was grown containing 14 $\text{In}_{0.15}\text{Ga}_{0.85}\text{As}$ quantum wells (QWs), each 8nm thick. Spacing layers of a 103nm thick $\text{Al}_{0.06}\text{Ga}_{0.94}\text{As}$ barrier and a 2.9nm GaAsP strain-compensating layer were used to separate each QW. An $\text{Al}_{0.3}\text{Ga}_{0.7}\text{As}$ layer was used to cap the structure. The 3mm x 3mm sized sample was cleaved from the wafer and bonded to a copper heat-sink by using indium foil. The back surface of the sample was roughened so as to minimize

the etalon effect of the substrate layer.

The resonator consists of the HR Bragg mirror, a mirror of 200mm radius of curvature, two plane HR mirrors and a 0.88% transmitting output mirror which was mounted on a translatable stage providing cavity length adjustment. The distance between the HR Bragg mirror and the curved mirror was 103mm and between the curved mirror and the output coupling mirror was 1.761m. This gives a cavity mode size of 32 μ m radius on the sample. Two flat HR mirrors were used between the curved mirror and the output coupling mirror in order to fold the cavity. The round trip time of cavity was matched to the repetition rate of the pump laser at around 80MHz. The pump pulses were generated by a Kerr-lens mode-locked Ti sapphire laser (Spectra-Physics Tsunami 3960 S3S) which can provide both 3.6ps pump pulse with a maximum average power at the sample of 450mW at a central wavelength of 796nm and 70fs pulse with a maximum average power of 450mW at a central wavelength of 791nm. The pump pulses were focused into the gain medium by a lens relay system designed to match the pump mode to the laser cavity mode. The temporal profile of the pulses produced from the synchronously pumped VECSEL was monitored using an autocorrelator (APE pulsecheck) that had a 50ps sampling window and the spectral profile of the pulses was observed by use of an optical spectrum analyzer (OSA, HP 86140).

4.4. Experimental Results

4.4.1. Synchronous pumping with 70 fs pulse

In this case, the VECSEL was pumped by 70fs Sech² pulses with an average incident power of 450mW. By carefully aligning the laser cavity, a maximum output power of ~40mW was obtained and the operating wavelength was 974.3nm. The cavity length, where the maximum average output power was achieved, was assumed to be the matching length. The full width half maximum (FWHM) detuning range where the

power dropped to half its value was about $200\mu\text{m}$. However, the quality and duration of the pulses depend strongly on the timing mismatch and good quality pulses can be only achieved in a much smaller region.

4.4.1.1. Cavity detuning effects

The laser power was firstly recorded as the cavity length mismatch was varied, as shown in Fig. 4.2. The detuning range where the power dropped to half its value was about $200\mu\text{m}$ (FWHM). The inset of the figure illustrates the average output power of the laser increased with pump power when the cavity was set to be optimal length.

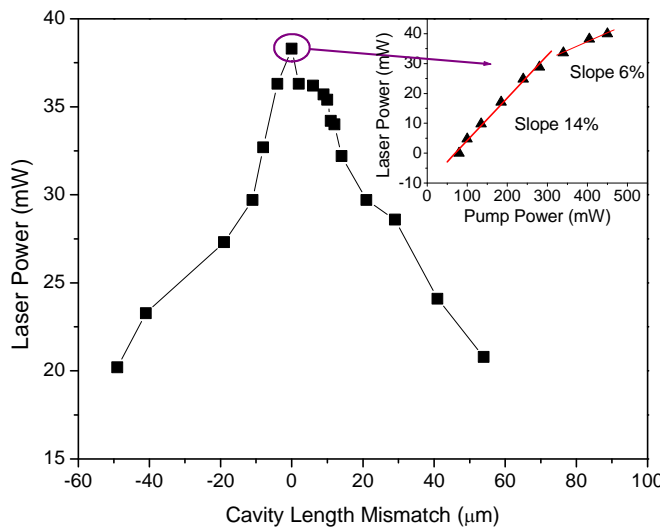


Fig. 4.2. Laser average output power as a function of cavity length mismatch (fs pumping without BRF); the inset shows the laser power increases with pump power at optimal cavity length.

Figure 4.3 shows how the autocorrelation traces and the spectra change with the amount of cavity length mismatch. If the cavity was much shorter than the optimal length, the lasing pulse was very broad. The autocorrelation trace contains a coherence spike, which indicates the presence of substructure in the pulse [8]. As the cavity was lengthened, the coherence spike disappeared and the pulse duration narrowed till the laser cavity was set to be close to the matching point. During this process, the spectral width of the pulses increased and the peak wavelength shifts

towards higher wavelengths. Around the matching point, modulations in the autocorrelation traces were observed, which are believed to be caused by satellite pulses (described and analyzed in the following in more detail). The spectral width increased considerably, when the cavity length was lengthened, reaching a maximum of 6.1nm (FWHM) at a length 9 μ m longer than the optimum length. During this process a coherence spike started to appear on the top of the autocorrelation traces. Beyond a cavity mismatch of 9 μ m, spectra and autocorrelation traces began to narrow again and the peak wavelength shifts back towards short wavelengths again. Finally, the laser was not mode locked anymore and the pulses were rather broad.

The pulse duration varied in the range of 10 – 40ps as the cavity length was changed and hence was far (at least 10 times than) from the inherent limit (a few hundred femtoseconds) imposed by the spectral width of the VECSEL. We attribute this to the frequency chirp imposed on the pulse by the phase modulation occurring in the gain medium due to the optical pumping and gain saturation. We mention also that the laser was unpolarized with about equal power in the horizontal and vertical direction. In order to improve the quality of laser pulses as well as controlling the spectrum and polarization, a 1mm thick single plate BRF was put into the laser cavity at Brewster's angle. And the resulting autocorrelation traces and the spectra are shown in Fig. 4.4. As shown in Fig. 4.5, by detuning the cavity length, maximum output power of 27.3mW at a pump power of 450mW was obtained. The mismatch sensitivity of the average power is again about 200 μ m (FWHM). Compared to the spectra of the laser without a BRF, the widths of the spectra are reduced. In addition, the phenomenon of multiple pulses is much clearer and more strongly pronounced. Since the multiple pulsing only appears in a very short region (\sim 10 μ m), it is difficult to accurately resolve the scenario by using a mechanical translation stage for controlling the cavity length.

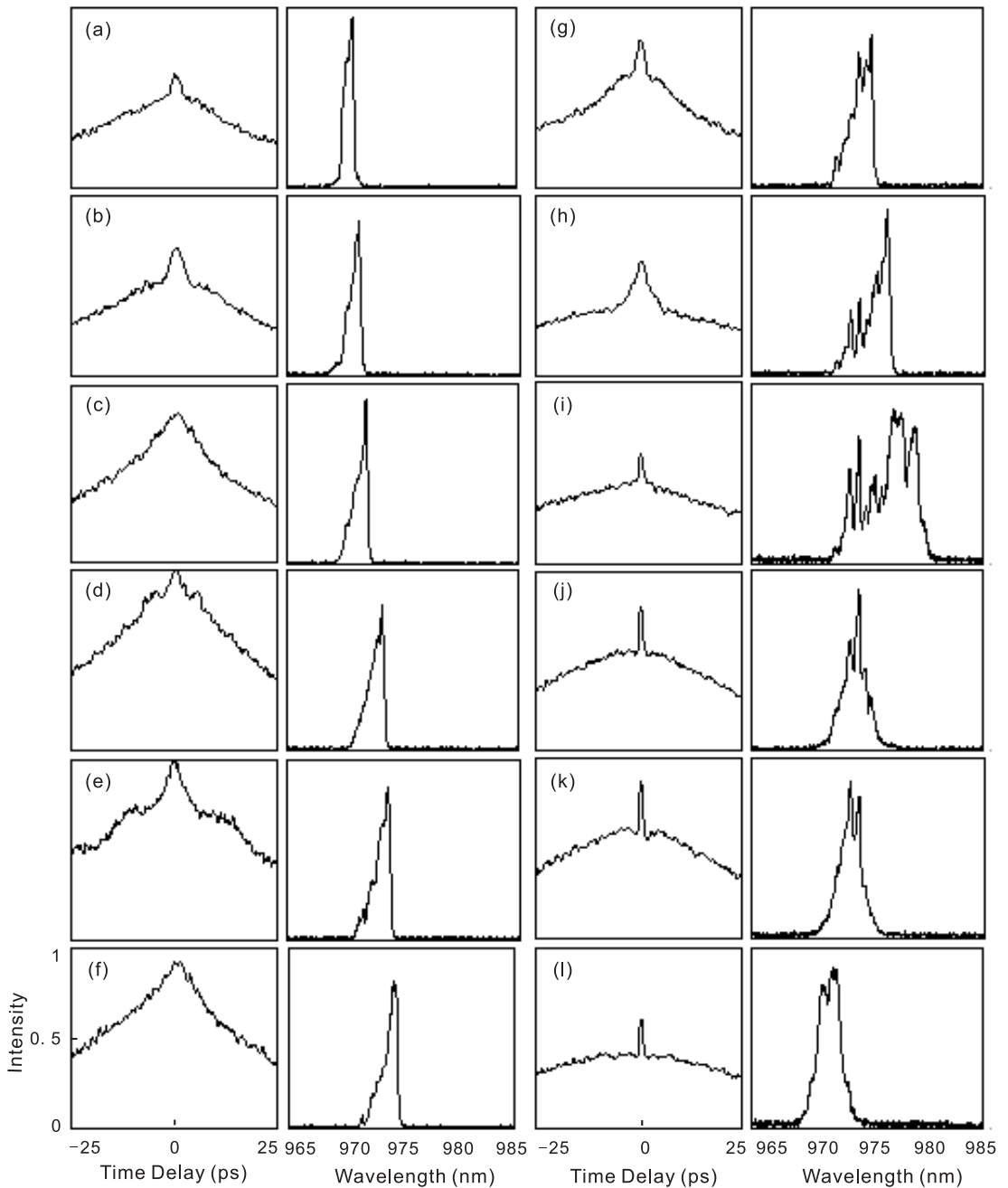


Figure 4.3. Series of autocorrelation traces of pulses (left hand side) and spectrum (right hand side) obtained from VECSEL at different settings of the cavity length (fs-pumping): (a) $-19\text{ }\mu\text{m}$; (b) $-11\text{ }\mu\text{m}$; (c) $-8\text{ }\mu\text{m}$; (d) $-4\text{ }\mu\text{m}$; (e) $-1\text{ }\mu\text{m}$; (f) $0\text{ }\mu\text{m}$; (g) $+2\text{ }\mu\text{m}$; (h) $+6\text{ }\mu\text{m}$; (i) $+9\text{ }\mu\text{m}$; (j) $+11\text{ }\mu\text{m}$; (k) $+12\text{ }\mu\text{m}$; (l) $+21\text{ }\mu\text{m}$.

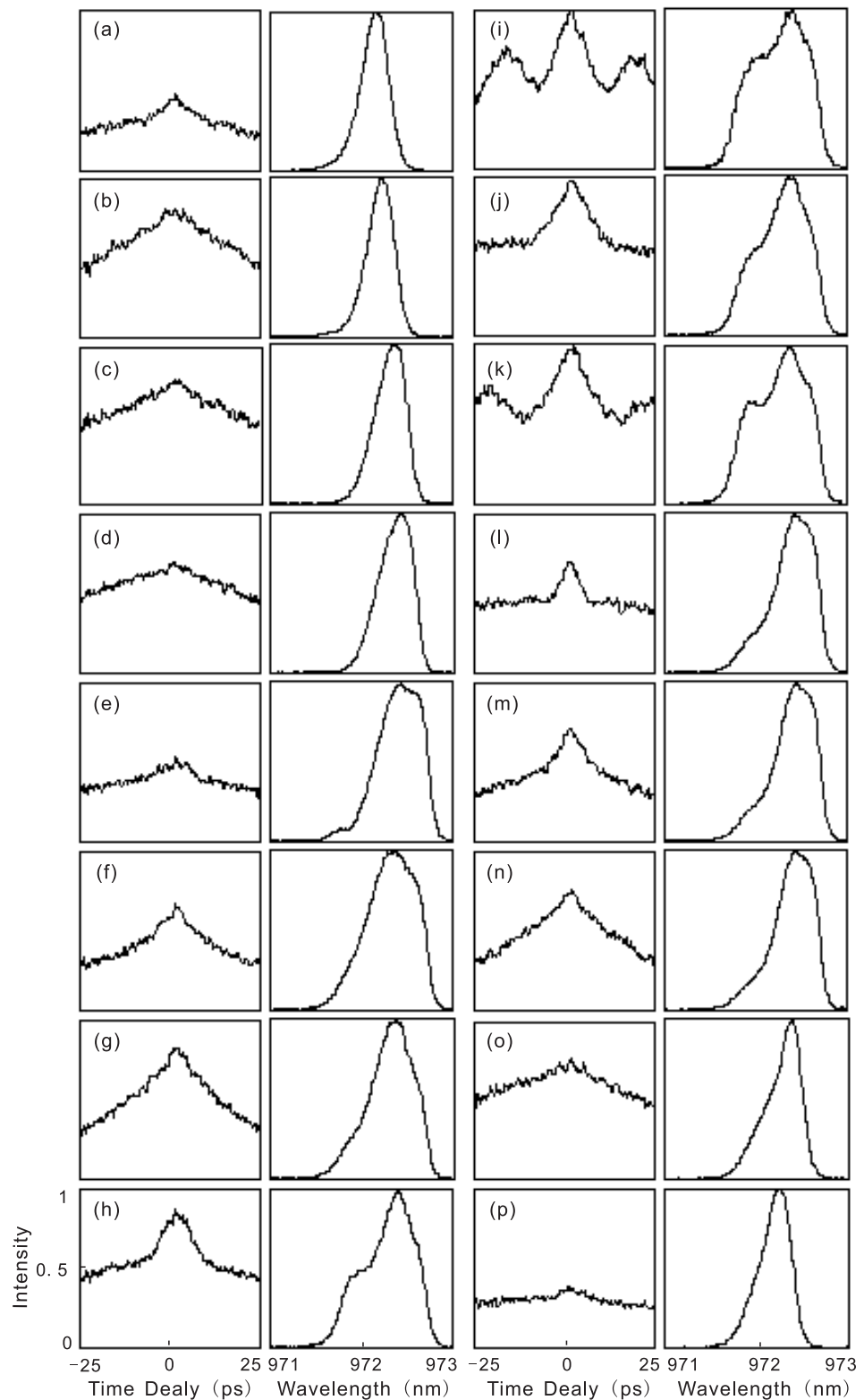


Fig. 4.4. Series of autocorrelation traces of pulses (left hand side) and spectrum (right hand side) obtained from VECSEL with BRF at different settings of the cavity length (fs-pumping): (a) -78 μm; (b) -45 μm; (c) -30 μm; (d) -23 μm; (e) -15 μm; (f) -11 μm; (g) -8 μm; (h) -2 μm; (i) -1 μm; (j) 0 μm; (k) +1 μm; (l) +3 μm; (m) +8 μm; (n) +12 μm; (o) +38 μm; (p) +71 μm;

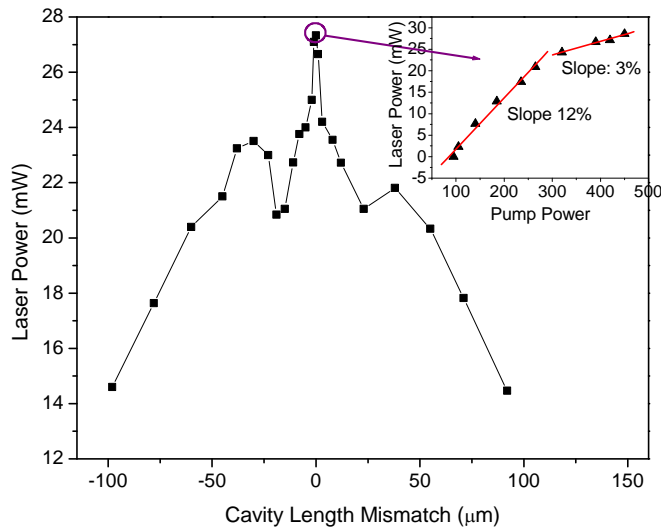


Fig. 4.5. Laser average output power as a function of cavity length mismatch (fs pumping with BRF); the inset shows the laser power increases with pump power at optimal cavity length.

Hence a piezoelectric transducer with an expansion parameter of 4.5nm/V was attached to one of the plane HR mirrors of the laser cavity. The maximum movement of the piezoelectric transducer was limited to $4.5\mu\text{m}$ by the 1000V power supply available. After realigning the cavity to get maximum output, the operating wavelength of the laser shifted to 973nm , but this did not affect the observations. Figure 4.6 shows the changes in the multiple pulse structure around the matching length by continuously tuning the voltage applied to the piezoelectric transducer. For a short cavity length, the central pulse was strong and the satellite pulses were weak and far away from the central one. When the cavity was lengthened, the satellite pulses became stronger and moved closer to the central pulse. This change stopped at some cavity length, from where the satellite pulses started to move away from the central pulse again and died out gradually. If the cavity is lengthened further, the amplitude of the central pulse jumped up again showing weak satellite pulses and a similar sequence repeated. As shown in Fig. 4.4, the spectra typically show indications of a shoulder or additional bump at both cavity detuning lengths of $-1\mu\text{m}$

and $+1\mu\text{m}$. The closer the satellite pulses moved toward the central pulse, the stronger the bump in the spectrum. One possible interpretation is that the different parts of the spectrum actually correspond to different pulses. The origin of the satellite pulses is the dynamic interaction between the intra-cavity circulating pulses and the gain, which will be discussed in section 4.5.3.

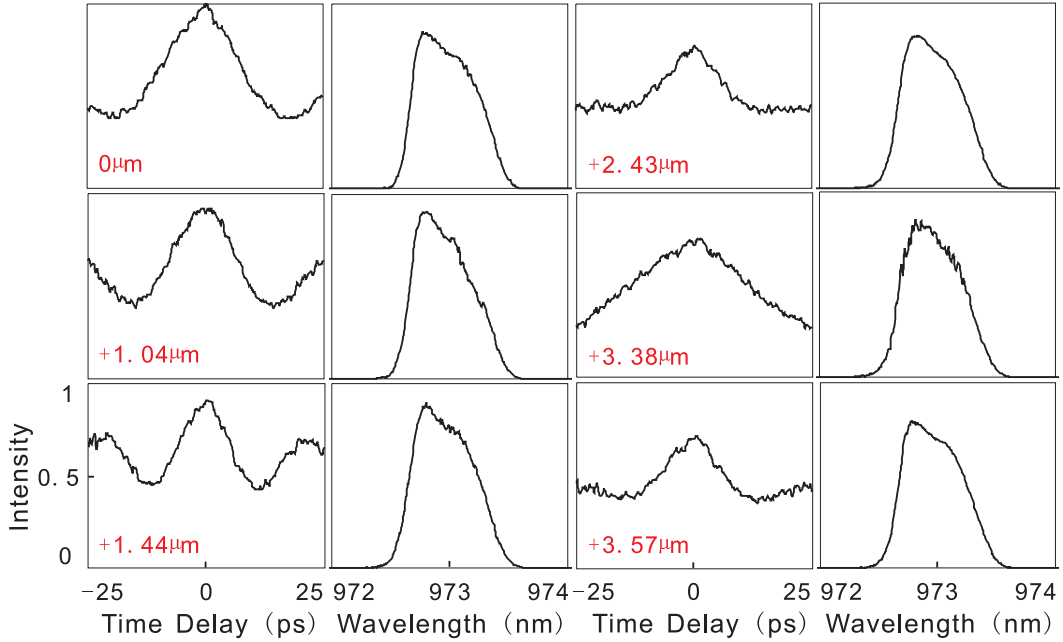


Fig. 4.6. Series of autocorrelation traces of pulses (left hand side) and spectrum (right hand side) obtained from VECSEL with BRF around the optimum cavity length (fs-pumping).

4.4.1.2. Extra-cavity compression of pulses

In order to compensate the chirp of the pulse, we employed a grating pair compressor whose operating principle has been introduced in chapter three (section 3.3.1). The grating pair compression was accomplished by double-pass transmission of pulses from the VECSEL through a pair of identical 1200lines/mm diffraction gratings. According to Eq. 3.3, the required dispersion can be obtained by simply choosing a proper distance between two gratings.

For the case without the BRF, a short pulse with a FWHM of the autocorrelation

trace of 377fs (shown in Fig. 4.7(a) was obtained when the separation between the two gratings was set to be 31cm. Here the laser cavity was tuned close to a position slightly shorter than the matching length where the spectral bandwidth was maximum. If a hyperbolic secant profile is assumed, the measured autocorrelation function corresponds to pulse duration of 244fs. The spectral bandwidth was measured to be 4.3nm. Hence, the time-bandwidth product was 0.33, i.e., the pulse is nearly transform-limited. The average power after passing the grating pair compressor was about 8.5mW. So the peak power of the laser pulse was calculated to be 435W. The chirp of the initial pulse can be estimated from the dispersion of the grating-pair to be about 20ps² (by using Eq. 3.3). It is up-chirped.

If the cavity length was increased beyond the point where the laser had the broadest spectrum (denoted as ‘switching point’ in this paper), compression was not achieved anymore. This indicated that the sign of the chirp of the laser pulses reversed from positive to negative or that the pulse did not have a simple linear chirp at all.

Hence a piece of standard telecommunication fibre working in the normal dispersion region was used to test the possibility of compression. Focused by a lens with 4.5 mm focal length, the laser light was directly launched into a 220m long fibre with coupling efficiency of 55% to 60%. Effective pulse compression by the fibre was achieved when the laser cavity was slightly lengthened beyond the switching point. The autocorrelation trace in Fig. 4.7(b) is the compressed pulse with a width of 925fs (FWHM) corresponding to a pulse duration of 600fs (assuming a hyperbolic secant profile). The time bandwidth product was 0.9. The average power emerging from the fibre was 22mW so the peak power of the pulse was then about 458W. The small pedestal is probably caused by the nonlinear chirp under the wings which could not be compensated. When the laser cavity was lengthened even further, the spectrum of the laser started to fluctuate strongly. This indicated that feedback from the fibre was affecting the laser. However no such feedback was observed when a short piece (30cm) of fibre was used. The feedback effect was believed to be caused by

nonlinear effects such as Stimulated Brillouin Scattering (SBS) inside the fibre. At that region, a nearly transform-limited but unstable pulse with an autocorrelation width of 300fs (pulse duration of approximately 200fs) was observed. The peak power of the compressed pulse was 1.4kW. This experiment demonstrates that not only the pulse width and the laser spectrum depend on the cavity length mismatch, but also the sign of the chirp of the laser pulse.

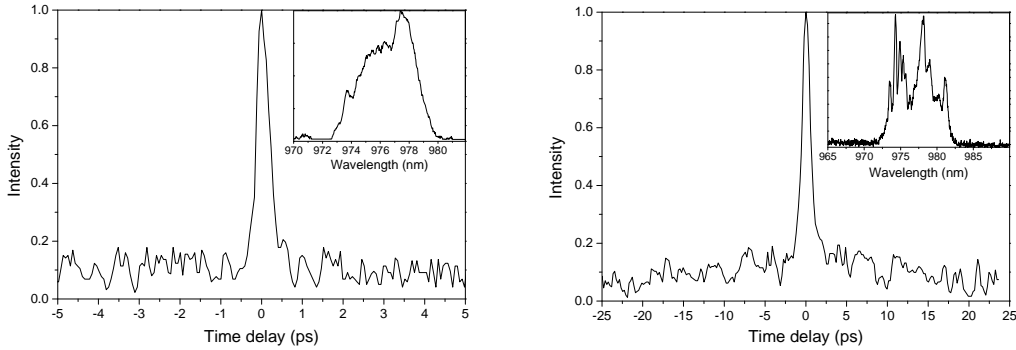


Fig. 4.7. Autocorrelation and spectrum of the compressed pulses (fs-pumping, without BRF): (a) up-chirped pulse was compressed to 244fs (assuming a hyperbolic secant profile; cavity detuning length was around $+8\mu\text{m}$); (b) down-chirped pulse was compressed by fiber to 600fs (assuming a hyperbolic secant profile; cavity detuning length was around $+10\mu\text{m}$)

Pulse compression for the case of an intra-cavity BRF was also investigated by using the same grating pair separated 65cm apart. The shortest pulses were obtained, if the cavity length was adjusted to be in the region with multiple pulses. The shortest autocorrelation width obtained was 4.2ps (see Fig. 4.8(a)) corresponding to a pulse width of 2.7ps, if a hyperbolic secant profile is assumed. The time bandwidth product for this pulse was 0.5. This experimental result indicates that the pulses were up-chirped (about 40ps^2). By tuning the laser to generate strongest satellite pulses and meanwhile changing the zero position for the autocorrelator; we found that the satellite pulses were compressed as well, shown in Fig. 4.8(b). This could possibly explain why the compressed pulse has some background and noisy wings, as the wings of the satellite pulses could overlap the central pulse.

All the experimental results on chirp compensation demonstrated that the laser pulses have very strong chirping induced by the phase modulation in the active region of the semiconductor gain medium.

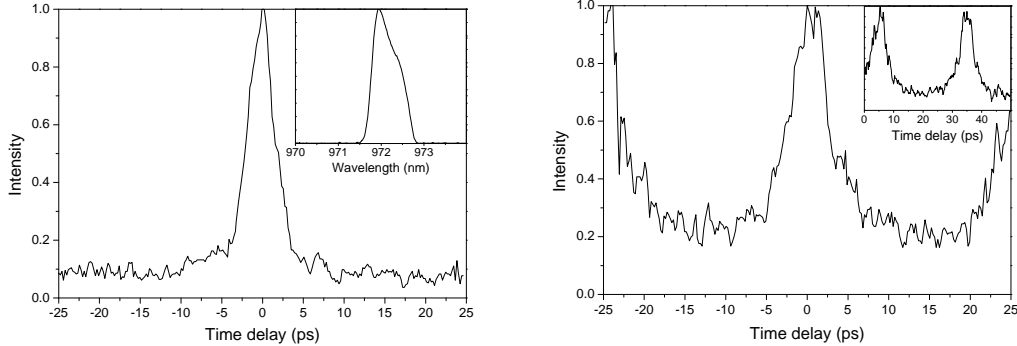


Fig. 4.8. Autocorrelation and spectrum of the compressed pulses profile (fs-pumping, with BRF): compression for primary pulse with weak satellite pulses and pulse duration was 2.7ps (assuming a hyperbolic secant profile; cavity detuning length was around $-8\mu\text{m}$); (b) compression for primary pulse with strong satellite pulses profile (cavity detuning length was $-1\mu\text{m}$ and $+1\mu\text{m}$, shown in Fig. 3); The inset shows both primary pulse and satellite pulse after shifting the zero position of time axis (region shown -40 to +10ps, SP= satellite pulse, PM= primary pulse).

4.4.2. Synchronous pumping with 3.6 ps pulse

If pumped with 3.6ps pulses, the VECSEL had an average pump power threshold of 70mW. When excited with an average pump power of 420mW, it gave an average output power of 27mW at a wavelength of 972nm. The detuning characteristics were found to be quite similar to the case of fs-pumping.

4.4.2.1. Cavity detuning effects

Again, the average output power of the laser was ministered as the cavity length was detuned. As Fig. 4.9 shows, the FWHM detuning range in output power was measured to be about $150\mu\text{m}$.

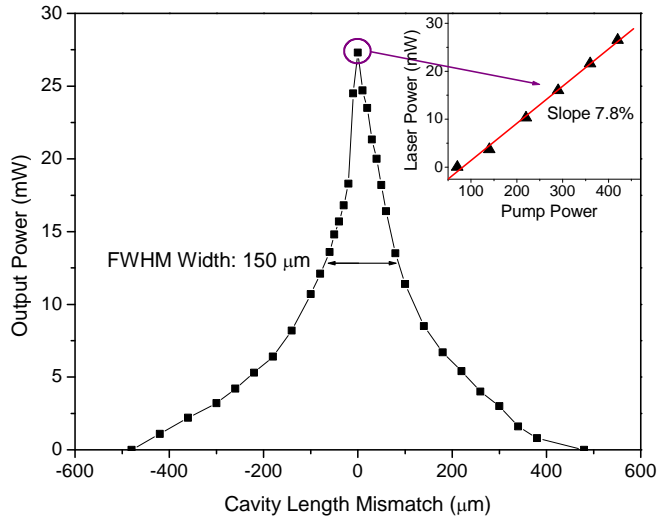


Fig. 4.9. Laser average output power as a function of cavity length mismatch (ps pumping without BRF); the inset shows the laser power increases with pump power at optimal cavity length.

Figure 4.10 shows how the autocorrelation traces and the spectra change with the amount of cavity length mismatch when the laser was pumped with 3.6ps pulse. When the cavity was too short, the lasing pulse was long and the autocorrelation function contained a coherence spike. As the cavity was lengthened, the coherence spike disappeared, the pulse duration narrowed and the spectral width increased. After the cavity was lengthened over the position where the laser generated highest output power, the pulse width started to broaden again, the spectral width increased further and the coherence spike reappeared. For high positive mismatch, the spectra narrowed again. We found that the minimum autocorrelation width of 19ps occurred at a cavity length about 10μm shorter than the length that produced the maximum spectral width of 7.5nm (FWHM). The wavelength of the peak of the lasing spectra

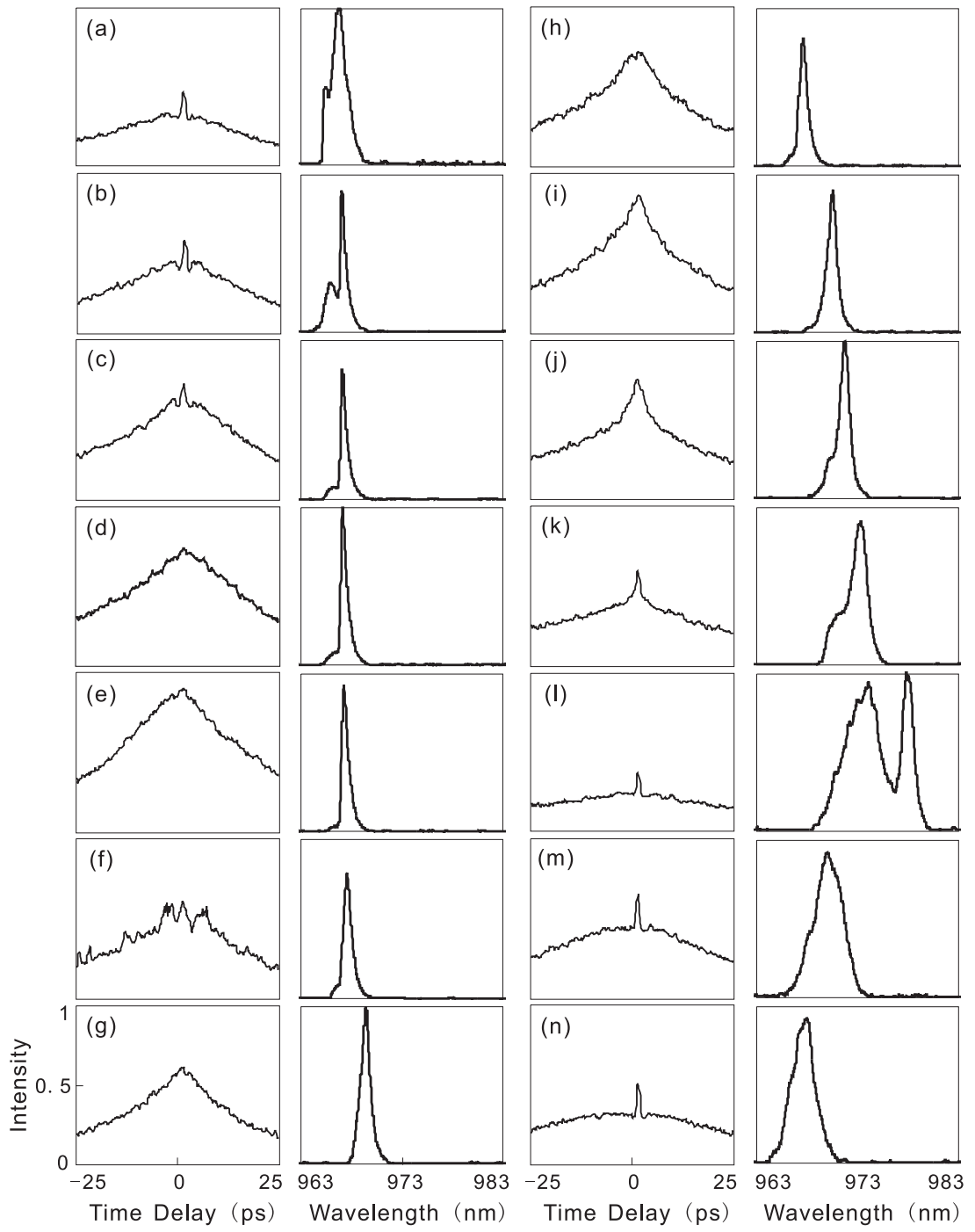


Figure 4.10. Series of autocorrelation traces of pulses (left hand side) and spectrum (right hand side) obtained from VECSEL without BRF at different settings of the cavity length (ps-pumping): (a) $-95\mu\text{m}$; (b) $-83\mu\text{m}$; (c) $-60\mu\text{m}$; (d) $-55\mu\text{m}$; (e) $-40\mu\text{m}$; (f) $-32\mu\text{m}$; (g) $-18\mu\text{m}$; (h) $-15\mu\text{m}$; (i) $-5\mu\text{m}$; (j) $0\mu\text{m}$; (k) $+5\mu\text{m}$; (l) $+10\mu\text{m}$; (m) $+15\mu\text{m}$; (n) $+25\mu\text{m}$.

of the VECSEL first shifted from 966nm to 974nm, and it moved back to 966nm after the spectral broadening stopped. The laser pulse duration was in the range of

10-40ps (assuming a hyperbolic secant profile), again far from the inherent limit imposed by the spectral width of the VECSEL. The temporal profile of the laser intensity was monitored by using a fast photodiode. Noisy intensity profile was found when the cavity length was detuned to around a cavity length of 50 μ m shorter than the optimum length. And this noise on intensity appeared to be a much more pronounced periodic modulation when the cavity was set in the range of -80 μ m to -400 μ m relative to optimum length where the mode locking operation had stopped. Figure 4.11 demonstrates the whole evolvement. The modulation frequency linearly increased with cavity mismatch length, from ~5MHz to ~10MHz, until the lasing stopped. It represented the repetition frequency difference between master and slave laser.

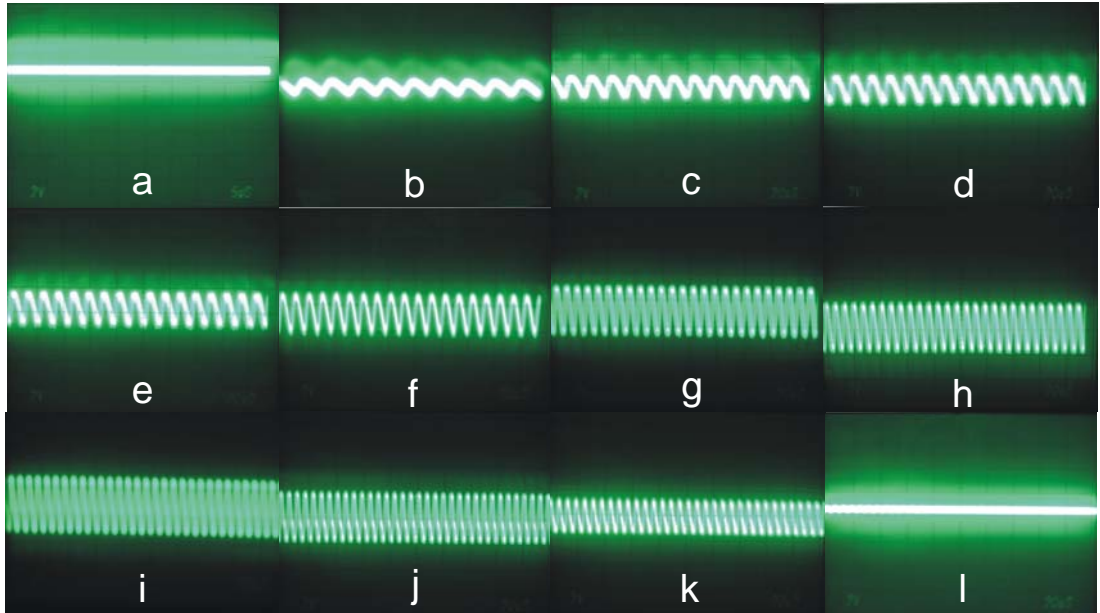


Figure 4. 11. Depth and frequency of the modulation of VECSEL output varied with cavity length mismatch: (a) -50 μ m; (b) -60 μ m; (c) -80 μ m; (d) -100 μ m; (e) -140 μ m; (f) -160 μ m; (g) -180 μ m; (h) -240 μ m; (i) -280 μ m; (j) -320 μ m; (k) -360 μ m; (l) -400 μ m.

As already described in section 4.3.1 for the case of fs pulse pumping, in order to improve the quality of laser pulses as well as controlling the spectrum and polarization, a 1mm thick single plate BRF was again put into the laser cavity at Brewster's angle. The resulting autocorrelation traces and the spectra are shown in Fig. 4.12. Similar observations were obtained, such as the widths of the spectra are

reduced, modulated laser output at short cavity and the phenomenon of multiple pulses is much clearer and more strongly pronounced. The change of the laser power as a function of cavity length mismatch is shown in Fig. 4.13. The tuning range for laser power reducing to half of the maximum was measured to be $208\mu\text{m}$. The maximum output power was reduced to be around 10mW and the laser slope efficiency at optimal cavity length was about 3%.

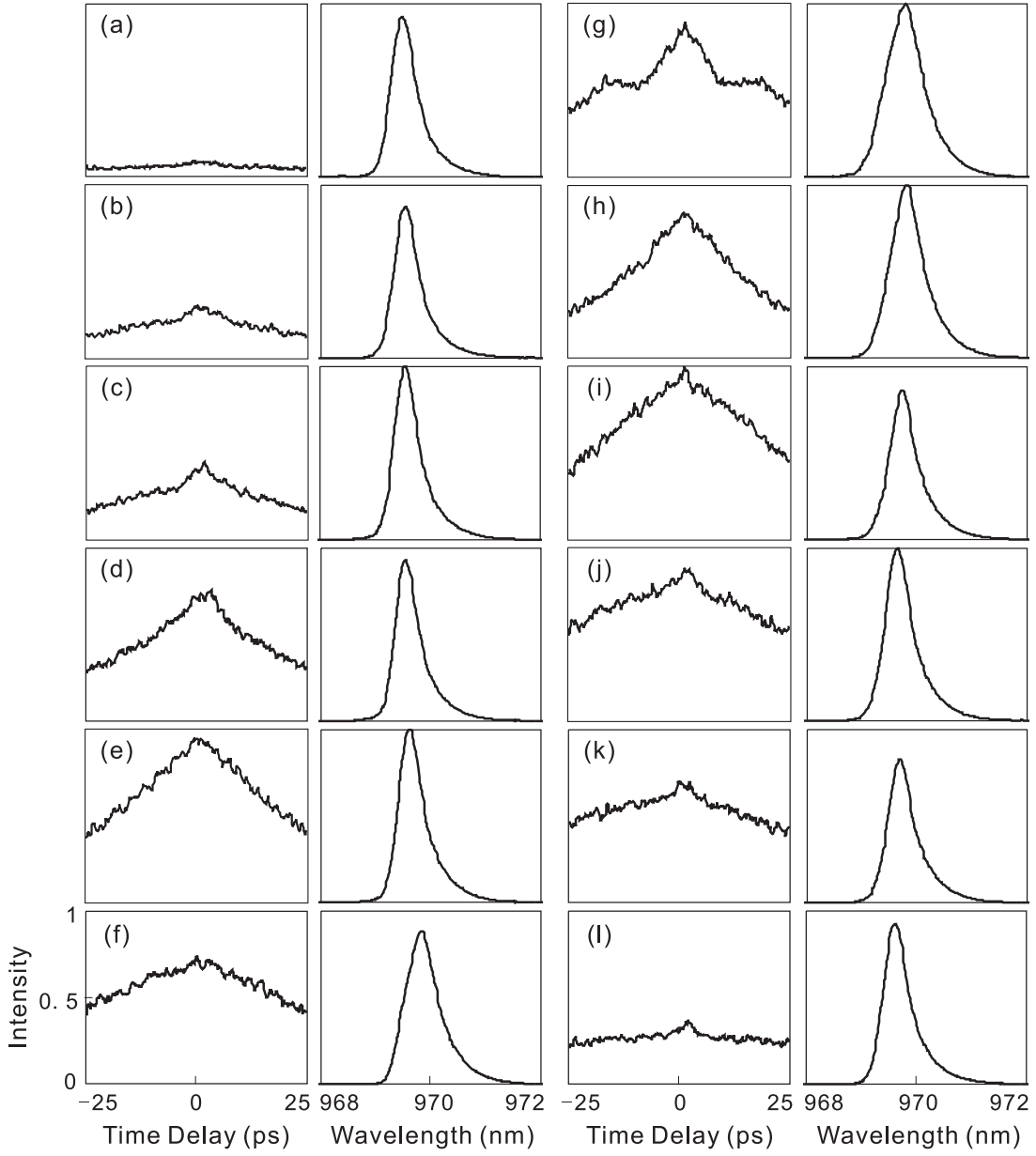


Figure 4.12. Series of autocorrelation traces of pulses (left hand side) and spectrum (right hand side) obtained from VECSEL with BRF at different settings of the cavity length (ps-pumping): (a) $-100\mu\text{m}$; (b) $-80\mu\text{m}$; (c) $-60\mu\text{m}$; (d) $-40\mu\text{m}$; (e) $-20\mu\text{m}$; (f) $-10\mu\text{m}$; (g) $0\mu\text{m}$; (h) $+10\mu\text{m}$; (i) $+20\mu\text{m}$; (j) $+40\mu\text{m}$; (k) $+50\mu\text{m}$; (l) $+80\mu\text{m}$.

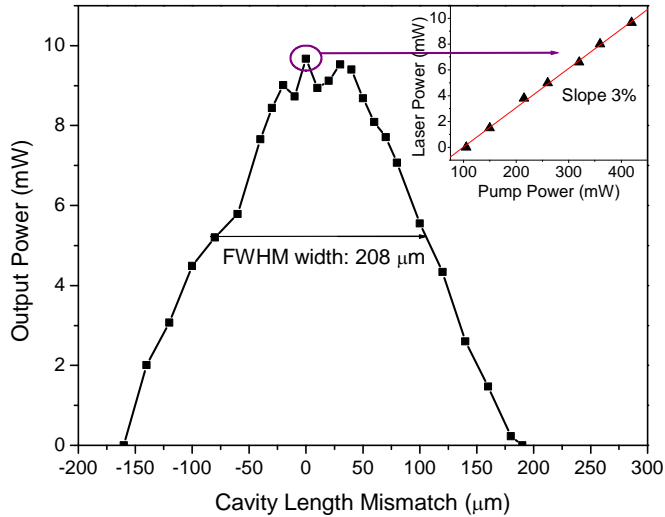


Fig. 4.13. Laser average output power as a function of cavity length mismatch (ps pumping with BRF); the inset shows the laser power increases pump power at optimal cavity length.

4.4.2.2. Extra-cavity compression of pulses

Using the same grating pair as described above, the pulses could be compressed in a region below the point of maximal spectral width. Fig. 4.14 shows the result where the FWHM pulse duration before compression was measured to be about 25-30ps with a 6.2nm FWHM spectral bandwidth. By setting the distance of two gratings to be approximately 28cm apart, we obtained a compressed pulse with FWHM of the autocorrelation trace of 286fs corresponding to a duration of 185fs, if a hyperbolic secant profile is assumed. The average power after grating pair was measured to be about 4.5mW and hence it corresponds to a peak power of 300W. The time-bandwidth product in this case was calculated to be 0.36, indicating that the initial up-chirp of the laser pulses was well compensated. The dispersion from the grating-pair was calculated to be about -15ps^2 (by using Eq. 3.3).

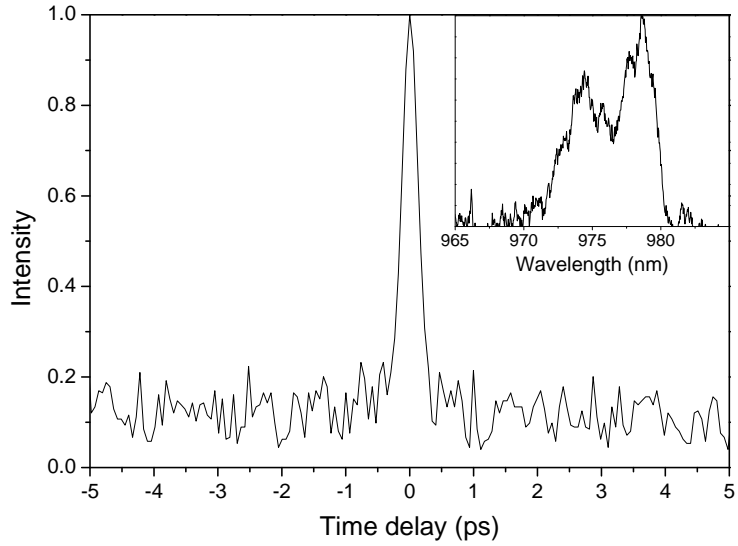


Fig. 4.14. Autocorrelation and spectrum of the compressed pulse (ps-pumping); The pulse width is 185fs assuming a hyperbolic secant profile. (The detuning length was about +5~10 μ m)

4.5. Discussion

4.5.1. Possibilities of intra-cavity dispersion compensation

4.5.1.1. Gires-Tournois Interferometer

Although successful extra-cavity pulse compression has already been obtained by using either grating pair or an optical fiber delay line, we are still very interested in a more compact ultra-short pulse generator achieving by intra-cavity pulse compression. A GTI, described in last chapter, was considered for this purpose. The theoretical calculation was firstly conducted before putting the GTI directly into the cavity, as we would like to know what the maximum group delay dispersion (GDD) it can provide. The GTI we considered here was taken from the commercial Ti:Sapphire laser (Spectra-Physics Tsunami 3960 S3S). The reflectivity of the front and back surface is 4% and 100%, respectively. The air-gap between two mirror

surfaces can be tuned around $80\mu\text{m}$. Hence by using Eq. 3.7 we could calculate the GDD at different wavelengths. Figure 4.15 shows the results. The calculated maximum dispersion (absolute value) is 0.14ps^2 which is two orders of magnitude less than the dispersion of the laser pulse ($+20\text{ps}^2$).

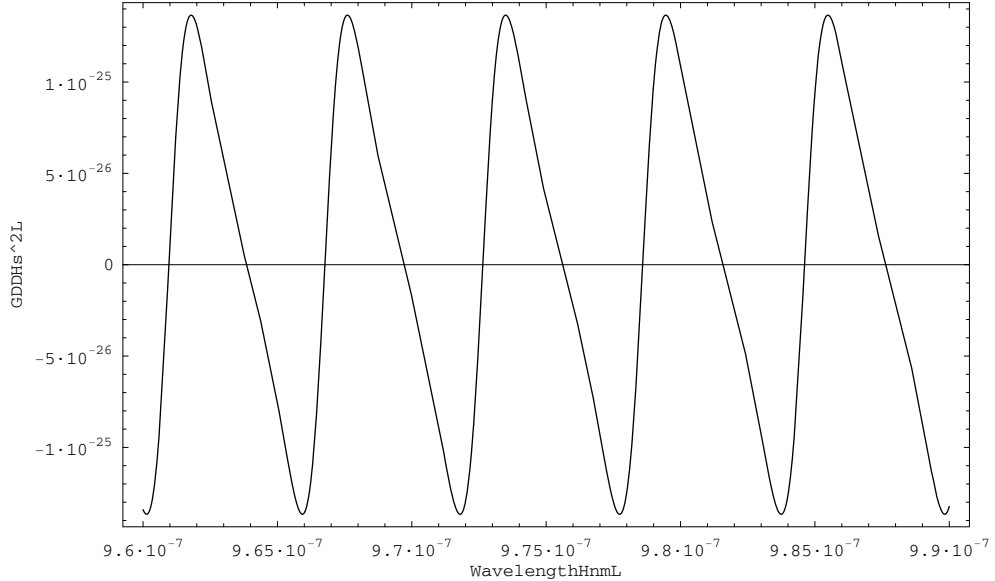


Fig. 4.15, Group delay dispersion induced from Gires-Tournois interferometer as a function of wavelength, the reflectivity of the first surface is 4% and the thickness of the air gap is $80\mu\text{m}$.

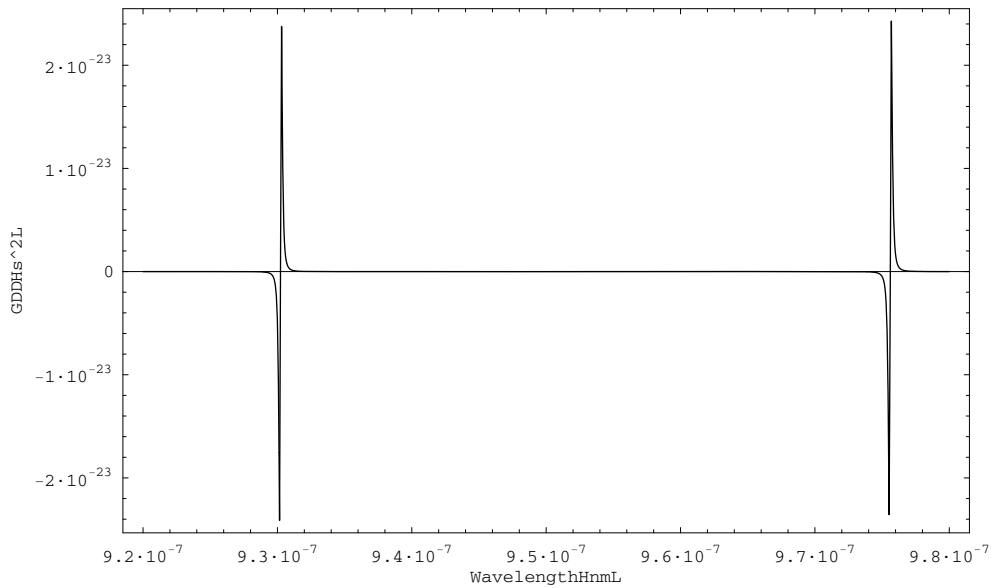


Fig. 4.16, Group delay dispersion induced from Gires-Tournois interferometer as a function of wavelength, the reflectivity of the first surface is 97% and the thickness of the air gap is $10\mu\text{m}$.

In order to compensate such strong dispersion, a new GTI design was carried out. Since the bandwidth of a GTI should be much larger than that of a laser pulse ($\sim 7\text{nm}$), assumed 50nm in this case, the air-gap should be around $10\mu\text{m}$. The required reflectivity of the first surface should be larger than 97%. However, this high finesse design is very impractical as: Firstly, the air-gap is too thin which is very difficult for alignment. Secondly, the half width of the transmission maxima, shown in Fig.4.16, is narrower than 0.5nm which is much less than the 7nm bandwidth of the laser radiation. The higher the reflectivity of the first surface the narrower the transmission maxima. From the above discussion, we can conclude that GTI is not a suitable element for intra-cavity dispersion management in our case.

4.5.1.2. Prism Pair

As described in Chapter Two, prism pair is a widely used optical element for intra-cavity dispersion compensation due to its low insertion loss and the ability for allowing a continuous tuning of GVD from negative to positive dispersion. Figure 4.17 shows the operation principle of a prism pair inside a laser cavity.

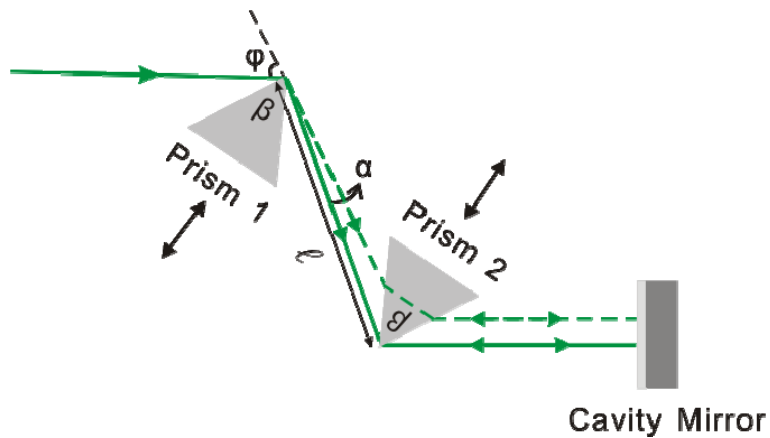


Fig. 4.17. Schematic setup of two prism sequence with adjustable GVD

Calculations based on Eq. 3.5 have been done here to see whether prism pair is suitable or not in order to compensate the massive dispersion ($10\text{-}40\text{ps}^2$) of the synchronously mode-locked VECSEL demonstrated above. The separation between

two prisms can be estimated by following equation

$$\ell = \left(\ln'' - \Phi''(\omega_l) \cdot \frac{2\pi c^2}{\lambda_l^3} \right) / 4(n')^2, \quad (4.1)$$

Therefore, the required distance should be at least 1.3km so as to provide enough negative dispersion ($\sim -10\text{ps}^2$) for compensating the strong dispersed laser pulse at 975nm. Such a long distance is not practical for the experimental implementation. And hence prism pair is not a suitable element for the intra-cavity dispersion management for the synchronously pumped VECSELs.

4.5.2. Differences between ps and fs pumping

It appears from our experiments that the key parameters for the operation around the optimum detuning condition as the bandwidth of the laser spectrum, the width of the autocorrelation function and the feasibility and fidelity of compression actually do not depend very much on the pulse duration of the input pulse. This is probably related to the fact that the optical pumping excites carriers in the barriers and that it takes about 20ps [10] until the carriers relaxed down into the QW and provide gain at the lasing wavelength. The potential relevance of this delay was apparently not recognized by previous studies (e.g. [20]) of synchronously mode-locked VCSELs

4.5.3. Form of autocorrelation functions and drift instability

Although details might be different for the different configurations, there are some common tendencies in the behaviour of the laser, if the cavity length is tuned through zero. If the cavity is much shorter than the matched length, the autocorrelation traces are rather broad and the spectra are rather narrow. Increasing the length, the pulses narrow and the spectra become broader and asymmetric (with a shift to higher wavelength). Around the matched condition, the autocorrelation function displays satellite peaks indicating multiple pulsing (see below). If the cavity length is

increased further, the pulses broaden again, but a strong coherence spike is present in the autocorrelation function (especially in the case without a BRF). This indicates the presence of a sub structure within the pulses. For even higher lengths, the spectra narrow again.

For an interpretation of these features we recall some results on synchronously pumped dye and color center lasers [11-14]. These lasers can exhibit stable pulsing in the sense that the pulses (or pulse sequences) are the same for each round-trip only in a very limited - though finite - interval of cavity mistuning. This is related to the fact that a timing offset due to a cavity length mismatch would accumulate over several round-trips and result in a temporal walk-off of the circulating pulses versus the optimal gain condition imposed by the time window of the synchronous pumping. A finite mismatch can be tolerated, since the gain gradients (in time) pull or push the circulating pulse versus the optimal condition. The width of this ‘locking’ region is given by the so-called cavity filtering time τ_f , either imposed by the spectral width of the gain medium or by frequency-selective intra-cavity filtering elements [11, 14]. For the longer cavity, if the cavity mismatch is too large, a drift instability occurs and perturbations wander across the pulses from round-trip to round-trip [11, 14]. The existence of these sub structures is witnessed by the coherent spike in the autocorrelation function for the long cavities. A cross correlation between subsequent pulses was done for color center lasers [14] and reveals that actually the maximum cross correlation is obtained for a nonzero delay confirming the existence of a drift. We can expect a similar feature in our laser.

The cavity filtering time τ_f is defined as

$$\tau_f = 1/4\pi\sqrt{d^2T(v)/dv^2} \quad (4.2)$$

where $T(v)$ is the filter power transmission as a function of the optical frequency v . It can be expressed by

$$T(v) = \frac{(1-R)^2}{(1-R)^2 + 4R\sin^2(2\pi vnl\cos(\theta)/c)} \quad (4.3)$$

where R is the reflectivity at each interface of the filter, v is the laser frequency, n is the refractive index of the filter, l is the filter thickness and the θ is the angle formed between the filter and the intra-cavity laser beam. Hence by using Eq. 4.2 and Eq. 4.3, the filtering time for the laser operating at around 970nm and with a 1mm Brewster angled BRF was estimated to be 12fs. The different filtering time in the case without (limited by the bandwidth of the gain spectrum) and with BRF (estimated to be 12fs corresponding to a length mismatch of $1.8\mu\text{m}$) explain also why the features observed are less sensitive to the cavity length tuning, if the BRF is used.

Towards the low-cavity length limit, the regime with good mode-locking is limited by the fact that the circulating pulse has to arrive after the pump pulse established threshold inversion in order to achieve efficient amplification. Below this point, lasing might occur in the form of a broad pulse determined in width by the build-up time of the gain and gain saturation [22]. This is probably the origin of the broad pulses we observed for very short cavity lengths.

4.5.4. Multiple pulsing

The appearance of multiple pulses can be explained by the rather long time it takes to build up the gain after the pump pulse because the carriers need to relax into the QWs. Hence, the effective pumping time is rather long and in that limit multiple pulsing is a well known phenomenon in dye and color center lasers [11, 14-15]. They can be explained by the fact that the gain is not completely saturated by the main pulse and due to the ongoing pumping the threshold might be crossed a second time (or even repeatedly). The fact that the timing distance to the main pulse decreases for increasing cavity length (shown in Fig. 4.6) indicates that the circulating pulse arrives before the conditions for best gain is amplified and leaves enough inversion for a satellite pulse. Interestingly, this change of timing is different from most observations in dye and color center lasers, where the separation between pulses increases for increasing cavity mismatch [14, 22]. Close inspection of the data shows

that there is actually a very small interval of detuning, where multiple pulsing reappears, after it seems to have ceased (just before the pulses broaden again, detuning length of $+1\mu\text{m}$ in Fig. 4.4, detuning length of $3.57\mu\text{m}$ in Fig. 4.6). Whether this second regime is related to the observations in dye lasers cannot be decided on the basis of our data because it is too small to be analysed in a systematic way.

A detailed theoretical analysis of the multiple pulsing and its possible relationship to the changes observed in the spectrum is beyond the scope of this work. The interplay of different effects is probably more involved than in dye and color center lasers, because in semiconductor lasers, the frequency of peak gain and the group refractive index will depend strongly on the carrier density. In addition, both are highly dynamic, which is also demonstrated by the chirp of the pulses measured. We will turn to a discussion of the latter in the following.

4.5.5. Analysis of pulse chirp

As already mentioned, the chirp of the pulses was estimated to be on the order of 10 ps^2 in the regime where we can assume that chirp is the dominant pulse distortion (obviously high-order phase aberration will be present and also the envelope of the spectrum is not well behaved). The dispersion caused by the DBR structure and material dispersion for the related semiconductor materials in the transparent region and other intracavity elements like mirrors are all on the order of 10^{-4}ps^2 which should be negligible [16-18, 20]. So the dominant cause of pulse chirping is phase modulation in the laser amplifier [19, 20].

There are two main contributions: one is the phase modulation originating from the pulsed optical pumping, the other SPM due to gain saturation [20]. The resulting changes in carrier density cause a change in refractive index due to the strong phase-amplitude coupling in semiconductors. This carrier-induced index change, responsible for SPM, is often accounted for through the linewidth enhancement factor α [20, 21]. A simplified equation has been developed to describe the two

contributions on the frequency sweep of the output VECSEL pulse [20]:

$$\Delta\omega_{\text{out}} = \frac{\alpha P_p(\tau + \Delta\tau)}{2\gamma E_{psat}} \cdot \left\{ 1 - \exp\left[\gamma G(\tau) - b(N_{p0} - N_0)L\right] \right\} - \frac{\alpha P_{in}(\tau)}{2E_{sat}} \left\{ \exp[G(\tau)] - 1 \right\} \quad (4.4)$$

where P_p is the pump power, P_{in} is the power for input laser pulse, $\Delta\tau$ is the timing mismatch between pump pulse and laser pulse, α is the linewidth enhancement factor, E_{psat} and E_{sat} represent the saturation energy for pump pulse and laser pulse respectively; γ is the ratio between the differential gain coefficients at pump frequency ω_p and laser frequency ω_l ; N_{p0} and N_0 are the transparent carrier densities at pump frequency ω_p and laser frequency ω_l ; L is the effective length of gain medium. The first part of the right side of the equation describes the effect of the pulsed optical pumping to the frequency sweep of the laser pulse; while the second part illustrates how the SPM induced by gain saturation affects the pulse chirp.

A quantitative analysis for the sign and amount of the dispersion based on a GaAs VECSEL system has been given by Jiang et al. [20]. However, the equations of motion of the field and the carriers in the presence of the cavity are not solved consistently, but it is only calculated, what chirp a laser pulse with a Gaussian shape with a fixed width will acquire, if traversing the gain medium pumped by a pulse with a Gaussian shape.

Gain saturation alone is shown to result in an up-chirp of the laser pulse, whereas the optical pumping leads to a down-chirping. The relative strength of the two effects depends on the ratio between the duration of the pump pulse (better the build-up time of the gain, because there might be a delay before the carriers relaxed down into the QW) and the duration of the laser pulse. If the duration of the pump pulse is about the same or shorter than the laser pulse, then the chirp due to optical pumping is larger than the chirp due to gain saturation and the pulses are down-chirped. If the laser pulse is considerably shorter than the pump pulse, gain saturation dominates the chirp and the pulse becomes up-chirped. We explain the preference for up-chirp in our experiment with the fact that the build-up time for the gain is rather long due to

the fact that we pump the barriers. Hence gain saturation is the prevailing chirp mechanism. In accordance with that a higher chirp was found for the case with BRF where the laser pulse before compression was shorter than without BRF.

The observation of a down-chirp in a small regime where the mode-locking process becomes unstable might be due to the fact that the pulses there are longer and hence optical pumping is dominating the chirp. We stress that the results of [20] also imply that in general no simple chirp can be expected and that the chirp depends on cavity tuning. This explains qualitatively the smallness of the regions where efficient compression could be achieved. We note that the chirp of 10ps^2 measured is of the order of magnitude to be expected from the considerations in [20].

Our results qualitatively agree with findings in synchronously pumped long-wavelength VECSEL (emission in the $1.5\mu\text{m}$ region) for long pump pulses (about 150ps in [7]; about 8ps in [6] showing however long tails and satellite pulses thus increasing the effective pulse length [20]). These authors find also up-chirping, if the cavity length is tuned to the position of maximal spectral bandwidth. They demonstrate also that the pulse is down-chirped for other cavity tuning conditions [6] though it is not clear under which conditions this change takes place. In [7], it is conjectured that the pulses are down-chirped, if the cavity tuning is adjusted to yield the shortest pulses (without compression), because it could not be compressed with a grating pair. However, the possibility of a compression in a fiber was not demonstrated. We consider our experiments to be clarifying in that respect. The absolute pulse length obtained were considerably longer ($>700\text{fs}$ even after compression) than in the present work. However, a detailed comparison is probably not possible because of the different material systems.

Nice work was also done on GaAs systems operating in the 880nm spectral region. Here, down-chirped pulses, which could be compressed down to 320fs, were obtained for pump pulses with a duration of 5ps. However, the compression involved a significant amount of spectral filtering also and the autocorrelation has a significant

pedestal. The sign of the chirp is in agreement with the expectation from [20] for short pump pulses, though it can be suspected that the gain build-up time is actually higher also in their case. Possibly, they were investigating the regime slightly beyond the ‘switching point’ of chirp where we also found down-chirping. The configurations are similar in the sense that there were no bandwidth-limiting elements and that they also observed a coherent spike in the autocorrelation function before compression. We could not reproduce the result in [23], where pulses - though low power (about 6mW average power) with a duration of about 200fs were obtained directly from an oscillator in the 890 nm region. This result was related to the filtering effects of resonant periodic gain [23]. Possibly our structure is less effective because we have only half the number of period.

4.6. Conclusion

A synchronously mode-locked 980nm VECSEL has been described. Detailed studies of the laser characteristics as a function of pump duration and cavity tuning were performed showing the potentials as well as the limitations of the synchronous pumping approach for mode-locking. The output pulses had duration of 10-40ps for ps as well as for fs pumping. This indicates strong chirping due to the optical pumping-induced carrier generation and due to SPM by gain saturation. These processes were analyzed in some detail. Chirp compensation was effectively achieved by using either a grating-pair or a fiber. Nearly transform-limited pulses with duration of a few hundred femtoseconds with peak power ranging from 300W to 1.3kW were obtained. Thus it appears that synchronous pumping might be useful to provide ultrashort pulse sources at repetition rates of about 100MHz in spectral regions which cannot be accessed directly by other sources (mainly the Ti:Sapphire laser). Our results demonstrate that it is not necessarily beneficial to use very short pump pulses, but that the performance will stay about the same till the 10ps range. We mention that it appears to be interesting to reconsider this issue in conjunction

with the recently introduced technique of in-well pumping [24-25], where the dynamics of the gain build-up is expected to be faster. Obviously, more efficient techniques for external pulse compression or intracavity dispersion would be helpful in order to overcome the massive chirping present in these devices.

4.7. Reference

- [1]. E. Bertseva, A. A. Kachanov, A. Campargue, "Intracavity laser absorption spectroscopy of N₂O with a vertical external cavity surface emitting laser," *Chemical Physics Letters*, Vol 351, No. 1-2, pp. 18-26, 2002.
- [2]. U. Keller, K. J. Weingarten, F. X. Kartner, D. Kopf, B. Braun, I.D. Jung, R. Fluck, C. Honninger, N. Matuschek and Juerg Aus der Au, "Semiconductor Saturable Absorber Mirrors (SESAM's) for Femtosecond to Nanosecond Pulse Generation in Solid-State Lasers," *IEEE Journal of Selected Topics in Quantum Electronics*, Vol. 2, No. 3, pp. 435-453, 1996.
- [3]. S. Hoogland, A. Garnache, I. Sagnes, J. S. Roberts and A. C. Tropper, "10 GHz train of sub-500-fs optical soliton pulses from a surface-emitting semiconductor laser," *IEEE Photonics Technology Letters*, Vol. 17, No. 2, pp. 267-269, 2005.
- [4]. M. A. Holm, P. Cusumano, D. Burns, A. I. Ferguson and M. D. Dawson, "Mode-locked operation of a diode-pumped, external-cavity GaAs/AlGaAs surface emitting laser," in *Proceedings of IEEE Conference on Lasers and Electro-Optics* (Institute of Electrical and Electronics Engineers, New York, 1999), pp. 153-154.
- [5]. W. B. Jiang, R. Mirin and J. E. Bowers, "Mode-Locked GaAs vertical cavity surface emitting lasers," *Applied Physics Letters*, Vol. 60, No. 6, pp. 677-679, 1992.
- [6]. W. B. Jiang, S. R. Friberg, H. Iwamura and Y. Yamamoto, "High powers and subpicosecond pulses from an external-cavity surfaceemitting InGaAs/InP multiple quantum well laser," *Applied Physics Letters*, Vol. 58, No. 8, pp. 807-809, 1991.
- [7]. W. H. Xiang, S. R. Friberg, K. Watanabe, S. Machida, W. B. Jiang, H. Iwamura and Y. Yamamoto, "Femtosecond external-cavity surface-emitting InGaAs/InP multiple-quantum-well laser," *Optics Letters*, Vol. 16, No. 18, pp. 1394-1396, 1991.
- [8]. D. B. McDonald, J. L. Rossel and G. R. Fleming, "Temporal and spectral studies of a synchronously pumped dye laser: Detailed interpretation of autocorrelation measurements," *IEEE Journal of Quantum Electronics*, Vol. 17, No. 6, pp. 1134-1138, 1981.
- [9]. E. B. Treacy, "Optical pulse compression with diffraction gratings," *IEEE Journal of Quantum Electronics*, Vol. 5, No. 9, pp. 454-458, 1969.

- [10]. A. R. Zakharian, J. Hader, J. V. Moloney, S. W. Koch, P. Brick, S. Lutgen, “Experimental and theoretical analysis of optically pumped semiconductor disk lasers,” *Applied Physics Letters*, Vol. 83, No. 7, pp. 1313-1315, 2003.
- [11]. F. Minami and K. Era, “Cavity detuning effects in the synchronously mode-locked CW dye laser,” *Optics Communications*, Vol. 56, No. 1, pp. 46-50, 1985.
- [12]. W. Forysiak and J. V. Moloney, “Dynamics of synchronously pumped mode-locked color-center lasers,” *Physical Review A*, Vol. 45, No. 5, pp. 3275-3288, 1992.
- [13]. W. Forysiak and J. V. Moloney, “Mode-locking dynamics of synchronously pumped color-center lasers,” *Physical Review A*, Vol. 45, No. 11, pp. 8110-8120 1992.
- [14]. U. Morgner and F. Mitschke, “Drift instabilities in the pulses from cw mode-locked lasers,” *Physical Review E*, Vol. 58, No. 1, pp. 187-192, 1998.
- [15]. L. W. Casperson, “Coherence effects in synchronously pumped mode-locked dye lasers,” *Journal of Applied Physics*, Vol. 54, No. 5, pp. 2198-220, 1983.
- [16]. S. de Silvestri, P. Laporta and O. Svelto, “The role of cavity dispersion in CW mode-locked lasers,” *IEEE Journal of Quantum Electronics*, Vol. 20, No. 5, pp. 533-539, 1984.
- [17]. P. Laporta and V. Magni, “Dispersive effects in the reflection of femtosecond optical pulses from broadband dielectric mirrors,” *Applied Optics*, Vol. 24, No. 13, pp. 2014-2020, 1985.
- [18]. N. Pikhtin and A. D. Yas’kov, “Dispersion of the refractive index of semiconductors with diamond and zinc-blende structures,” *Sov. Phys-Semiconductor*, Vol. 12, pp. 622-626, 1978.
- [19]. G. P. Agrawal and N. A. Olsson, “Self-phase modulation and spectral broadening of optical pulses in semiconductor laser amplifiers,” *IEEE Journal of Quantum Electronics*, Vol. 25, No. 11, pp. 2297-2306, 1989.
- [20]. W. B. Jiang, D. J. Derickson, and J. E. Bowers, “Analysis of Laser Pulse Chirping in Mode-Locked Vertical-Cavity Surface-Emitting Lasers,” *IEEE Journal of Quantum Electronics*, Vol. 29, No. 5, pp. 1309-1318, 1993.
- [21]. C. H. Henry, “Theory of the linewidth of semiconductor lasers,” *IEEE Journal of Quantum Electronics*, Vol. 18, No. 2, pp. 259-264, 1982.

- [22]. C. P. Ausschnitt, R. K. Jain and J. P. Heritage, "Cavity Length Detuning Characteristics of the Synchronously Mode-locked CW Dye Laser," IEEE Journal of Quantum Electronics, Vol. 15, No. 9, pp. 912-917, 1979.
- [23]. W. B. Jiang, M. Shimizu, R. P. Mirin, T. E. Reynolds, and J. E. Bowers, "Femtosecond periodic gain vertical-cavity lasers," IEEE Photonics Technology Letters, Vol. 5, No. 1, pp. 23-25, 1993.
- [24]. M. Schmid, S. Benchabane, F. Torabi-Goudarzi, R. Abram, A. I. Ferguson, and E. Riis, "Optical in-well pumping of a vertical-external-cavity surface-emitting laser," Applied Physics Letters, Vol. 84, No. 24, pp. 4860-4862, 2004.
- [25]. W. Zhang, T. Ackemann, S. McGinily, M. Schmid, E. Riis, A. I. Ferguson, "Operation of an optical in-well-pumped vertical-external-cavity surface-emitting laser," Applied Optics, Vol. 45, No. 29, 7729-7735, 2006.

Chapter Five

Single frequency operation of a compact 980nm VECSEL

5.1. Introduction

In this chapter, the single frequency operation based on a compact 980nm VECSEL is demonstrated. A novel technique is applied to stabilize an intra-cavity etalon which was used for single-mode selection in the VECSEL cavity. Active stabilization of the laser was achieved by locking the laser to a reference cavity.

5.2. Overview

Single frequency operation acts in the opposite way to mode-locking. For laser mode locking, the more oscillating modes exist the narrower the generated pulse will be. However singe frequency operation requires only one longitudinal mode. This can be achieved by introducing wavelength dependent loss. Normally a combination of a Brewster angled birefringent filter (BRF) and an intra-cavity etalon is used. The BRF, also called Lyot filter [1], consists of one or several birefringent plates sandwiched by two polarizers. It introduces birefringence which leads to wavelength-dependent polarization rotation and thus wavelength-dependent transmission loss at the polarizers. The rotation of the BRF can provide a coarse tuning of the laser. The etalon works as a spectral filter which forms a Fabry-Perot cavity inside the laser and confines the laser spectrum to a series of transmission bands. By carefully choosing

the thickness and the reflectivity of the etalon, efficient spectral filtering can be achieved and single frequency operation is thus obtained. In addition to these two intra-cavity elements, active stabilization is required to lock the laser longitudinal mode to a specific wavelength. This is due to the fact that any small vibration of the cavity mirrors or rotation of the etalon would be enough to cause mode jumping. The stabilization of the laser enables a stable performance of the laser with narrow spectral linewidth.

Till now, many efforts have already been made to generate narrow linewidth output from different types of semiconductor lasers in different spectral regions. A monolithic 1550-nm single-mode AlInGaAs-InP multiple quantum-well distributed feedback laser was reported by RT Sahara et al. in 2002. They obtained laser linewidth as narrow as 50kHz [2]. A linewidth of less than 20kHz was achieved in single-frequency VCSELs by A Ouvrard [3]. External cavity grating tuned diode lasers generated an output with less than 50kHz line-widths [4]. In 1995 Loh WH demonstrated a novel cavity configuration for single frequency operation of the semiconductor laser. By using a 3m erbium doped fiber as the external cavity, longitudinal mode-hopping is suppressed and 1kHz linewidth was obtained [5]. However, the output power of these reported laser sources is typically a few milliwatts. The fast development of VECSELs solves the problem of low output power while keeping narrow laser line-width. M. Holm demonstrated first single frequency operation of an 870nm GaAs/AlGaAs based VECSEL with a laser relative linewidth of 3kHz and the maximum output power of 42mW [6]. In this chapter, I will describe a single frequency operation of an InGaAs/AlGaAs based VECSEL operating around 970nm. This device produced up to 260mW of output power with about 9nm tuning range. Both the intra-cavity birefringent etalon [7-8] and the laser cavity length were actively stabilized to give a root-mean-square (rms) line-width of 45kHz. The use of resonant periodic gain (RPG) effectively eliminates spatial-hole burning and makes these structures ideal for single-frequency operation by using

only simple standing-wave cavity configurations. Therefore, single frequency VECSELs are expected to have wide applications in laser spectroscopy and nonlinear optics due to their wavelength versatility, simplicity of design and stable narrow line-width operation.

5.3. Theory

5.3.1. Spatial hole burning (SHB)

According to the laser theory developed by Schawlow and Townes [9], the output of crystalline solid state lasers should be extremely monochromatic since their lineshapes are homogeneous broadened and thus the lasers have fast spectral cross relaxation rate which would lead to single mode laser output. However, early solid-state lasers were found to be multimode. The origin for multimode oscillation of the solid-state lasers was discovered to be slow spatial cross-relaxation or SHB by Tang, et. al. [10].

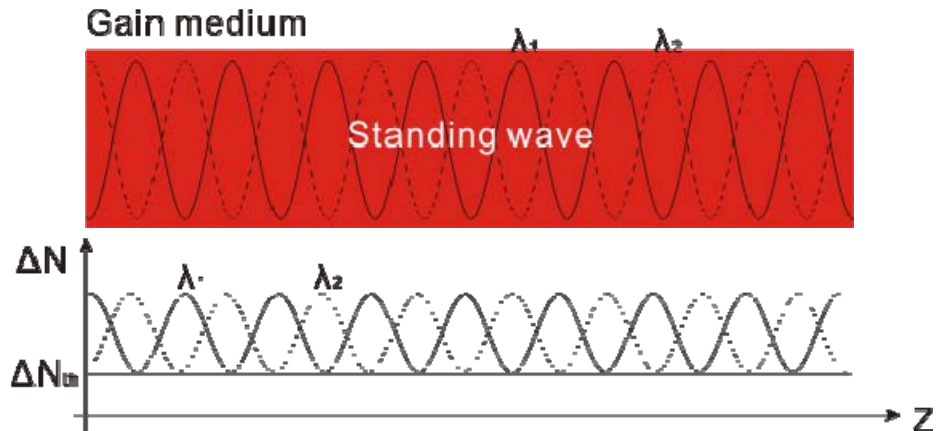


Fig. 5.1. Spatial intensity distribution for two standing wave fields with different wavelengths λ_1 and λ_2 .

In a linear laser resonator, the electrical field of the lasing mode will interfere with itself to form an optical standing wave. The intensity of the standing wave varies sinusoidally along the axis of the active medium and resonator, as shown in the upper graph of Fig. 5.1. Since the stimulated emission is only generated at anti-nodes of the

standing wave, hence the population inversion ΔN at anti-nodes starts to be saturated and finally pinned to the threshold ΔN_{th} value when the stationary oscillation of the mode is reached. At mean time the stimulated emission at nodes equals to zero and the population inversion is not affected and keeps increasing. Tang et al. [10] has shown that the rate of spatial diffusion of the population inversion is very slow. This would result a spatial modulation on the laser gain (population inversion) along the axis Z. When the unsaturated gain accumulates to reach a certain level, another mode will be excited to oscillate. Thus the standing wave field of the second mode has its anti-nodes overlap with the undepleted gain or the nodes of the first standing wave field, as shown in the bottom graph of Fig. 5.1. The second field has a shift of $\lambda/4$ against to the first field. Same argument can be applied for the stimulation of the third mode with shift of $\lambda/3$, fourth mode and so on. The increase of the number of the modes will not stop until the gain is uniformly saturated.

Although theoretically SHB can be minimized by making an active medium sufficiently short and placing it close to one cavity mirror (for standing wave cavity), in practice the extremely short length gain medium has to be paid at the price of using a very high absorption coefficient material. Most solid state laser materials do not have such a high absorption coefficient, and therefore this idea can not be applied generally. Another idea is to eliminate the standing wave field of the laser cavity. This can be achieved by creating a travelling wave field by building a unidirectional ring cavity such that the field will sweep the gain of the crystal and hence avoid SHB. This unidirectional design is now widely employed for obtaining single frequency operation. However comparing with standing wave cavity, unidirectional design requires optical diode to block one direction of propagation, which thereby adds more complexity on the cavity design and alignment. Also it is very sensitive to the birefringence of the optical elements inside the cavity, such as gain medium.

The appearance of VECSELs has successfully solved those problems and completely eliminated the effect of SHB. Both linear cavity and ring cavity can be used for

single frequency operation. This is due to the incorporation of the resonant periodical gain structure into the active medium, which has been introduced in chapter two (section 2.2.2). By placing the active material only where it is most needed (anti-nodes of the standing wave of the mode), there is no gain at the nodes and therefore modes can not build up between the anti-nodes of the standing wave.

5.3.2. Birefringent etalon

The details on how birefringent etalon works and its application to active stabilization for single-mode operation have been reported by Gardner, et al [7]. Here I will briefly introduce this element and the stabilization technique based on it.

The reflection coefficient $A_r(\delta, A)$ for an electric field incident on a solid etalon is given by the expression [11],

$$A_r = \frac{(1 - e^{i\delta}) \cdot \sqrt{R}}{1 - R \cdot e^{i\delta}} A_i \quad (5.1)$$

where R is the intensity reflection coefficient and $\delta = \frac{4\pi n l \cos(\theta)}{\lambda}$ is the phase retardation for a roundtrip of the light of wavelength λ in the etalon with thickness d and refractive index n , which is tilted at an angle θ to the incident beam. The reflection coefficient has a period of $c/(2n \cdot d \cdot \cos(\theta))$.

The etalon described in this chapter is made of birefringent material. Therefore, the two refractive indices n_1 and n_2 corresponding to the two principal axes of the material will lead to two different values δ_1 and δ_2 for the phase delay. According to Eq.5.1 this will result in different reflectivities for the two polarizations. If the phase difference $\delta_1 - \delta_2$ is π modulo of 2π the reflection for one polarization will be maximum while it will be minimum for the other. The etalon is needed to be slightly tilted to form a small angle, γ , between the laser polarization and one of the optic axes as shown in Fig.5.2. The majority of the light (intensity of this component

proportional to α^2) is polarized along this axis while a component proportional to β^2 has orthogonal polarization ($\alpha^2 + \beta^2 = 1$). The incident electric field can be resolved in its two components along these two axes

$$\vec{E}(t) = (\alpha \cdot E_0 \cdot \exp(i\omega t), \beta \cdot E_0 \cdot \exp(i\omega t)) \quad (5.2)$$

where E_0 is the amplitude and ω the optical frequency. The reflected electric field is then

$$\vec{E}_r(t, \delta_1, \delta_2, R) = (\alpha \cdot E_0 \cdot A_r(\delta_1, R) \cdot \exp(i\omega t), \beta \cdot E_0 \cdot A_r(\delta_2, R) \cdot \exp(i\omega t)) \quad (5.3)$$

At transmission resonance for the 1-component ($\delta_1=0$ modulo 2π) the reflected light is then only linearly polarized along the 2-axis. At either side of the resonant point it is elliptically polarized with opposite helicity.

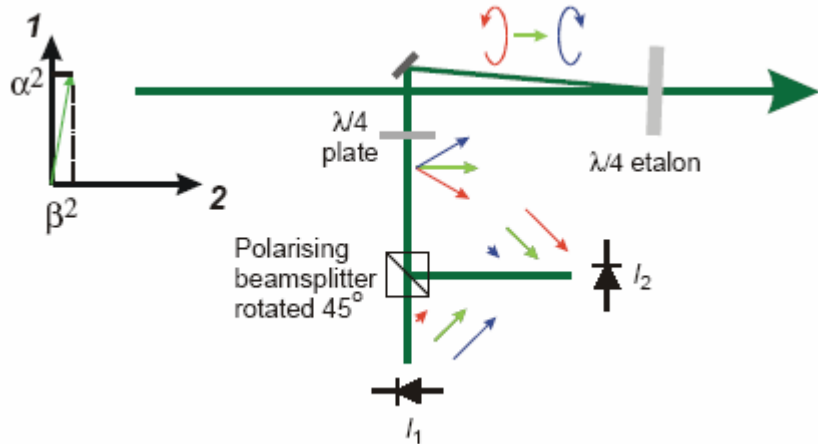


Fig. 5.2. Schematic setup for the operation of the birefringent etalon demonstrated in an extra-cavity. After [6]

This polarization can be analyzed by the combination of a quarter-wave plate and a polarizing beam-splitter, as shown in Fig. 5.2. The quarter-wave plate is aligned with the axes of the birefringent etalon so as to get linearly polarized light after the wave-plate. The direction of the polarization is changing with the difference between the frequency of the mode and the etalon transmission maxima. The varying linear polarization can now be analyzed with polarizing beam-splitter set at an angle of 45° relative to the axes of the quarter wave-plate. The two output electric fields from

the beam-splitter are:

$$E_1(t, \delta_1, \delta_2, R) = \frac{\sqrt{2}}{2} (\alpha \cdot E_0 \cdot A_r(\delta_1, R) \cdot \exp(i\omega t) + i \cdot \beta \cdot E_0 \cdot A_r(\delta_2, R) \cdot \exp(i\omega t)) \quad (5.4)$$

$$E_2(t, \delta_1, \delta_2, R) = \frac{\sqrt{2}}{2} (\alpha \cdot E_0 \cdot A_r(\delta_1, R) \cdot \exp(i\omega t) - i \cdot \beta \cdot E_0 \cdot A_r(\delta_2, R) \cdot \exp(i\omega t)) \quad (5.5)$$

The intensities $I_1(\delta_1, \delta_2, R)$ and $I_2(\delta_1, \delta_2, R)$ of the two beams after the polarization beam splitter are detected by two identical photodetectors. From the qualitative arguments regarding the polarizations above, these two intensities would give an asymmetric imbalance around the minimum loss point of the etalon. This can be described quantitatively by

$$S(\delta_1, \delta_2, R) = \frac{I_2(\delta_1, \delta_2, R) - I_1(\delta_1, \delta_2, R)}{I_2(\delta_1, \delta_2, R) + I_1(\delta_1, \delta_2, R)} = \frac{2 \cdot \alpha \cdot \beta \cdot \text{Im}[A_r(\delta_1, R) \cdot A_r^*(\delta_2, R)]}{\alpha^2 \cdot |A_r(\delta_1, R)|^2 + \beta^2 \cdot |A_r(\delta_2, R)|^2} \quad (5.6)$$

Hence the resulting function S changes with the relative phase difference $\delta_1 - \delta_2$ between two components and it will cross zero at the etalon resonance. This provides an ideal discriminant for an electronic stabilization circuit. Furthermore this technique is insensitive to laser intensity fluctuations and demonstrates a good tolerance for wavelength drifting, thus it is relatively easy to compute electronically either by using analogue circuits or digitally.

5.3.2. Confocal Fabry-Perot Interferometer

Confocal Fabry-Perot Interferometers (FPIs) are widely used as high-resolution spectrum analyzers for detecting the mode structure and the linewidths of lasers. As shown in Fig 5. 3, a typical confocal FPI consists of two spherical mirrors with equal radius of curvature (r). The distance between two mirrors is set to be $d=r$. Hence if we neglect the spherical aberration, any rays entering the interferometer and propagating parallel with the axis of the interferometer would pass through the focal point F . And they will return to the entrance point after four passages through the confocal FPI.

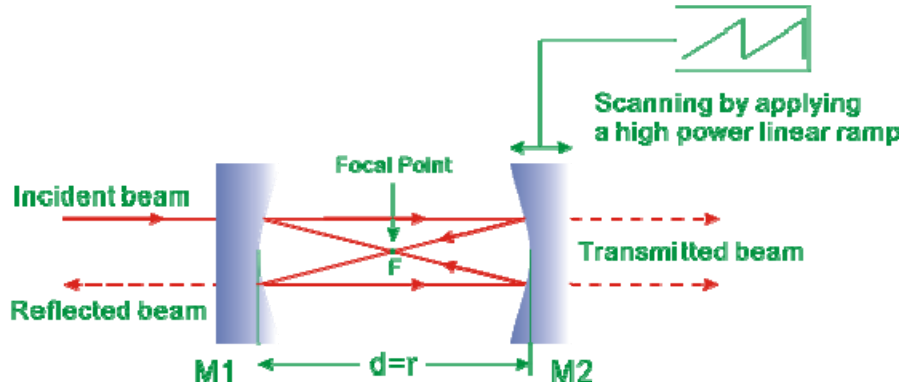


Fig. 5.3, the schematic of the confocal Fabry-Perot interferometer

However in reality, the entering ray is not parallel to the axis but with a small inclination θ ($\theta \ll 1$) and the spherical aberration can not be neglected. They would result in deviation of the propagation directions of the rays. Therefore rays with different distances l from the axis will not go through focal point F but will intersect the axis at different positions depending on l and the entering angle θ . In this case, rays would not return to their starting positions after four passages through the interferometer since the deviation will accumulate in the successive passages. The transmitted intensity function for near-confocal FPI with $l \ll d$ can be described as [12]

$$I(l, \lambda) = \frac{I_0 T^2}{(1-R)^2 + 4R \sin^2[(\pi/\lambda) \cdot \Delta s]} \quad (5.7)$$

$$\Delta s = 4d + l^4 / r^3 \quad (5.8)$$

where Δs is the optical path difference between two successive rays passing through the same point, λ is the laser wavelength, R is the reflectivity of each of the two mirrors, $T=1-R-A$ is the transmission of each of the two mirrors and I_0 is the intensity for incident ray. The intensity function has maxima for $\Delta s=m\lambda$ (m is positive integer). Therefore, the free spectral range (FSR) $\Delta\nu$ of the interferometer can be expressed

as $\delta\nu = \frac{c}{4d + l^4 / r^3}$, where c is the speed of the light. The spectral resolution of a

confocal FPI is determined by the full halfwidth of the transmission peaks, which can be described as

$$\Delta\nu = \delta\nu/F^* \quad (5.9)$$

where F^* is the finesse of the interferometer, it is related to the mirror reflectivity,

$$F^* = \frac{\pi\sqrt{R}}{1-R} \quad (5.10)$$

Only when the separation of two frequency peaks is larger than the full halfwidth of the transmission peaks $\Delta\nu$, two frequencies can be resolved by the interferometer. In this chapter, confocal FPI has been used to obtain the spectrum of a single frequency laser. Laser longitudinal modes can be fully resolved by scanning one of the mirrors so as to vary the distance d ($d > \lambda/4$). It should be noted that the FSR of the laser cavity should be smaller than that of a confocal FPI.

5.4. Single frequency operation

5.4.1. Experimental Setup

The 2mm x 2mm VECSEL sample was taken from the same semiconductor wafer described in Chapter Three for synchronous mode locking operation. The wafer has a mirror-on-substrate structure. In this structure, a highly reflecting Bragg mirror is first grown. It consists of 30 quarter-wave pairs of AlAs and GaAs layers. Grown on top of the Bragg mirror is gain region consisting of typically 14 $In_{0.16}GaAs$ quantum wells with thickness of 8nm each. On either side of the quantum wells is an appropriate GaAsP strain compensating layer. A confinement window layer $Al_{0.3}GaAs$ is then grown on top of the gain region and finally an $In_{0.48}GaP$ cap layer is added to prevent oxidation of the material. This semiconductor sample was bonded with a 700 μm thick diamond heat spreader with parallel surfaces and with a small wedge. The surface away from the gain medium is anti-reflection (AR) coated with a

reflectivity of less than 10^{-4} at the lasing wavelength. The use of wedged diamond and AR coating is to eliminate the etalon effects from the diamond. The sample and diamond as whole then is mounted on a water-cooled copper block. The compact laser cavity configuration is shown in Fig. 5.4.

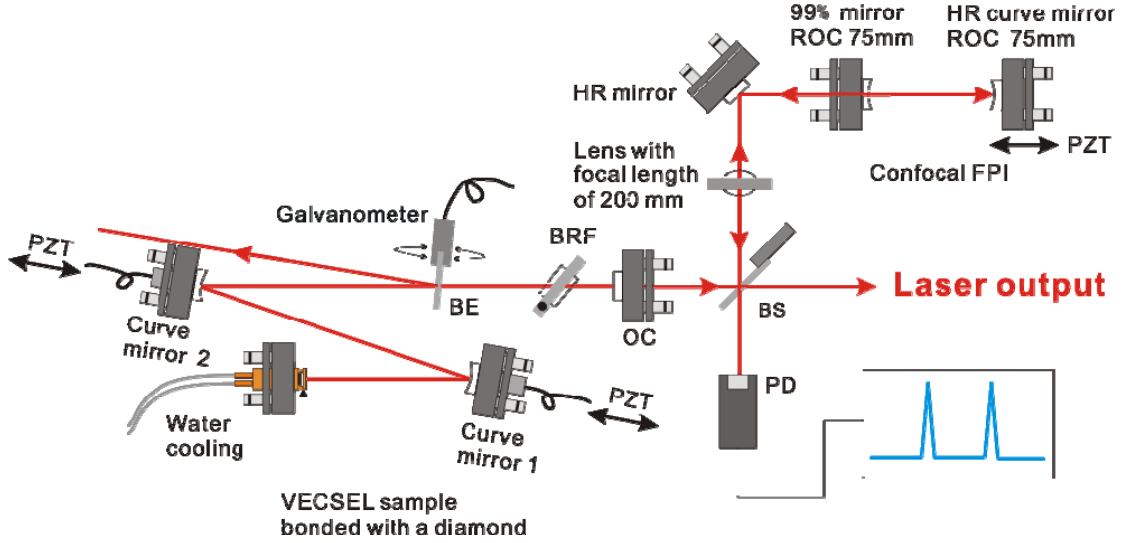


Fig.5.4. Schematic of the experimental setup for single mode operation of VECSEL; OC: output coupler, BRF: birefringent filter, BE: birefringent etalon, HR: high reflection FPI: Fabry-Perot Interferometer, BS: beam splitter, PZT: piezo-electric transducer, PD: photodiode.

The pump laser is a fiber coupled laser diode operating at the wavelength of 808nm. It delivers up to 15W out of a 200 μm diameter 0.22NA fiber. The pump light is focused with a high-NA lens system to an approximately 138 μm diameter spot. The pump incident angle is set to be around 45°. The total cavity is folded by two highly reflecting (<99.8% in the range 950-1050nm) curve mirrors (mirror 1 with radius of curvature of 25mm; mirror 2 with radius of curvature of 100mm) in order to obtain a compact cavity. Both of them are mounted on a piezo-electric transducer to enable fast electronic control of the cavity length. The output coupler is flat and its reflectivity is 98%. The distances for L1, L2 and L3 are about 24mm, 67mm and 100mm respectively. The total cavity length is 191mm which corresponds to a cavity FSR of 785.3MHz. The single frequency operation can be obtained by inserting a combination of a birefringent etalon made of crystalline quartz and a 2mm thick

single plate BRF. Only use of the BRF results a narrow laser spectrum with bandwidth of $\sim 0.2\text{nm}$. Additional insertion of an etalon would narrow the spectrum further and single mode will be selected. The birefringent etalon was designed to have a reflectivity of 25% and a $17\lambda/4$ plate at the laser wavelength of 975nm. The FSR of the etalon is 200GHz. Since the etalon is used to select suitable cavity mode by tilting the angle between intra-cavity laser beam and the etalon surface, it is thus very important to enable an accurate electronic control of the tilt angle. This can be obtained by mounting the etalon on a galvanometer (Model 6210, Cambridge Technology Inc.) with a horizontal rotation axis. The galvanometer is driven by a commercial precision mirror positioning system (Series 678XX Cambridge Technology Inc.) and rotates at a rate of $0.39^\circ/\text{V}$. The maximum rotation angle of the galvanometer is set to be 4° . As shown in Fig.6.2, the etalon is “walked off” slightly in the horizontal direction so as to pick a small part of laser beam for the purposes of diagnostic and active stabilization, which will be discussed in the section 5.5. The laser beam from the output coupler is focused into a confocal FPI using a lens with a focal length of 200mm. There are three purposes for the use of an interferometer: (a) to monitor the laser longitudinal modes; (b) to stabilize the laser by locking the laser cavity to the interferometer; (c) to enable fine tuning of the laser by scanning the interferometer. The interferometer consists of two curved mirrors with identical radius of curvature which is 75mm. The separation between two mirrors is set to 75mm. This corresponds to a cavity FSR of 1GHz. The input mirror of the interferometer has a reflectivity of 99% in the spectral range of 950-1050nm. The rear mirror with high reflection coating over this range is mounted to a piezo-electric transducer which moves at a rate of $1.5\mu\text{m}/\text{V}$. The finesse of the interferometer is calculated to be better than 150 and the bandpass is 6.5MHz.

5.4.2. Experimental Results

Before the intra-cavity elements were inserted, the laser gave a maximum power of 420mW with horizontal polarization. This power level dropped to be around 260mW when the BRF and etalon were both inserted and are aligned to select single longitudinal mode.

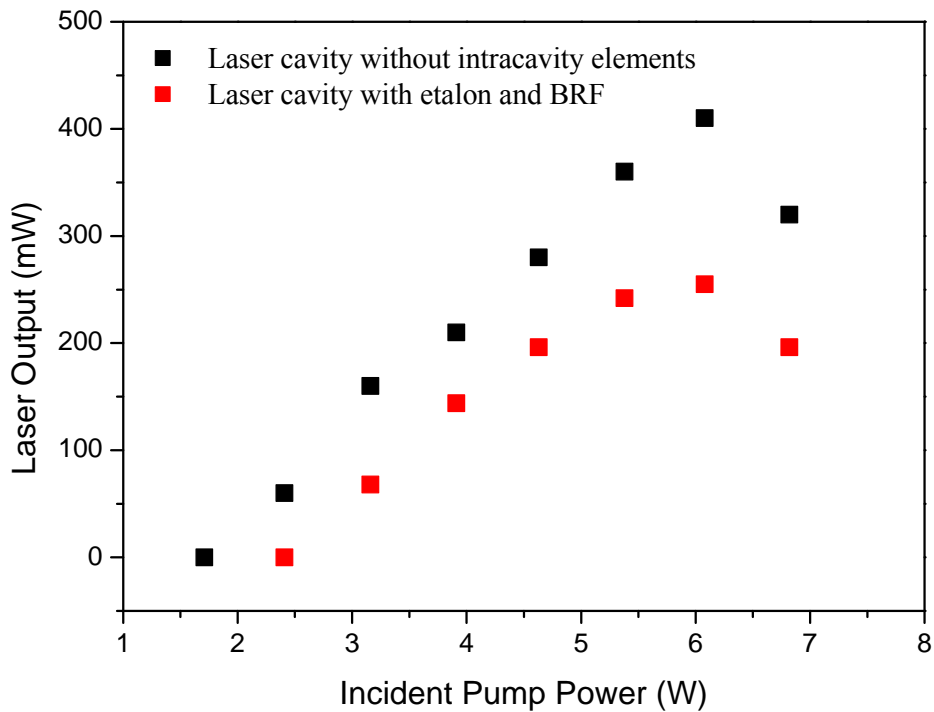


Fig.5.5. Laser power as a function of pump power

Figure 5.5 shows the power transferring curve for the laser with and without intra-cavity elements. Thermal roll over was observed. This is due to the fact that the semiconductor gain region is only cooled by free running water. The increase of pump power would lead to the generation of extra heat in the gain region that could not be evacuated and hence decrease laser efficiency. The heat extraction could be slightly improved by increasing the flow rate of the water. The slope efficiencies for

both cases (without intra-cavity elements and with intra-cavity elements) are measured to be about 10%. After passing through a beam splitter, 25% of the output laser beam was directed into the confocal FPI to monitor the laser spectrum, as shown in Fig. 5.6. Before putting the etalon into the laser cavity (only a BRF in the cavity), the laser was running at multiple longitudinal modes, as shown in Fig. 5.6 (a). However when the etalon was inserted into the laser cavity and aligned properly, only one single longitudinal mode was allowed to oscillate and hence single frequency operation was obtained, as shown in Fig. 5.6 (b).

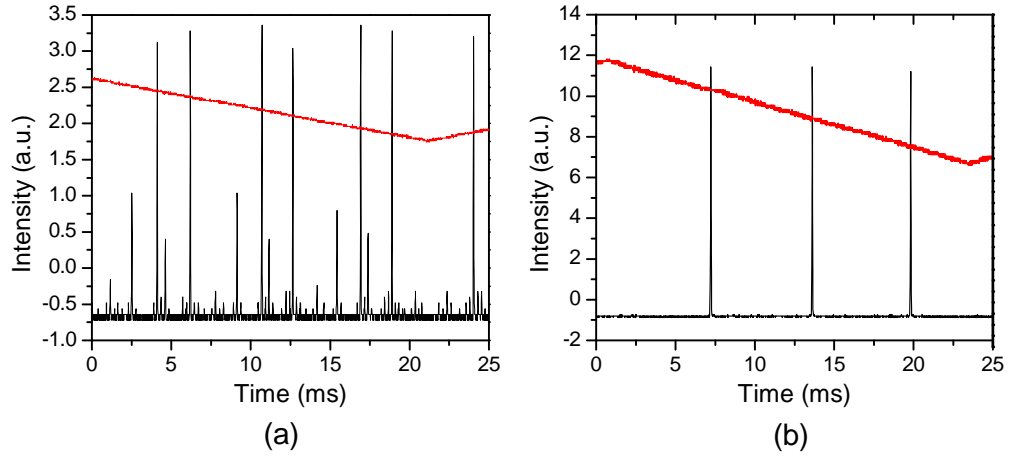


Fig. 5.6. Frequency dependent transmission of a linear Fabry-Perot interferometer for (a) the laser with a BRF but without birefringent etalon, (b) single frequency operation by inserting a BRF and a birefringent etalon

Broad gain bandwidth is one of the advantageous features of the VECSELs, which has already made them an ideal tunable laser source. Measurements of the overall tuning range of the single frequency VECSEL was undertaken using an Optical Spectra Analyzer (HP 86140). This allowed the laser spectral position to be measured to 0.07 nm accuracy. By rotating the BRF filter, a coarse tuning range of 10nm was obtained before the laser power dropped too much as shown in Fig. 5.7. Fine tuning of the laser cavity can be obtained by scanning the confocal FPI. This will be discussed in the following section.

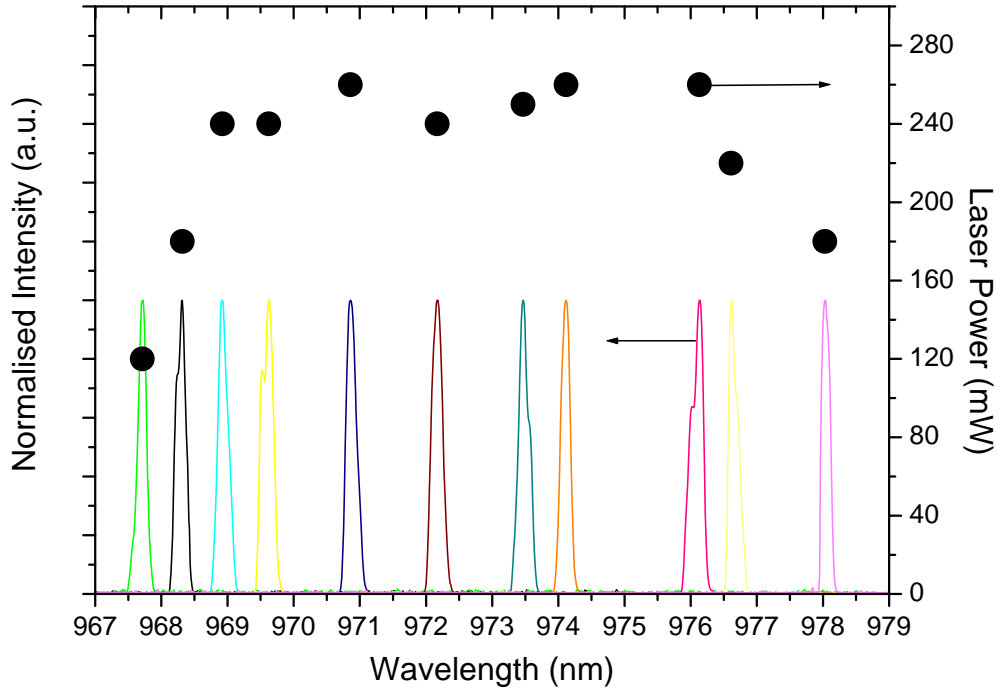


Fig. 5.7. Laser tuning curve: laser power to the right coordinate and the corresponding spectra to the left coordinate

5.5. Active stabilization and tuning

5.5.1. Experiments

As already stated in the section 5.4, single mode operation of the laser can be obtained by inserting a birefringent etalon together with a BRF. However, the oscillating longitudinal mode is not stable and mode hopping is always observed. This could be caused by many reasons, i.e. thermal drifts, acoustical vibration of the cavity mirrors which leads to the change of the cavity length and/or the variation of the etalon angle. Therefore, the stabilization on the cavity length and titling angle of the etalon is extremely important in order to achieve a stable operation of the device.

The frequency shift in titling an etalon from on axis to an angle θ is given by [13]

$$\Delta\nu = v_0\theta^2 / 2 \quad (5.11)$$

So the small change in titling angle θ of size $\delta\theta$ would result in a frequency change given $\delta(\Delta\nu)$ by

$$\delta(\Delta\nu) = v_0 \cdot \theta \cdot \delta\theta \quad (5.12)$$

By using Eq. (5.12) and applying values of $v_0=3*10^{14}$ and $\theta=0.3^\circ$, the rotation of the etalon by an angle of order 10^{-5} degree is sufficient for the laser to jump to the next cavity mode $\delta(\Delta\nu)\sim1\text{GHz}$. Hence the stability requirements are very stringent for the etalon. In this section, we experimentally investigate the technique for active stabilization of the birefringent etalon. Besides the locking of the etalon, the laser cavity length is also needed to be stabilized. This can be implemented by locking the laser to an external reference cavity.

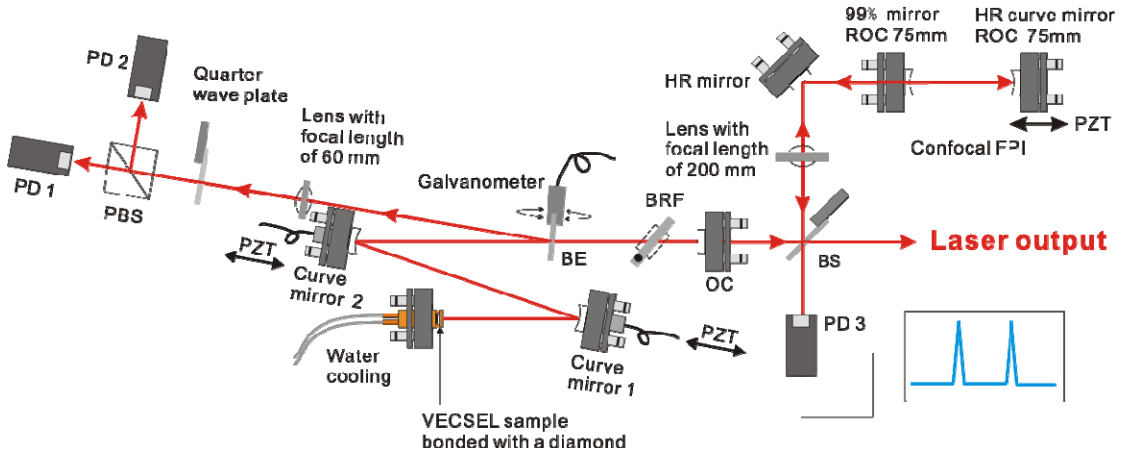


Fig. 5.8. Schematic of the experimental setup for actively stabilized single-mode operation of VECSEL; OC: output coupler, BRF: birefringent filter, BE: birefringent etalon, HR: high reflection FPI: Fabry-Perot Interferometer, BS: beam splitter, PBS: polarization beam splitter, PZT: piezo-electric transducer, PD: photodiode.

Figure 5.8 shows the experimental setup. A polarization analyzing system is built up outside the laser cavity in order to provide a feedback signal to galvanometer to control and lock the etalon electronically. A lens with focal length of 60mm is used to image the lasing spots on the etalon to two identical photodiodes (Hamamatsu S5870). The analyzing quarter-wave plate is aligned with the axes of the birefringent

etalon. And the polarizing beam-splitter is set at an angle of 45° relative to the axes of the analyzing quarter wave-plate. After passing through the quarter wave plate and the polarization beam splitter, the reflected linear polarized beam is split into two beams with identical intensities but perpendicular polarizations along the two axes of the beam splitter. Signals from two photodiodes are then fed into an electronic circuit and an error signal is generated by taking the difference of those two signals. This error signal would be integrated, amplified and finally applied to the galvanometer so as to compensate the slight rotation of the etalon. A closed feedback loop is then formed. When the error signal crosses zero at the etalon resonance the electronics will catch this position and lock the etalon. Before closing the loop, a sinusoidal voltage is applied directly to the galvanometer to scan the etalon around resonance which changes the direction of the laser polarization and hence results the modulated intensity profile of two polarization components. Figure 5.9 shows the two signals and their differencing error signal.

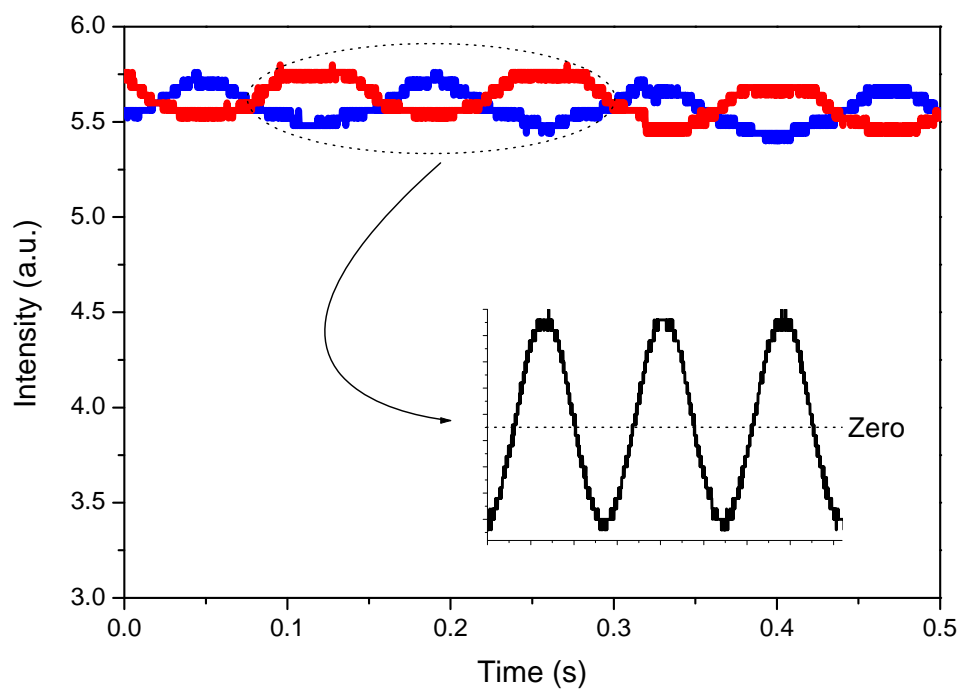


Fig. 5.9. The intensity profiles of the two polarization components of the laser beam detected by the polarization analyzer; inset is the difference of the two signals

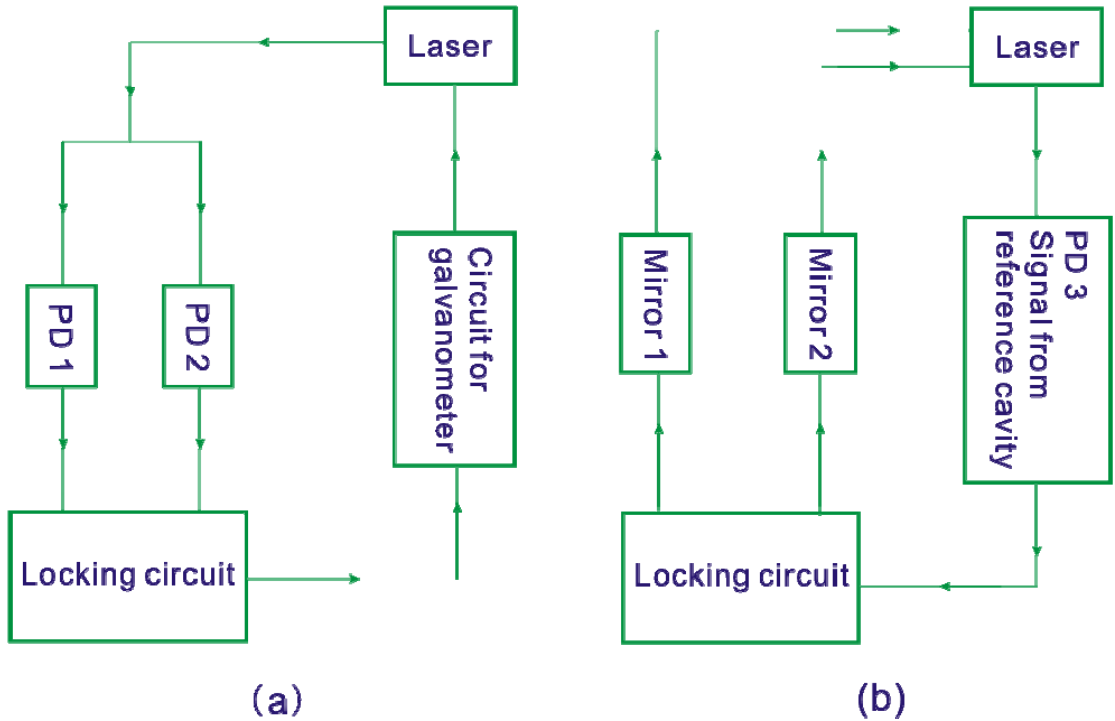


Fig. 5.10. Principle diagram for the active stabilization

Cavity length drifts induced from the acoustical vibration of the cavity mirrors can be stabilized by locking the laser cavity to the confocal FPI. To implement this locking, one requires the electronic control on both mirror 1 and mirror 2. Hence mirror 1 is mounted to a fast piezo-electric transducer with short scanning range. And mirror 2 is mounted to a slow piezo-electric transducer with larger scanning range. The transmission fringes from the reference cavity are detected by a fast photodiode and used as error signal. A negative DC offset is added to the fringes so that the sides of each fringe cross zero voltage level. This error signal is firstly amplified by using a voltage amplifier and then fed into a locking circuit. In the circuit the error signal is integrated and then amplified and drives the two mirrors mounted with the piezo-electric transducers. The fast piezo-mirror will respond quickly so as to determine the moving direction and then the followed larger movement by the slow piezo-mirror is used to compensate the change of cavity length and keep the error

voltage to the zero point (locking point). This feedback loop can thereby electronically stabilize the laser cavity. Figure 5.10 shows the basic operating diagram of the loop. By changing the DC offset different locking points can be determined. The tightest locking point locates at the centre of the fringes where the steepest discriminant of the error signal can be achieved. Steeper discriminant can be obtained by increasing the finesse of the reference cavity. However the steeper the discriminant is the smaller the capture range will be. Hence it is difficult to lock to high finesse cavities using a side-of fringe technique due to the asymmetry in the error signal.

5.5.2. Performance of the active stabilization

Actively stabilized single frequency operation of the VECSEL was achieved by locking both etalon and the laser cavity. Stable performance was obtained over one hour before the locked loop completely loosed. The linewidth of the laser is thus defined as the frequency fluctuations of the oscillating laser mode. Its value can be obtained by measuring the amplitude of the error signal. The voltage amplitude of the error signal can be converted to frequency by calculating the slope around the locking point of the reference fringes. Figure 5.11 shows the transmission fringes of the reference cavity. The full halfwidth of the cavity resonances is 6.5MHz. The slope around the locking point, also known as locking sensitivity, was calculated to be 4.1MHz/V. And the root mean square (RMS) value of the error signal was measured to be 11.2mV. Hence a RMS laser linewidth of 45kHz was attained, as shown in Fig. 5.12. According to the Schawlow-Townes relation [12], the limit of the semiconductor laser linewidth can be predicted. The modified equation can be described as

$$\Delta\nu_L = \frac{\pi h\nu_L \Delta\nu_c^2}{P_L} (1 + \alpha^2) \quad (5.13)$$

where $\Delta\nu_L$ is the limit of the linewidth, ν_L is the laser frequency, P_L is the laser output

power, $\Delta\nu_c$ is the halfwidth of the laser resonator resonance, h is the planck constant and α is the linewidth enhancement factor. Therefore, for a VECSEL operating at 970nm ($\nu_L = 3.09 \times 10^{14} \text{ Hz}$) with output power of 260mW, the resonance halfwidth of 5.1MHz and enhancement factor of 5, the limit of the laser linewidth is thus calculated to be $1.66 \times 10^{-3} \text{ Hz}$, which is far better than the predicted and reported minimum of other types of semiconductor lasers. VECSELs are thus inherently an ideal type of laser sources for single frequency operation.

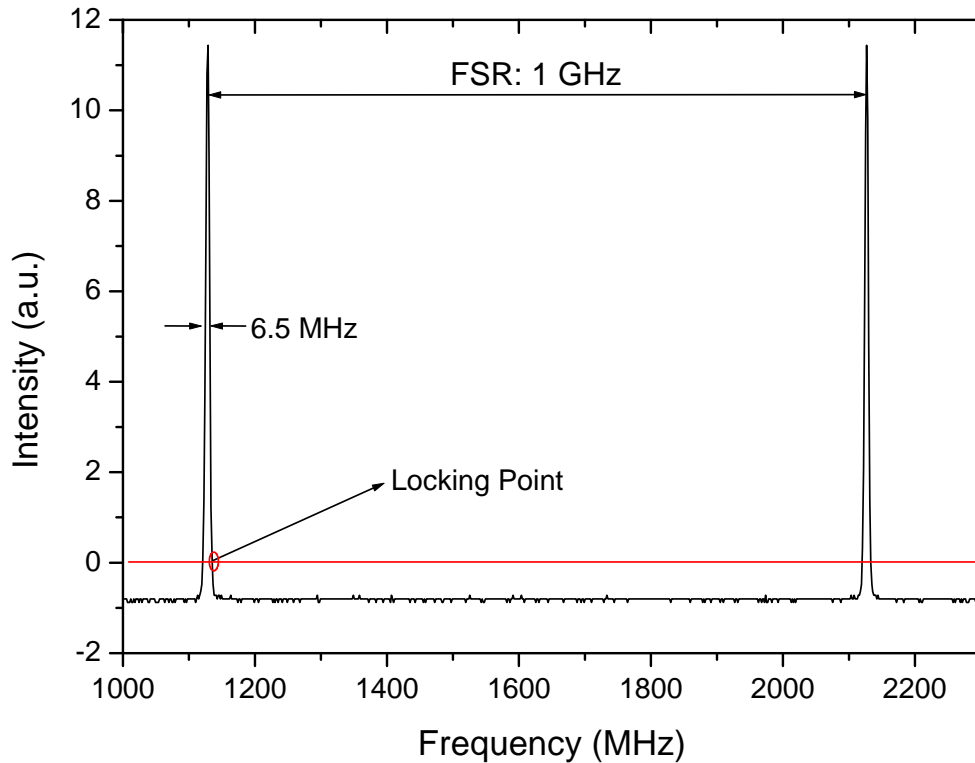


Fig. 5.11. Transmission function of the reference cavity with FSR of 1 GHz.

However the measured value in this experiment is significantly larger than the Schawlow-Townes limit. Hence further improvements of the laser stability are still possible in order to decrease the noise level of the laser and thereby narrow the linewidth. Figure 5.12 also shows the FFT spectrum of the error signal over 40ms. We see that the laser linewidth is limited by the high frequency noise with

fundamental frequency of 18.3 kHz and its harmonics of 36.6kHz, 54.9kHz, and 73.2kHz. By monitoring the FFT of the laser output and the etalon error signal over 40ms when only etalon is locked and the cavity is unlocked, we found that the laser itself is not the source for the high frequency noise, as shown in Fig 5.13. Hence these high frequency noises could possibly come from the power supplies and the piezo-driving circuits which are situated around the laser. A much smaller linewidth could be expected if those electronic noises can be suppressed.

The fine tuning of the stabilized laser was also investigated by applying a slow triangular ramping signal to the reference cavity. The ramp is also fed into the locking circuit to provide a feed forward signal to the laser cavity mirrors. Hence when the reference cavity length or FSR of the reference cavity is changed, the laser cavity mirrors would move accordingly to vary the cavity length. The shift of the cavity mode is thus tracked concurrently and the etalon is then rotated to be resonant to the mode. Experimental implementation shows that a tuning range of up to 4GHz is obtained before the lock is lost.

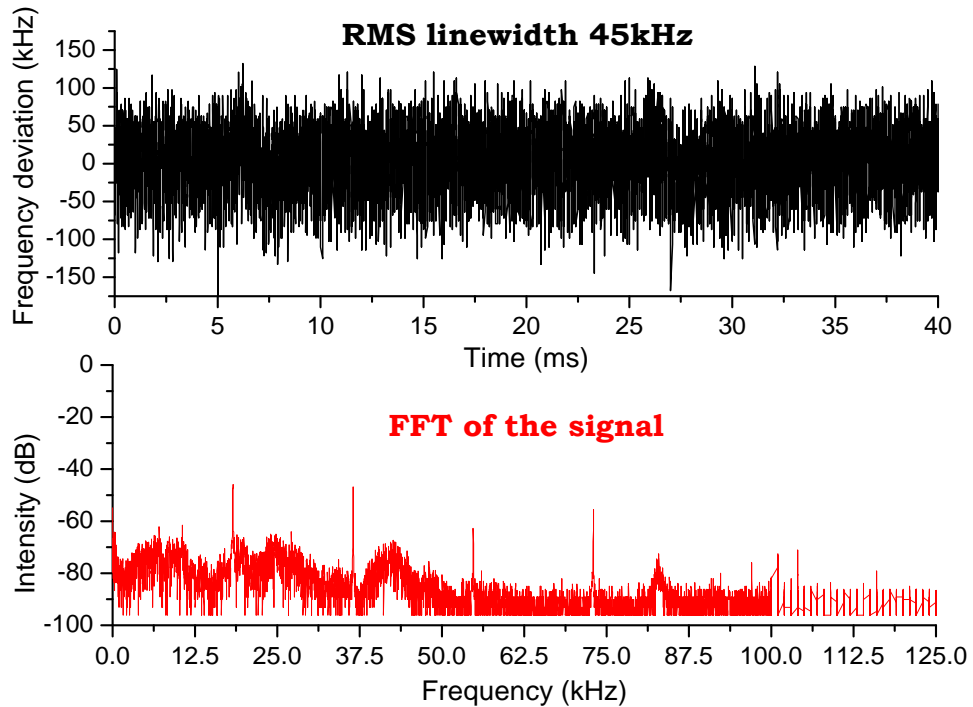


Fig.5.12, error signal and FFT spectrum of an actively locked single frequency VECSEL

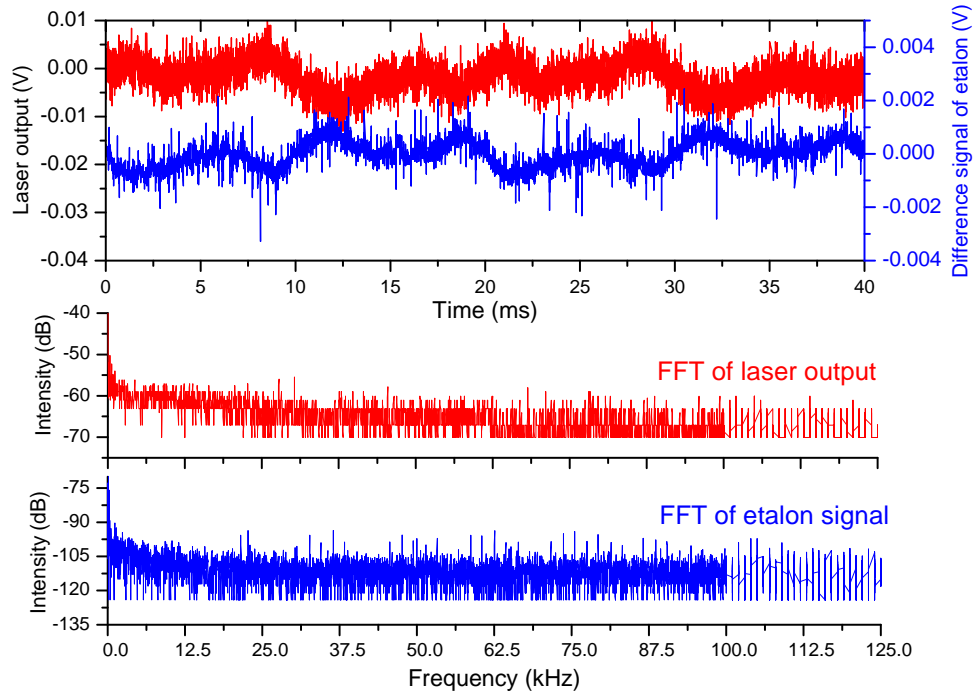


Fig.5.13, laser output and the error signal of the etalon as a function of time and their FFT spectra.

5.6. Conclusions

In conclusion, single frequency operation of a 980 nm VECSEL with compact cavity design has been demonstrated in this chapter. A maximum output power of 260mW was obtained. The laser stabilization was achieved by locking both birefringent etalon and the laser cavity. The relative laser linewidth was measured to be 45kHz. And a fine tuning range of 4GHz has been achieved with a coarse tuning range of 9nm. Further improvements such as suppression of electronic noise by using better circuits can be implemented to push the laser linewidth toward the Schawlow-Townes limit.

5.7. Reference

- [1]. B. Lyot, "Optical apparatus with wide field using interference of polarized light", C. R. Acad. Sci. (Paris) Vol. 197, pp. 1593, 1933
- [2]. R. T. Sahara, R. A. Salvatore, H. Lu, "Single contact monolithically integrated DFB laser amplifier," IEEE Photonics Technology Letters, Vol. 14, No. 7, pp. 899-901, 2002.
- [3]. A. Ouvrard, A. Garnache, L. Cerutti, F. Genty, and D. Romanini, "Single-frequency tunable Sb-based VCSELs emitting at 2.3 μ m," IEEE Photonics Technology Letters, Vol. 17, No. 10, pp. 2020-2022, 2005.
- [4]. P. J. S. Heim, Z. F. Fan, S. H. Cho, K. Nam, M. Dagenais, F. G. Johnson, R. Leavitt, "Single-angled-facet laser diode for widely tunable external cavity semiconductor lasers with high spectral purity," Electronics Letters, Vol. 33, No. 16, pp. 1387-1389, 1997.
- [5]. W. H. Loh, R. I. Laming, N. Zervas, M. C. Farries, and U. Koren, "Single frequency erbium fiber external cavity semiconductor laser," Applied Physics Letters, Vol. 66, No. 25, pp. 3422-3424, 1995.
- [6]. M. A. Holm, D. Burns, A. I. Ferguson, M. D. Dawson, "Actively stabilized single-frequency vertical-external-cavity AlGaAs laser" IEEE Photonics Technology Letters, Vol. 11, No. 12, pp. 1551-1553, 1999.
- [7]. K. S. Gardner, R. H. Abram, and E. Riis, "A birefringent etalon as single-mode selector in a laser cavity," Optics Express, Vol. 12, No. 11, pp. 2365-2370, 2004.
- [8]. R. H. Abram, K. S. Gardner, E. Riis, and A. I. Ferguson, "Narrow linewidth operation of a tunable optically pumped semiconductor laser," Optics Express, Vol. 12, No. 22, pp. 5434-5439, 2004.
- [9]. A. L. Schawlow and C. H. Townes, "Infra-red and optical masers", Physics Review, Vol. 112, No. 6-15, pp. 1940-1949, 1958.
- [10]. C. L. Tang, H. Statz and G. deMars, "Spectral output and spiking behaviour of solid state lasers", Journal of Applied Physics, Vol. 34, No. 8, pp. 2289-2295, 1962.
- [11]. A. Yariv, Optical Electronics, CBS College Publishing, 3rd edition, 1985, pp. 88-92.

- [12]. W. Demtroder, *Laser Spectroscopy – Basic Concepts and Instrumentation*, Third Edition, Springer-Verlag Berlin, 2002
- [13]. A. I. Ferguson, PhD thesis, University of St. Andrews, 1977.

Chapter Six

Optical In-well pumped 850nm VECSEL

6.1. Introduction

As already been introduced in Chapter Two, the use of in-well pumping can increase laser efficiency and decrease thermal problems. In this chapter this pumping concept was explored in an 850nm VECSEL. The characterization of three new wafers designed for in-well pumping is described. However the degradation of the laser output power with time was observed, which eventually hindered further investigation based on those new wafers. Hence an old wafer which was originally designed for barrier-pumping was used instead for a better understanding of the in-well pumping VECSEL system and future optimization. The high power operation ($>1\text{W}$) of the laser is obtained. The ways of optimizing the system has been investigated and are discussed.

6.2. Overview

Optically pumped vertical-external-cavity surface-emitting lasers (VECSELs) have been studied extensively for several years [1-3] and commercial products based on this technology are available. With only a few exceptions the vast majority of the research in this area makes use of quantum well (QW) gain structures based on InGaAs. These VECSELs usually emit light in the region between 950nm and 1100nm. Laser diodes operating around 800nm are used as pump sources. These are inexpensive and powerful commercial devices, well known for pumping high-power

Nd:YAG lasers. The current record of high power CW optically pumped VECSELs was achieved with an InGaAs based system producing 30W at 980nm [4].

VECSELs at shorter wavelengths (840-860nm; 670nm) are known to have much lower output power; the maximum reported values are 0.5W for 850nm [5] and 1W for 670nm laser [6]. One of the main problems with these systems is the availability of a suitable pump source. For example, VECSEL systems based on GaAs QWs, emitting around 850nm are normally pumped with laser diodes emitting below 700nm. However, these pump sources are significantly more expensive and less bright than their counterparts around 800nm. As a consequence GaAs based VECSELs are much less powerful than the equivalent systems based on InGaAs. In this chapter I will describe an optically pumped GaAs based system emitting in the 850nm region with an output power exceeding 1W, but pumped with an 806nm diode laser. Such a laser is very interesting for many applications requiring moderately high power in a single longitudinal and transverse mode. Here we are particularly interested in the applications for laser cooling, such as laser cooling of cesium [7]. These characteristics are of even higher importance for a system from which a frequency doubled output is required, e.g. as used in laser cooling of chromium or calcium [8-9].

The concept of in-well pumping of a VECSEL in the 850nm wavelength region has already been demonstrated in [10]. Here we explore the power scaling aspect of this technique. The main difference in pumping around 800nm instead of below 700nm is that the barrier region between the QWs now is transparent. Therefore, the pump light at 800nm is only absorbed in the QWs themselves (in-well pumping) and we estimate this absorption to be a mere 1% per QW per single pass [11-12]. In contrast, a gain structure designed and optimised for conventional barrier pumping (below 700nm), where the carriers are created between and subsequently drift into the QWs, has a typical absorption of 10% per barrier. The gain structure used for the present investigations was designed for barrier pumping and has only 17 QWs. Hence only a

relatively small fraction of the 800nm pump light is absorbed per pass through the gain region. However, in this chapter we will demonstrate that it is possible to increase the total absorption of the pump and hence increase the total output power of this type of system by carefully choosing the pump wavelength and by adapting the pump geometry. We will also discuss the optimization of the gain element.

In-well pumping has further advantages over the conventional barrier pumping than just allowing the use of the powerful 800nm diodes to pump 850nm VECSELs. As the quantum efficiency is increased less pump power is converted into heat and hence the VECSEL can be pumped harder. This aspect has recently been explored further in the context of in-well pumping of a 980nm laser with a 940nm pump [13]. Furthermore, in barrier pumping the absorption length of the barrier turns the number of QWs into a critical design parameter. Too few wells will result in a significant fraction of the ‘expensive’ 700nm pump light being transmitted through to and absorbed in the Bragg stack and substrate below the gain region. If there are too many QWs the last ones will not be pumped sufficiently and effectively act as absorbers at the VECSEL wavelength. In in-well pumping there is, in practice, no such limit. We are willing to accept that a significant fraction of the ‘inexpensive’ 800 nm pump light is not absorbed. VECSEL gain element designs usually include a Bragg stack immediately below the QW region, which is highly reflecting for the laser wavelength. This Bragg stack can be designed also to be highly reflecting for the pump light allowing it pass through the QW region once more and enabling recycling of any non-absorbed pump light similar to what has been demonstrated for the thin-disk solid state laser [14]. Finally, in-well pumping offers the possibility of extending the wavelength coverage of diode laser pumped VECSELs well below the 850nm region. For example fiber coupled laser diodes around 670nm with output power of several watts could be used to pump VECSELs emitting around 700 nm. This is a spectral region, which would otherwise be inaccessible with current pump laser technology. More information about in-well pumping can be found in

references [10], [13], and [15].

Apart from the investigations in optically pumped VECSELs emitting above 950nm [13] there are only a few reports on lasers operating around 850nm and 660nm where in-well pumping was used [10, 16]. In these cases the achieved output powers were much lower than is reported in this chapter. Some reports have been published about the characteristics of in-well pumping of vertical-cavity surface-emitting lasers (VCSEL) but no information is available on power scaling or achieved thresholds [17-18]. However, they do point out the importance of matching the wavelength with the resonant structure of the micro-cavity formed by the Bragg stack and the VCSEL surface, similar to the findings in this chapter.

6.3. Characterization of new VECSEL wafers

6.3.1. Wafer structures

The results in section 6.3 are based on the three samples (5mm x 5mm) taken from the wafers (USTR04-8-0/1/2) illustrated in table 6.1. Normally VECSELs are typically composed of MQWs where each well is placed at the anti-node of the cavity standing wave to achieve the maximum relative confinement factor. The position of the antinodes of cavity standing wave is then controlled by the optical thickness of the micro-cavity. Growth variation, process control, and the thermally induced refractive index changes can change the optical thickness of the micro-cavity, resulting in a mismatch between the antinodes and the QWs. This can affect high-power high-temperature operation of the VECSEL. Hence, in order to overcome this mismatch and achieve high effective gain over a large power and temperature regime, a four-well resonant periodic gain structure is proposed. In this design a highly reflecting DBR mirror consisting of 30 pairs of quarter-wavelength-thick AlGaAs and AlGaAs layers was grown on a 0.2mm thick GaAs substrate. On top of DBR mirror, the active region was grown. In that region,

four thin GaAs QWs are group and placed at each anti-node and are spaced by Al_{0.3}Ga_{0.7}As barriers. A thin capping layer (GaAs_{0.9}P) was grown on the top of the aluminum-rich confinement window (Al_{0.5}GaAs) in order to prevent oxidation. The total micro-cavity length was designed to be resonant to laser wavelength.

Layer No	Material	Group	Repeat	Mole Fraction (x)	Thickness (microns)
25	GaAs(x)P			0.9	0.010
24	Al(x)GaAs			0.5	0.1772
23	Al(x)GaAs			0.3	0.0354
22	GaAs				0.005
21	Al(x)GaAs			0.3	0.010
20	GaAs				0.005
19	Al(x)GaAs			0.3	0.010
18	GaAs				0.005
17	Al(x)GaAs			0.3	0.010
16	GaAs				0.005
15	Al(x)GaAs	2	4/5/6*	0.3	0.0648
14	GaAs	2	4/5/6*		0.005
13	Al(x)GaAs	2	4/5/6*	0.3	0.010
12	GaAs	2	4/5/6*		0.005
11	Al(x)GaAs	2	4/5/6*	0.3	0.010
10	GaAs	2	4/5/6*		0.005
9	Al(x)GaAs	2	4/5/6*	0.3	0.010
8	GaAs	2	4/5/6*		0.005
7	Al(x)GaAs			0.3	0.0978
6	Al(x)GaAs			0.98	0.0687
5	Al(x)GaAs		30	0.2	0.0588
4	Al(x)GaAs		30	0.98	0.0687
3	GaAs				0.02
2	Ga(x)InP			0.49	0.02
1	GaAs				0.2

Table 6.1. Designed structures of three new wafers; “*” denotes three different VECSEL wafers with different number of groups of QWs: 4 for USTR04-8-0 wafer; 5 for USTR04-8-1 wafer and 6 for USTR04-8-2 wafer.

6.3.2. Reflectivity

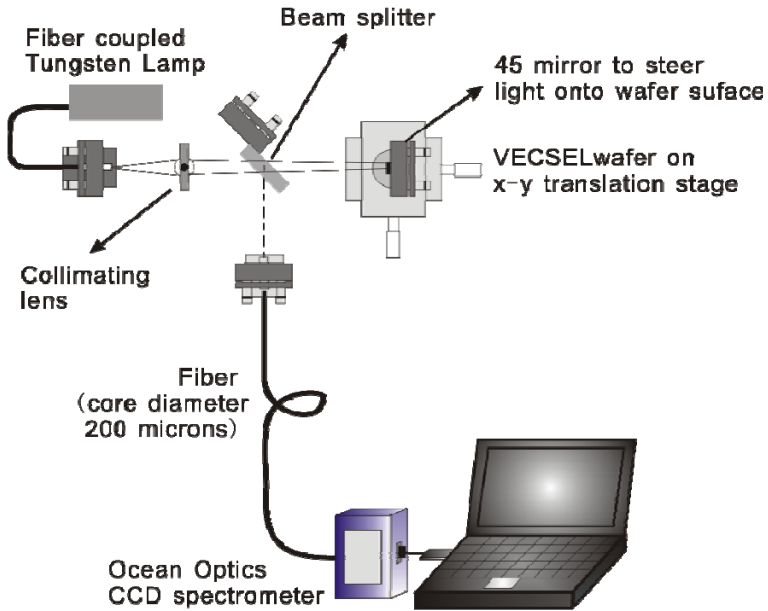


Fig. 6.1. Schematic experimental setup for reflectivity spectrum measurement.

In order to know the positions and strengths of the resonances for pumping and lasing as well as the position of the Bragg reflectance band, measurement of the reflectivity spectrum is required. Figure 6.1 shows the experimental setup for the measurement. White light is coming from a fiber coupled Tungsten lamp. The fiber end is imaged by a focal lens onto the VECSEL sample with the spot size of $500\mu\text{m}$ in diameter. The sample is put on a translation stage. A steering mirror is used to fold the incident light so as to excite the sample perpendicularly. The reflected light is detected by a multimode fiber coupled CCD spectrometer (Ocean Optics HQ2A0111, 0.2nm resolution). The measured reflectivity spectra for three samples are shown in Fig. 6.2. Comparing with three spectra curves, we see that the reflectivity structures for three samples are very similar but not overlapped. The structure has red-shifting as the number of the QWs increases. The width of the reflectivity stop-band is about 80nm. In the stop-band there is only one absorption enhanced resonance which is around 820nm.

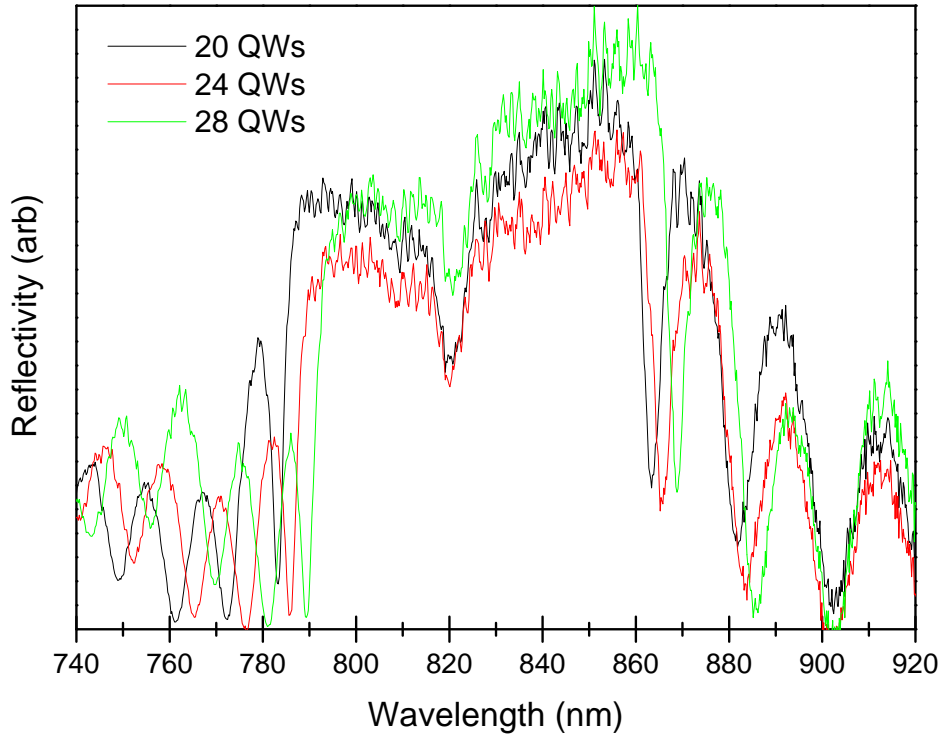


Fig. 6.2. Measured reflectivity spectra of the GaAs based VECSEL samples: black line for the sample with 20 QWs (USTR04-8-0); red line for the sample with 24 QWs (USTR04-8-1); green line for the sample with 28 QWs (USTR04-8-2).

6.3.3. Photoluminescence

Photoluminescence is a direct result of QW carriers being generated by the pump light and hence a good measure for the absorption in the structure. We investigated the PL intensity by varying exciting wavelength as well as pump incident angle. The experimental setup is shown in Fig. 6.3. The tunable CW Ti:Sapphire laser was used as the pump source. The laser beam was focused onto the sample to give a spot size of roughly $500\mu\text{m}$ in diameter. The sample was mounted on a rotation stage which can provide 360° rotation with the axis parallel to the front surface of the sample. For each wavelength the sample was rotated, the reflected power and normal PL intensity

were monitored simultaneously.

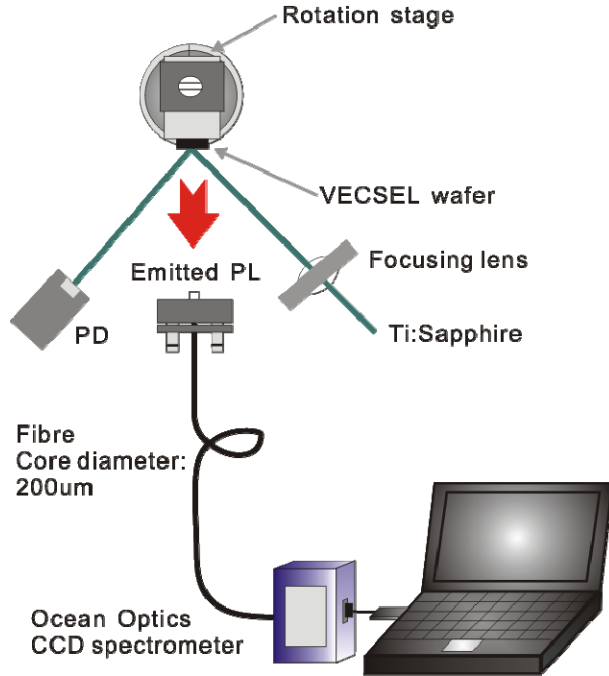


Fig. 6.3. Schematic set-up of the photoluminescence (PL) and reflectivity measurement.

The corresponding results are shown in Fig. 6.4, where the change for minimum reflectance with wavelength matches well with that for maximum PL intensity. Due to the temperature rise inside the sample by pumping with Ti: sapphire laser, the peak wavelength of the PL spectrum was measured to be around 830nm which is the designed laser operating wavelength. It is found that the best pumping wavelength is around 816nm where the PL was maximized. However this wavelength is out of the spectra range of our pump source (806nm-810nm). We need to optimize the pump angles for reachable wavelengths. By comparing with peak values for three curves, it is found that the maximized PL intensity decreases as the number of QWs increases. This can be possibly due to that some of the QWs for 24 QW or 28 QW sample are not excited and act as absorbers for the emitted PL. Hence the more QWs the sample has the lower maximized PL intensity it will generate. The angle at which the PL was maximized was also recorded for a range of wavelengths. The optimum angle decreases as the wavelength increases, which is consistent with the data shown in Fig.6.5. The reason for this is that the periodicity of the standing wave pattern of the

pump radiation along the cavity axis can be related to the pump wavelength λ_p by the expression $\lambda_{swp} = \lambda_p / \cos(\Theta_{in})$. By changing the incident pump angle so as to change internal angle of propagation Θ_{in} the periodicity of the standing wave pattern can be tuned to match the micro-cavity resonance 830nm at room temperature. The calculated optimum angle is 55° for the pump wavelength of 808nm. This is found to be consistent with the measured values: 50°, 55° and 60° for 20 QW, 24 QW and 28 QW samples respectively.

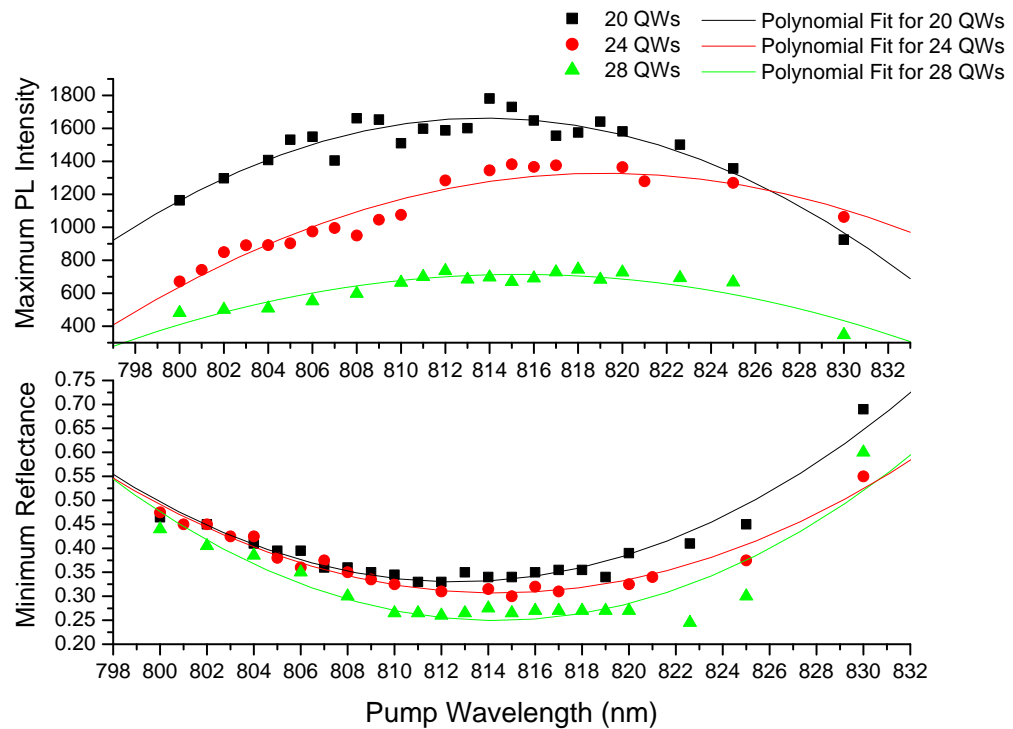


Fig. 6.4. Maximum peak-intensity of the PL and minimum reflectivity as a function of pumping wavelength for 20 QW wafer (black square symbols), 24 QW wafer (red circular symbols) and 28 QW wafer (green triangular symbols).

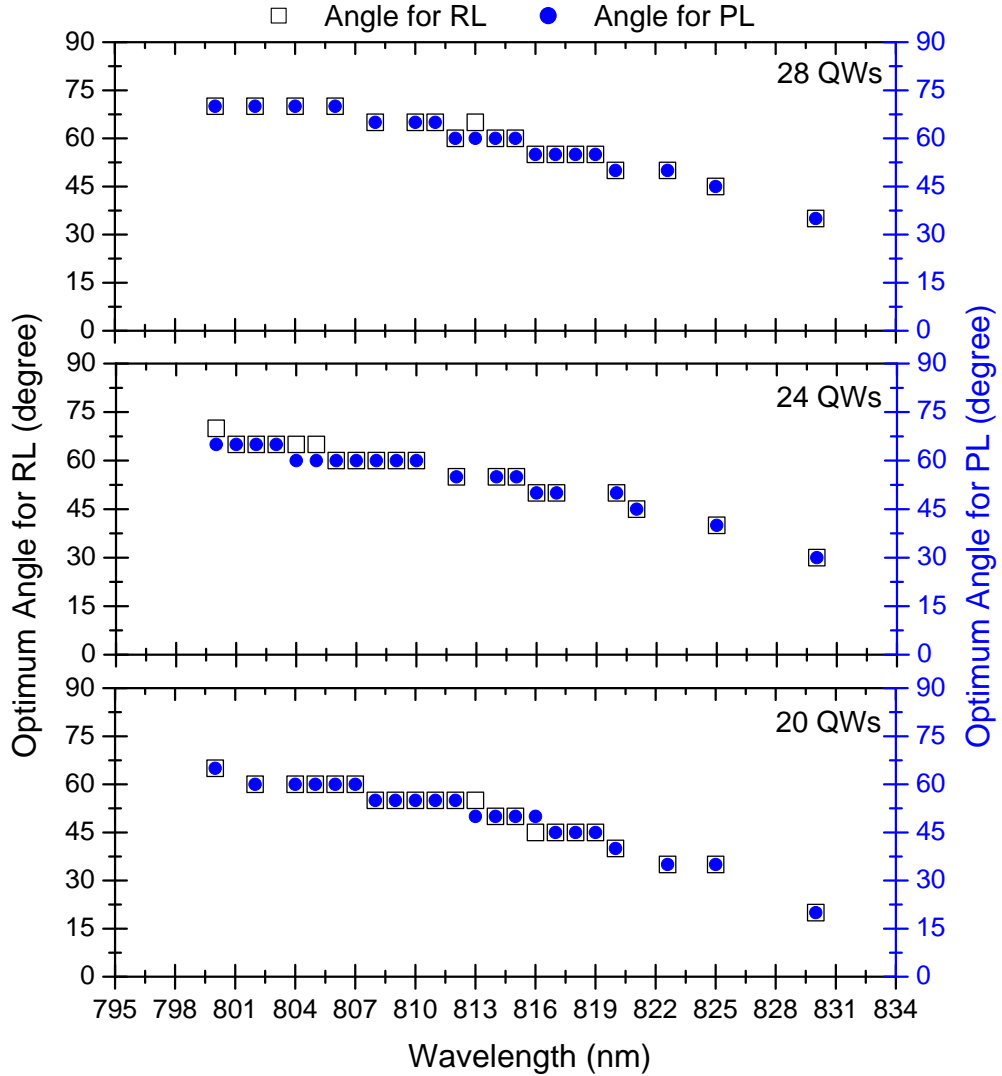


Fig. 6.5. Optimum incident angle for RL (left coordinate) and PL (right coordinate) versus pumping wavelength; (a) 20 QW wafer, (b) 24 QW wafer, (c) 28 QW wafer.

6.3.4. Laser operation

The sample used for investigating laser operation was from wafer design USTR04-8-2 (28 QWs). This sample bonded to a $\varphi 4 \times 0.5\text{mm}$ piece of diamond was mounted with indium foil in a standard brass VECSEL mount. Using the 14/11mm lens combination for the pump optics and a pump incidence angle of 50° , a three mirror laser cavity was set up as shown in Fig. 6.6. This consisted of a

ROC=-100mm folding mirror set at 55mm from the chip, with an output coupler (2%) at 250mm from the folding mirror. This provides a fundamental mode radius of about 39 μ m at the VECSEL chip. (The pump mode is about 38x59 μ m.) The pump diode temperature was 18.7°C, giving a pump wavelength of 808.9nm.

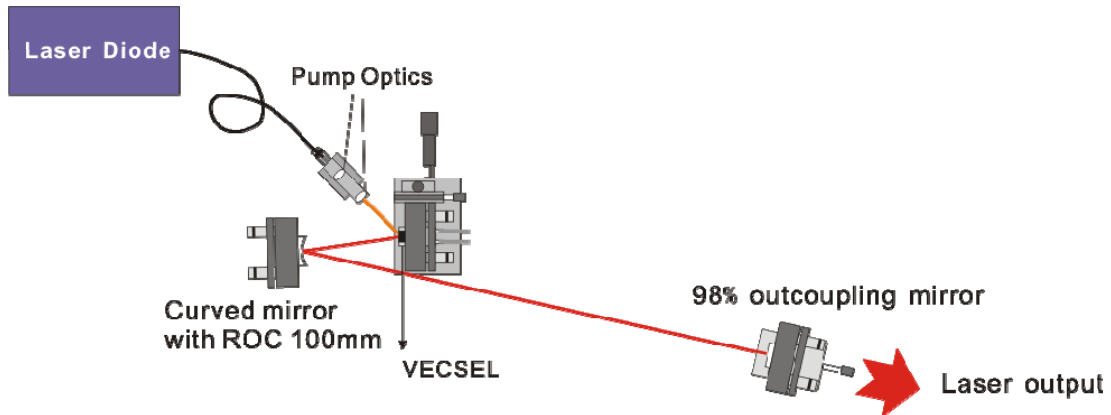


Fig. 6.6. Schematic diagram for three-mirror VECSEL cavity.

According to the results given in Fig. 6.5, the incidence angle of 50° is not optimized for current sample. This is due to the mechanical limitation of our setup. The highest output power obtained was 340mW. However, there were clear signs of device degradation with time. To try to quantify these effects, the output power of the device was monitored as a function of time. The results are shown in Fig. 6.7. There is a clear reduction on minute time scales. The laser power decreased to half of its maximum value only after about 40 minutes. Similar degradation was observed at all points on the sample that were tested. The mechanism for this is still under investigation. This suggests that this in-well pumped VECSEL system is not reliable. Similar observations have been found with the samples from other two wafers (USTR04-8-0/1). Hence we are forced to characterize the old 850nm VECSEL wafer which was designed for barrier pumping in order to obtain a better understanding on the in-well pumping based on VECSELS.

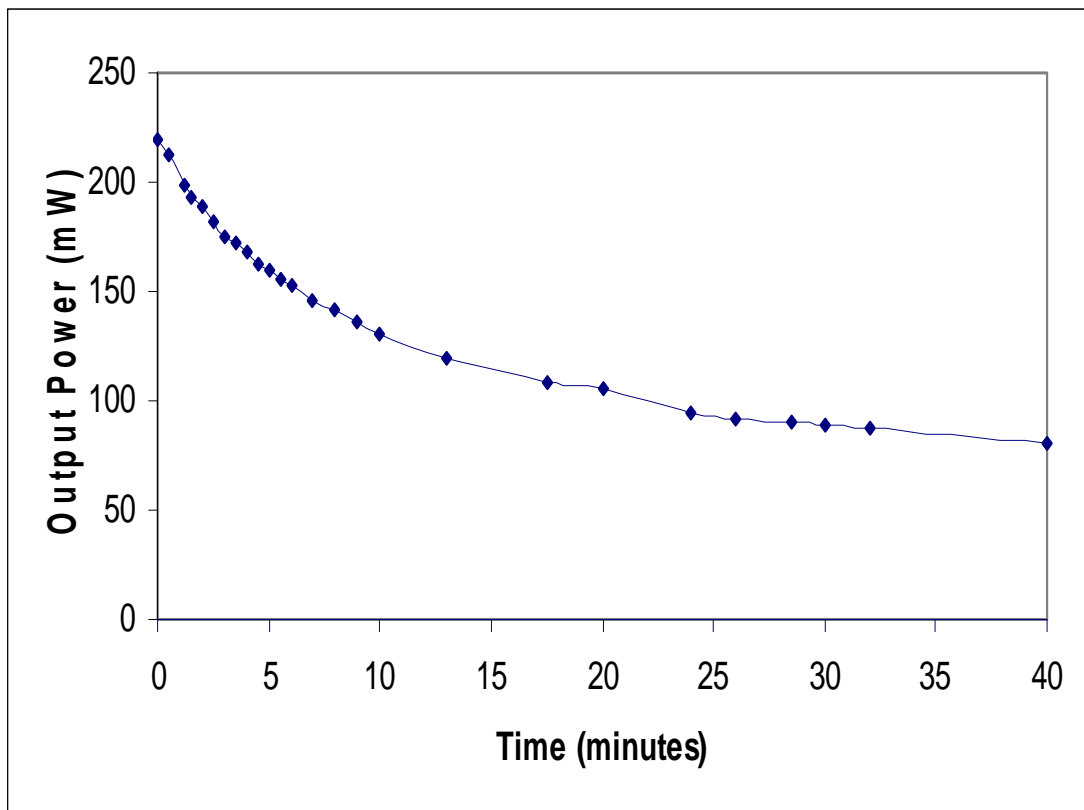


Fig. 6.7. The degradation of output power with time [19]

6.4. Characterization of the old wafer

6.4.1. Wafer structure

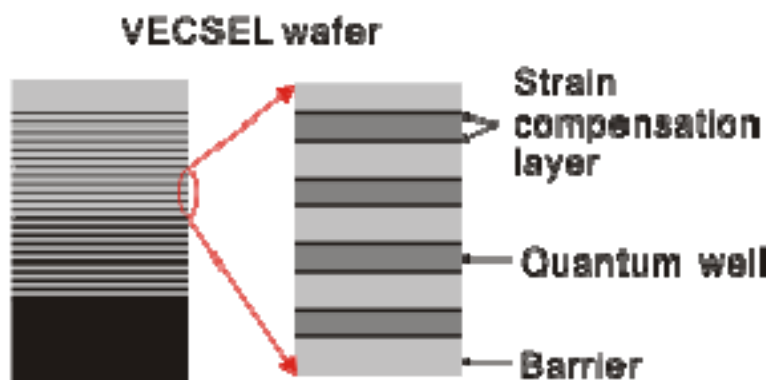


Fig. 6.8. Schematic of the VECSEL wafer structure

The basic structure of the VECSEL gain element used in this work has been

introduced in chapter two and is illustrated schematically in Fig. 6.8. A Bragg mirror containing 30 AlAs/ $\text{Al}_{0.18}\text{Ga}_{0.82}\text{As}$ layers was deposited on top of a GaAs wafer. This high reflective (HR) mirror has the central wavelength at 850nm and a bandwidth of 85nm FWHM, as shown in Fig. 6.8. Above the mirror is a gain structure consisting of 17 $\text{In}_{0.1}\text{Al}_{0.115}\text{GaAs}$ QWs each with a thickness of 10nm. This results in a band gap of 1.4573eV corresponding to emission at 851nm. The wells are separated by approximately half a wavelength of $\text{Al}_{0.26}\text{Ga}_{0.74}\text{As}$ layers. Next to each QW is a 5nm thick $\text{Al}_{0.115}\text{GaIn}_{0.1}\text{AsP}_{0.18}$ layer with a band gap of 1.65eV to compensate the strain induced by a lattice mismatch between QW and barrier. A 309 nm thick $\text{Al}_{0.5}\text{Ga}_{0.5}\text{As}$ layer is added on top of the gain structure increasing the total length of the micro-cavity to 2.55 μm . This corresponds to an anti-resonant structure at 850nm. A finishing layer of 20nm $\text{GaAsP}_{0.1}$ was added to protect the structure.

6.4.2. Reflectivity & PL

Before building the external cavity, the reflectance and photoluminescence (PL) spectrum of the gain medium was recorded for normal incidence, as shown in Fig. 6.8. From this we can clearly identify the positions and strengths of the resonances for pumping and lasing as well as the position of the Bragg reflectance band. The observed PL is a function of the QW emission and the spectral filtering caused by the micro-cavity resonances described above resulting in the main peak of the PL signal matching exactly with one of the absorption enhancement resonances. Due to the anti-resonant design of this wafer, the designed laser wavelength (approximately 850nm and defined by the resonant periodic gain) lies in the range between two resonances (840nm and 878nm). The resonances of the semiconductor structure are also found to be of importance in enhancing the pump absorption in the gain medium [10, 13]. When the cavity formed between the Bragg mirror and the VECSEL surface is resonant for a particular pump wavelength the pump intensity will build up resulting in an increased absorption. This not only leads to a sensitivity to the pump

wavelength for the in-well pumping scheme, which is much higher than for conventional barrier pumping [1], but also a significant dependence on the pump angle.

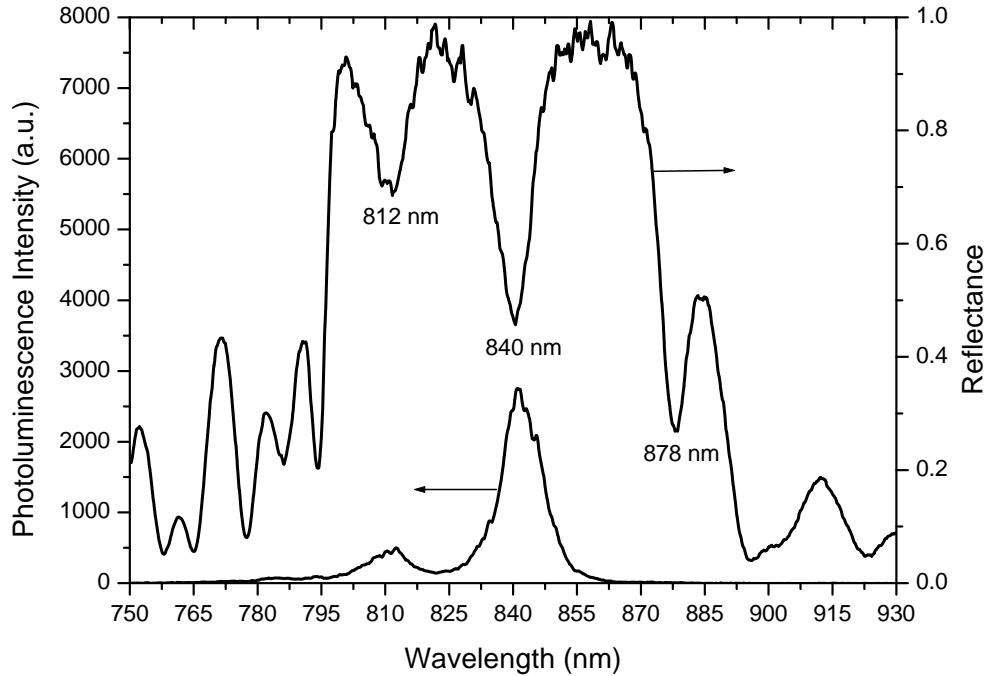


Fig. 6.8. Measured reflectance (right ordinate) and photoluminescence emission (PL) spectra (left ordinate) of the VECSEL sample at room temperature with normal incidence. The sample is excited by an 806 nm pump source.

6.4.3. Photoluminescence Excitation

Similar to the experiment described in section 6.3.3, we investigated the PL excitation spectra for different pump angles in order to find the optimum pump wavelength for a given incident angle. The difference here is to scan the wavelength for a chosen incidence angle. Figure 6.9 shows the PL excitation spectra of the VECSEL sample for near normal and 45° angle of incidence of the pump light. For this experiment a tunable CW Ti:Sapphire laser was used as a pump source. The PL was detected perpendicular to the VECSEL surface by using a multimode fibre

coupled CCD spectrometer. Point A and A' correspond to the same maximum but are separated by 15nm. This is the expected shift of resonance for a propagation angle of 11.7° inside the gain medium, which agrees well with the 45° angle of incidence. Point A and B are the two maxima of the micro-cavity separated by a free spectrum range (FSR) of 16.8THz corresponding to the 2.55μm thick gain structure. It has to be noted that a wavelength shorter than 790nm for the 45° curve and 810nm for the normal incidence curve the Bragg mirror is no longer highly reflecting and the behaviour of the micro-cavity is more complicated.

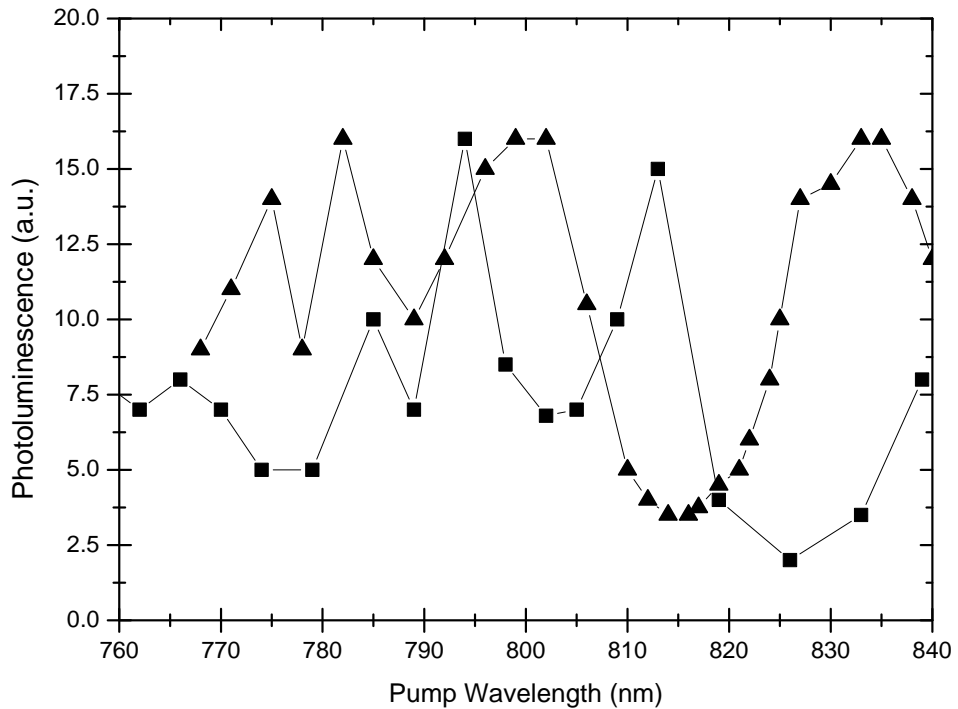


Fig. 6.9. Photoluminescence excitation spectrum. The peak fluorescence at around 840 nm is shown as a function of the excitation wavelength. The angle of incidence is near 0° for the square symbols and 45° for the triangular symbols, respectively. The operating temperature was 20°C, after [25]

Figure 6.9 indicates that the excitation is not optimum in the wavelength range of our current pump source (806nm – 811nm) and for an angle of incidence of 45°. In order to match the pump wavelength to a micro-cavity resonance the pump angle must be

reduced. A more detailed investigation on the optimum pump angle was carried out in the wavelength region of 800nm to 810nm.

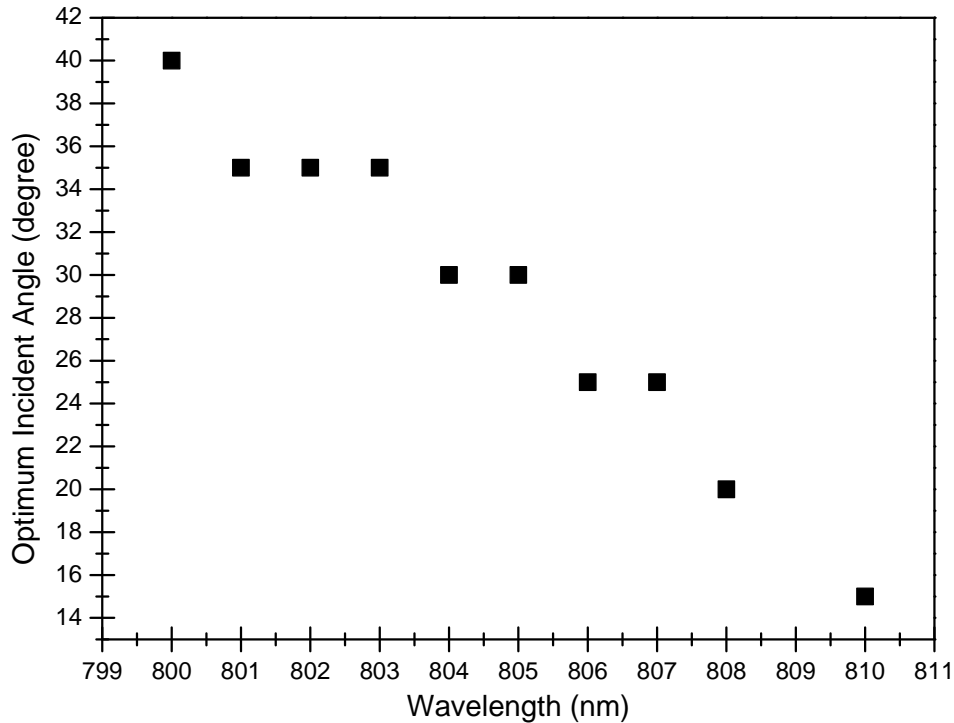


Fig. 6.10. Optimum pump angle as a function of pump wavelength. The optimum pump angle was taken to be that which resulted in the highest PL intensity at the 840 nm maximum. The operating temperature was 20°C.

By using the same experimental setup in section 6.3.3, we obtained the optimum angle for each pumping wavelength, as shown in Fig. 6.10. Similar to the observations described in section 6.3.3, the optimum angle decreases as the wavelength increases. This is consistent with the data shown in Fig.6.9. The reason for this is that the periodicity of the standing wave pattern of the pump radiation along the cavity axis can be related to the pump wavelength λ_p by the expression $\lambda_{swp} = \lambda_p / \cos(\Theta_{in})$. By changing the incident pump angle the periodicity of the standing wave pattern can be tuned to match the micro-cavity resonance (812

nm) as shown in Fig.6.8. The optimum angle is around 27° for 806nm decreasing to about 15° at 810nm. Due to the mechanic limitation of our system, we have to operate with a pump angle larger than 20° . The data presented on high power operation in this paper were taken with an 806nm pump incident at approximately 27° . The high sensitivity of the laser absorption on the pump wavelength indicates also that at all pump powers the operating temperature of the pump should be adapted to keep the diode emission wavelength fixed.

6.4.4. Laser operation

6.4.4.1. Experimental setup

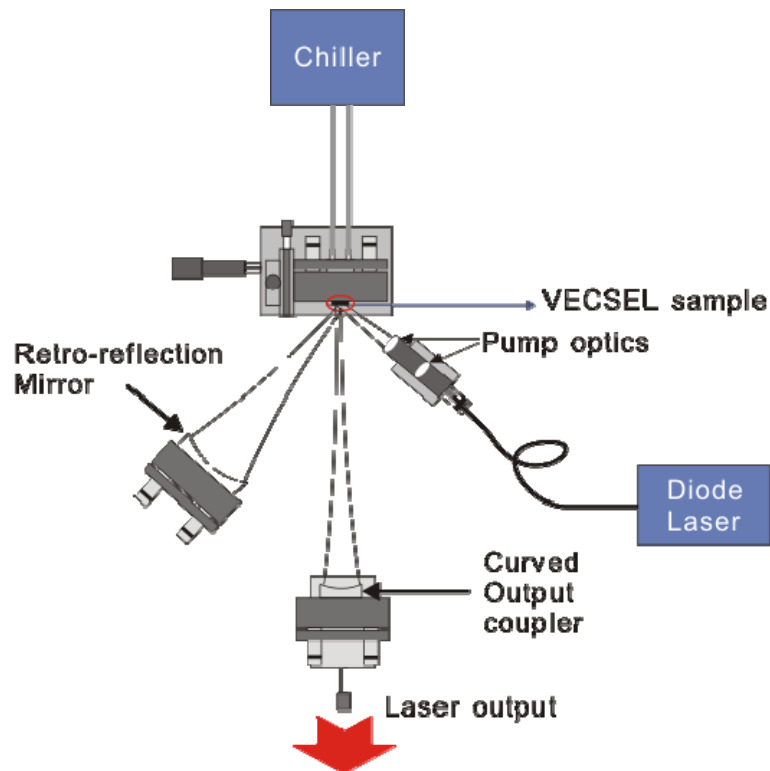


Fig. 6.11. The VECSEL structure. A highly reflecting Bragg mirror and a strain compensated gain region are grown on a GaAs substrate.

The VECSEL sample was firstly bonded to a $\varphi 4 \times 0.5\text{mm}$ piece of diamond. The whole device was then clamped between two copper plates and mounted on a

water-cooled copper block to control the cooling temperature T_C of the VECSEL gain chip, as shown in Fig 6.11. The laser cavity is formed by the HR Bragg mirror and an external curved output coupler (OC). The radius of curvature of the OC was 150mm and the reflectivity 98%. Due to the refractive index difference a fraction of the laser light is reflected at the diamond-semiconductor interface and a micro-cavity is formed between this surface and the Bragg mirror. Due to its resonances this micro-cavity can significantly enhance the pump absorption efficiency, which is discussed in the following part of this paper. The diamond-air interface causes an approximately 17% reflection loss of the pump light. This reflection also causes the diamond heat spreader itself to act as an etalon for the laser resulting in a channeled laser spectrum.

The pump source was operating at $\lambda_p=811\text{nm}$ at full power and a cooling temperature of 20°C . By cooling it down to $T_p=-6.7^\circ\text{C}$ the wavelength dropped to $\lambda_p=806\text{nm}$ while the output power did not change significantly. The laser was coupled into a 100\mu m fibre with an NA of 0.22. After the focusing system the spot size on the VECSEL was roughly 110\mu m in diameter. The length of the external cavity was around 149mm. Different pump incident angles were investigated in order to search for the optimum angle for best pump absorption at the specific pump wavelength. After a single pass through the gain region the remaining pump light was reflected by the HR-Bragg mirror and passed through the gain region a second time. The remaining pump power, approximately 65%, which was not absorbed after the double pass, could be reflected back onto the VECSEL with a curved gold coated mirror. With this additional recycling loop approximately 92% of the non-absorbed pump power could be launched in a second double pass through the VECSEL. However of this 17% will again be lost at the diamond-air interface. These losses could be greatly reduced from the present total of 34% to less than 5% by use of AR coatings at the diamond heat spreader at pump wavelength.

6.4.4.2. Experimental results

For laser operation, an external mirror with $R_C=150\text{mm}$ is aligned to complete the laser cavity. While keeping the pump constant (both wavelength and power) and only changing the temperature of the mount onto which the gain element was attached, the optimum laser cooling temperature T_C at maximum pump power was found to be 20°C , as shown in Fig. 6.12. The actual QW region of the gain element will be operating at a significantly higher temperature due to the thermal gradients across the semiconductor material [20] and we can therefore expect T_c to depend on the heat load (absorbed pump power) of the system.

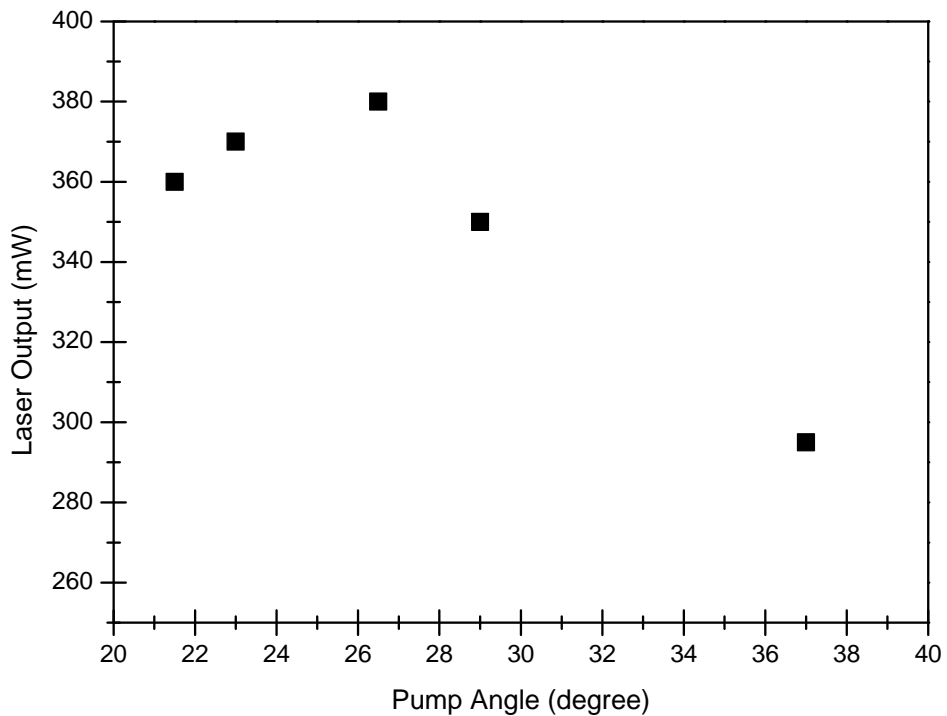


Fig. 6.12. Maximum laser output power versus pump angles

After setting the pump angle to be around 27° and laser cooling temperature to 20°C , a maximum power of 380mW was obtained and no obvious laser degradation was

found. The laser was clearly operating with higher order transverse modes. The reflected pump light was now imaged back onto the gain element using a gold coated curved mirror. This pump recycling provided an additional double-pass through the QW gain region and resulted in an increase of the laser power by a factor of 2.5. The additional heat load on the gain medium resulted in a drop of the optimum laser cooling temperature to 15°C.

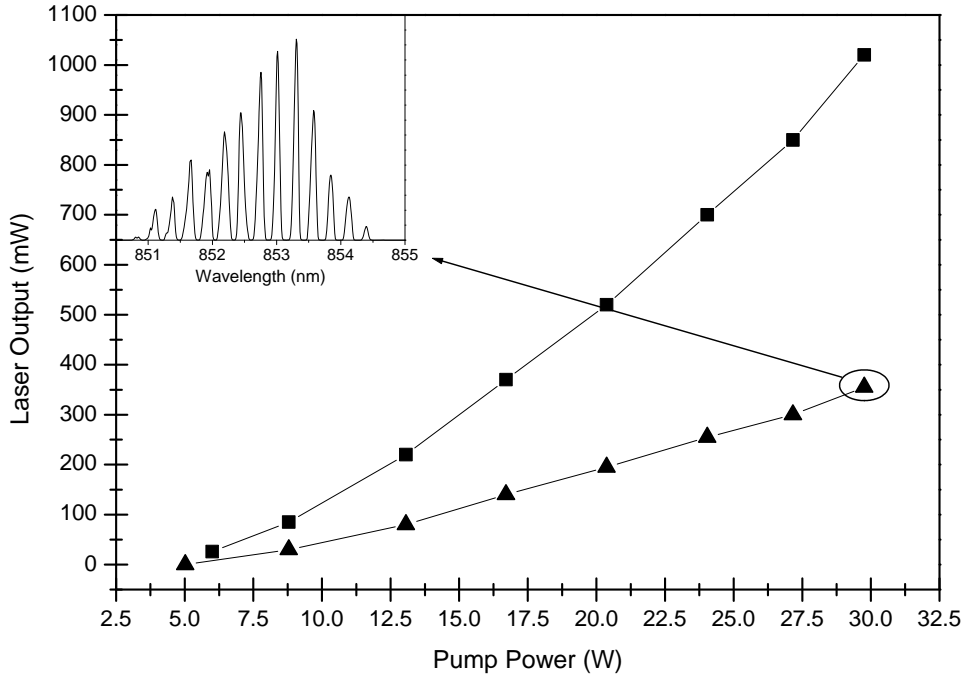


Fig. 6.13. Laser output power versus pump power at a pump angle of 27° and a laser temperature of 15°C with (upper curve with square symbols) and without (bottom curve with triangular symbols) retro-reflection. The pump wavelength was fixed at 806 nm by changing pump cooling temperature at different powers. The inset shows the VECSEL spectrum at maximum pump power and no recycling. The structure in the spectrum is due to the diamond heat spreader acting like an etalon.

The output power of the VECSEL as a function of the pump power with and without recycling of the pump light back to the gain medium was investigated and is shown in Fig. 6.13. Also shown is an example of the output spectrum of the laser. The individual peaks in this channeled spectrum are separated by the FSR of the diamond. Suppression of this etalon is possible using an AR coated and wedged heat spreader

[21].

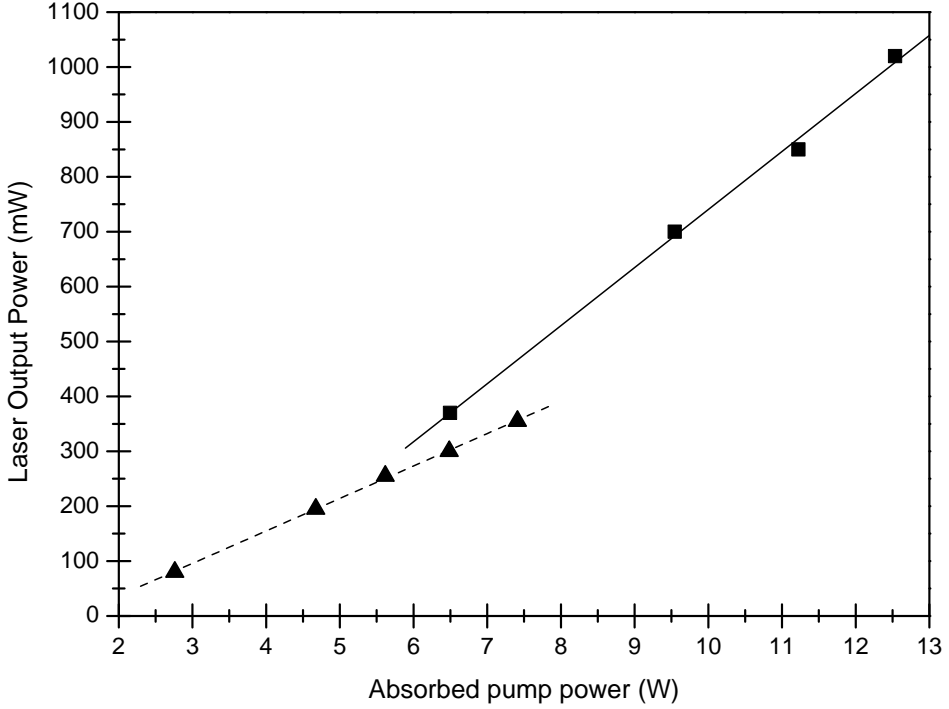


Fig. 6.14. Laser output power versus absorbed pump power for the laser with (square symbols) and without (triangular symbols) pump retro-reflection. The slope efficiencies for the laser without and with pump recycling are 6% and 10.6% respectively.

The maximum output power of 1.02W at 855nm was achieved at a pump power of 29.8W, this corresponds at an estimated absorbed power of 12.5W, see also Fig. 6.14. As indicated above, the pump wavelength was kept constant at 806nm. The absorption in the QW region was estimated from measurements of the pump reflectivity. After subtracting the constant reflection loss (17%) at the front surface of the diamond for each pass the double-pass absorption of the VECSEL without retro-reflection and at maximum pump (29.8W) was around 30%. With retro-reflection in place 45% of total incident pump power was reflected back onto the gain medium. Based on measurements of an increase in the absorption with increasing pump power due to the heating of the gain region we estimate the overall

double-pass absorption to be about 35%. It is apparent from both sets of data that the output power increases more rapidly than the normal linear dependence on pump power. This is due to the fact that the pump wavelength and laser temperature were optimized for the highest power level. Since the temperature coefficient of the micro-cavity resonances is $\sim 0.1\text{nm/K}$, the resonant wavelength shifts to the blue when the pump power decreases and thus laser temperature drops. Hence the pump radiation is detuned gradually from the resonance generating the concave curves. From the shift of resonance with pump power we estimated a gain-region temperature increase of 50°C which is also in accordance with literature values [20]. If, rather than plotting the laser output power against the incident pump power, we use the additional measurement of the reflected pump power to plot it against the absorbed, we recover straight line fits. Figure 6.14 shows this data. The slope efficiencies for the lasers with and without pump retro-reflection are determined to be 10.6% and 6% respectively. We attribute this difference to the fact that the laser temperature for this data set (15°C) was optimized for the highest power operation with pump retro-reflection. The slope efficiency for in-well pumping was found to be less than the efficiency for barrier pumping (20%-30%) when the same wafer was used. This can be attributed to the fact that the structure of the wafer is not optimized for in-well pumping. This is discussed in the following section.

6.4.4.3. Multi-pass pump scheme

As seen from the results presented in Fig. 6.13 there is still significant pump power left even after one recycling loop of the pump light. Additional recycling loops could therefore potentially increase the absorption and hence the total output power of the VECSEL. A multi-pass pump set-up similar to that demonstrated for thin-disk solid state lasers [14] would be the preferred geometry for an in-well pumped system. As the absorption per single pass in a VECSEL structure is higher than in a solid state

thin disk fewer recycling loops would be required. Hence multi-pass pump geometry was investigated, as shown in Fig. 6.15.

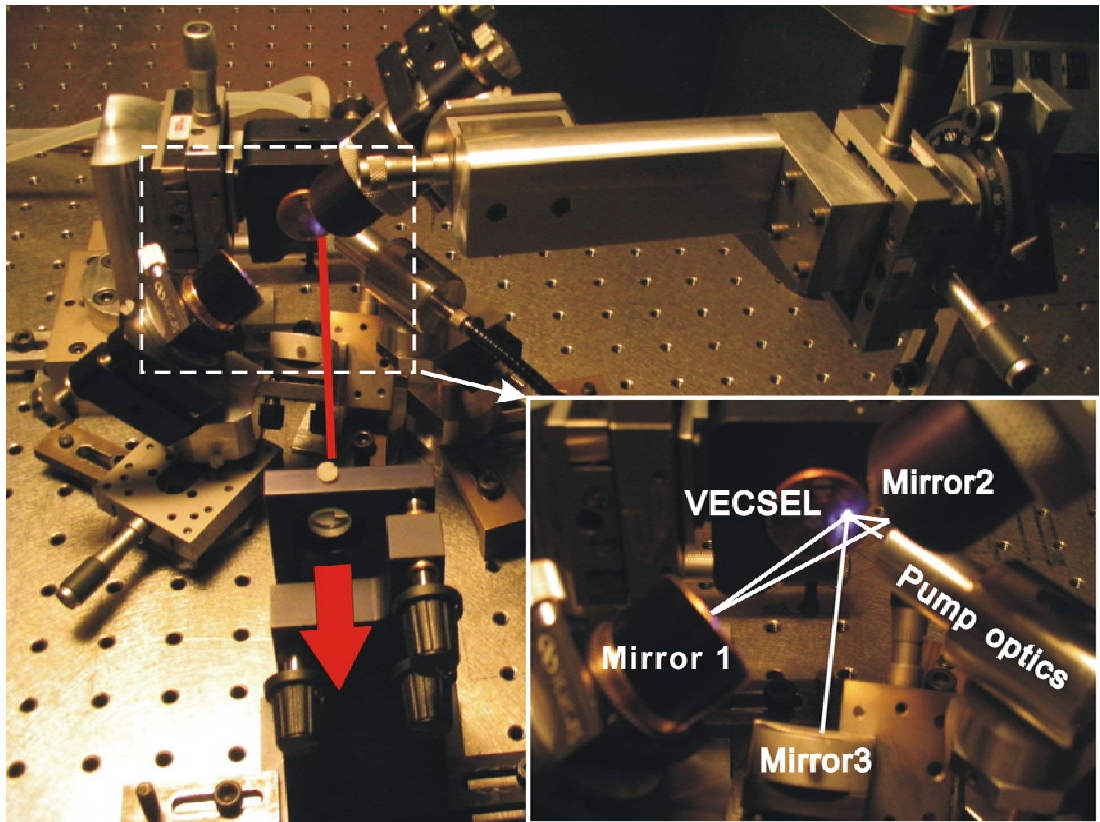


Fig. 6.15. Experimental setup for an in-well pumped VECSEL with multi-pass pump geometry.

Due to the mechanical limitation, the pump angle was increased to about 37° . Two gold coated off-axis parabolic mirrors with effective focal length of 50.8mm and one gold coated curve mirror with effective focal length of 50mm were used to form the pump recycling system. In this configuration, pump light travels four times (4 double passes) through the laser gain element. If a constant double-pass absorption is assumed (absorption is independent on the increase of the pump power) to be 30%, a total pump absorption for this pump recycling system is about 43%. This gives about 19% increase of the absorption when compared with 36% for simple pump geometry described in the last section. By carefully aligning laser system, laser power of 840mW was obtained when the laser and pump cooling temperature were set to be

25°C and -6.5°C respectively. The simple retro-reflection system was also tried in order to make comparison. The laser power was 770mW when only one reflection mirror was used. The rise of the laser power is only around 9% if the laser gain is assumed constant, which is less than the ideal 19% increase. The reason for this less efficiency could possibly be that pump beam would catch astigmatism after traveling through the off-axis parabolic mirrors. Hence it leads to the mismatch of mode size between the laser and the pump and decrease the laser efficiency.

6.4.5. Discussion

In order to optimize future designs of optically in-well pumped VECSELs there are three aspects which have to be taken into account. The first two relate to the resonant structure built into the design of the gain element. They are the intra-cavity enhancement and the resonant periodic gain (RPG) structure [22], which are traditionally only optimized for the laser wavelength. For a conventional barrier pumping VECSEL device, a standing wave pattern of the laser electrical field is formed between the front surface of semiconductor and the Bragg reflector. The QWs are placed at the antinodes of the standing wave pattern in order to enhance the intensity of the laser field. This gives an enhancement for the intensity by a factor of $\Gamma_{RPG} = 2$, where Γ_{RPG} represents the enhancement factor for resonant periodic gain, compared to the average intensity. The intensity of the laser field can be further enhanced by the micro-cavity which is formed between the Bragg reflector and the surface of the structure. This can be designed to be resonant at the laser wavelength to yield a VECSEL with a particularly low threshold. For barrier pumping it is not necessary to consider any interference effects involving the pump as it is largely absorbed in a single passage through the structure and the reflectance band of the Bragg stack is generally not wide enough to cover the pump wavelength. However for in-well pumping the overlap between the standing wave pattern of the pump

radiation and the locations of QWs needs to be optimized. The cavity enhancement factor [13] can be described as $\Gamma_{cav} = \frac{n_{se} \cdot I_{cav}}{n_d \cdot I_0}$, where n_{se} and n_d are the refractive indices of semiconductor and diamond respectively and I_{cav} , I_0 correspond to intra-cavity field intensity and incoming field intensity. The electrical field distribution of the pump has been calculated by determining the overlap integral of the pump field over the wells.

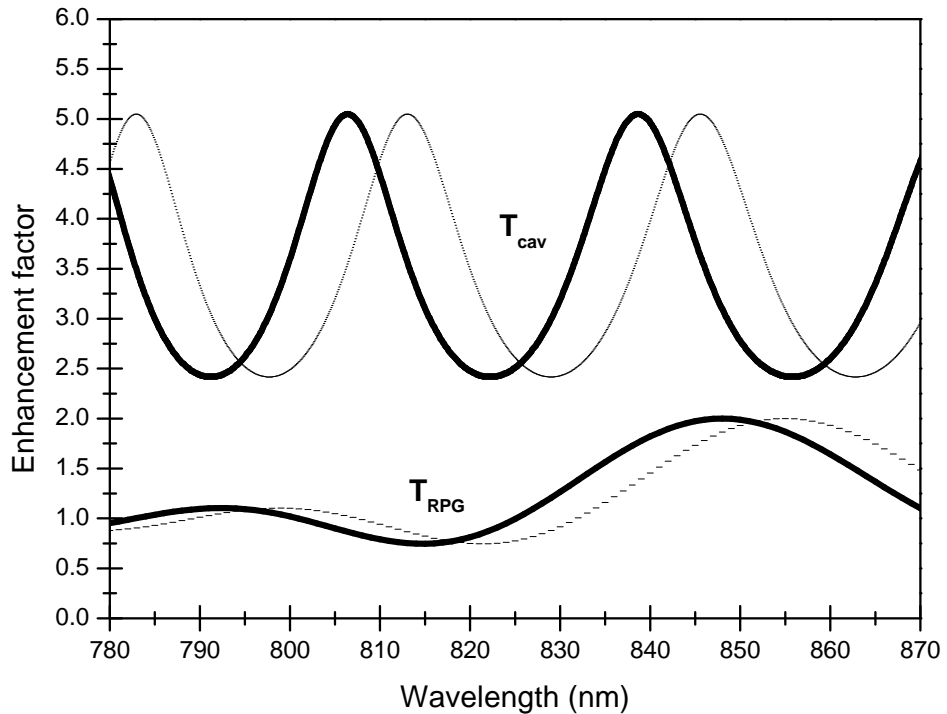


Fig. 6.15. Calculated values of the enhancement factors (Γ_{cav} and Γ_{RPG}) as a function of wavelength for both normal incidence (dash line) and at an angle of 27° (solid line).

The enhancement factors Γ_{cav} and Γ_{RPG} can be calculated based on our knowledge of the composition of the semiconductor structure used in this paper and their dependencies as a function of wavelength are shown in Fig. 6.15. The set of

curves with dash line are the enhancement factors (Γ_{cav} and Γ_{RPG}) at normal incidence. While the other set of curves with solid line are the factors at an incident angle of 27°. The curves shift to shorter wavelength as the incident angle increases. Due to the anti-resonant structure of the wafer, the main peak of the Γ_{RPG} curve does not overlap with the peaks of the Γ_{cav} function. From the overlapping function (Γ_{RPG}) for the case of 27° incident angle, a wavelength of 847 nm would be optimum. However, it is far off a micro-cavity resonance and rather close to the laser wavelength which will lead to strong absorption bleaching. Hence it is not suitable for pumping. The cavity resonance at 840 nm corresponds still to a high value of Γ_{RPG} but remains very close to the laser wavelength. We are therefore forced to select our pump wavelength to be either another resonance of the micro-cavity or the second lower peak for RPG enhancement depending on which factor is dominant. For our current wafer structure, the micro-cavity enhancement is stronger than the enhancement by RPG structure. Hence the resonance at 806 nm is chosen for our pumping wavelength, where the average RPG factor $\Gamma_{RPG} = 0.868$ indicating a rather poor overlap between pump and QWs. Indeed, by modelling the pump electric field distribution, the absorption at each QW inside the current sample was also examined. It is found that three QWs located in the part of the active region close to DBR hardly absorb pump light. Those QWs will act as absorbers to the laser radiation. This could partly explain the relatively high internal loss of the laser (~3%) [23]. Hence it would be advantageous in a future design to replace un-pumped QWs with pump transparent spacers and possibly group two or more QWs at the anti-node of the cavity standing wave in order to maintain their total number. This would not only reduce the internal loss of the laser but also increase the total pump absorption as Γ_{RPG} approaches its theoretical maximum limit of 2.

The third aspect of the improvement of the overall performance of in-well pumping

is to increase the absorption per QW. This could be achieved by widening the QWs. However, in order to maintain the quantum nature this would require the walls of the wells to be higher. This is entirely feasible as the barrier band gap is a free parameter for an in-well pumped system.

6.5. Conclusion

The characterizations of three new VECSEL wafers were presented. However the investigations were suspended due to the laser degradation. And an old wafer optimized for barrier pumping was used instead. After whole chain of characterization on an old wafer sample starting with reflectivity and photoluminescence measurements at wafer level via the optimization of the pump geometry, an output of 1W at 850nm has been demonstrated from an optically in-well pumped VECSEL. Laser gain has also been investigated demonstrating a logarithmic dependence on the pump intensity. The pump light was only absorbed in the QWs. It has been shown that the absorption of the pump light is influenced by a weak micro-cavity in the gain element and therefore the wavelength of the pump source is crucial. The absorption can be further enhanced by optimizing the overlap integral of the pump field over QWs together with grouping QWs. Secondly the absorption per QW as well as the number of QWs can be increased. Thirdly, the surface reflection loss from the uncoated diamond heat spreader can be eliminated by adding suitable coatings which should have two transmission peaks, one for laser wavelength the other for pump wavelength with chosen incidence angle. By taking these suggestions into account, it seems reasonable to expect that future systems would achieve output powers of several watts around 850nm with a good beam quality, similar to the system reported by emitting at 1000nm [4]. In chapter 4 a new wafer design for in-well pumping will be described in detail.

6.6. Reference

- [1]. W. J. Alford, Th. D. Raymond, and A. A. Allerman, "High power and good beam quality at 980 nm from vertical external-cavity surface-emitting laser," Journal of Optical Society of America B, Vol. 19, No. 4, pp. 663-666, 2002.
- [2]. R. Haering, R. Paschotta, A. Aschwanden, E. Gini, F. Morier-Genoud, and U. Keller, "High-Power Passively Mode-Locked Semiconductor Lasers," IEEE Journal of Quantum Electronics, Vol. 38, No. 9, pp. 1268-1275, 2002.
- [3]. M. A. Holm, D. Burns, A. I. Ferguson, and M. D. Dawson, "Actively Stabilized Single-Frequency Vertical-External-Cavity AlGaAs Laser," IEEE Photonics Technology Letters, Vol. 11, No. 12, pp. 1551-1553, 1999.
- [4]. J. Chilla, St. Butterworth, A. Zeitschel, J. Charles, A. Caprara, M. Reed, and Luis Spinelli, "High Power Optically Pump Semiconductor Lasers," in *Solid State Lasers XIII: Technology and Devices*, R. Scheps, H. J. Hoffman, eds., Proc. of SPIE 5332, pp. 143-150, 2004.
- [5]. J. E. Hastie, J. M. Hopkins, S. Calvez, C. W. Jeon, D. Burns, R. Abram, E. Riis, A. I. Ferguson, and M. D. Dawson, "0.5-W Single transverse-mode operation of an 850-nm diode-pumped surface-emitting semiconductor laser," IEEE Photonics Technology Letters, Vol. 15, No. 7, pp. 894-896, 2003.
- [6]. J. E. Hastie *et al.* Manuscript in preparation.
- [7]. C. Salomon, J. Dalibard, W. D. Phillips, A. Clairon, S. Guellati, "Laser cooling of Cesium atoms below 3-mu-K," Europhysics Letters, Vol. 12, pp. 683-688, 1990.
- [8]. T. Kurosu, and F. Shimizu, "Laser cooling and trapping of calcium and strontium," Japanese Journal of Applied Physics, Part 2- Lett. Vol. 29, No. 11, pp. L2127-L2129, 1990.
- [9]. C. C. Bradley, J. J. McClelland, W. R. Anderson, and R. J. Celotta, "Magneto-optical trapping of chromium atoms," Physical Review A, Vol. 61, No. 5, 053407 2000.
- [10]. M. Schmid, S. Benchabane, F. Torabi-Goudarzi, R. Abram, A. I. Ferguson, and E. Riis, "Optically in-well pumping of vertical-external-cavity surface-emitting laser," Applied Physics Letters, Vol. 84, No. 24, pp. 4860-4862, 2004.

- [11]. Y. A. Chang, J. R. Chen, H. C. Kuo, Y. K. Kuo, and S. C. Wang, "Theoretical and Experimental Analysis on InAlGaAs/AlGaAs Active Region of 850-nm Vertical-Cavity Surface-Emitting Lasers," *Journal of Lightwave Technology*, Vol. 24, No. 1, pp. 536-643, 2006.
- [12]. L. A. Coldren, and S. W. Corzine, *Diode Lasers and Photonic Integrated Circuits*, (John Wiley & Son, New York, 1995).
- [13]. S.-S. Beyertt, M. Zorn, T. Kubler, H. Wenzel, M. Weyers, A. Giesen, G. Trankle, and U. Brauch, "Optical In-Well Pumping of a Semiconductor Disk Laser With High Optical Efficiency," *IEEE Journal of Quantum Electronics*, Vol. 41, No. 12, pp. 1439-1449, 2005.
- [14]. A. Giesen, H. Hugel, A. Voss, K. Wittig, U. Brauch, and H. Opower, "Scalable concept for diode pumped high power solid-state lasers," *Applied Physics B*, Vol. 58, No. 5, pp. 365-372, 1994.
- [15]. M. Schmid, "VECSELs: An attractive new source in the Near-IR," *Photonics Spectra November*, pp. 58-64, 2004.
- [16]. M. Muller, C. Kamutsch, J. Luft, W. Schmid, K. Streubel, N. Linder, S.-S. Beyertt, U. Brauch, A. Giesen, and G. H. Dohler, "Optically pumped vertical-external-cavity semiconductor thin disk laser with cw operation at 660nm," in *Proceedings of International Symposium on Compound Semiconductor* 174, pp. 427-430, 2002.
- [17]. K. J. Knopp, D. H. Christensen, and J. R. Hill, "Vertical-cavity surface-emitting lasers with low-ripple optical pumping windows," *IEEE Journal of Selected Topics in Quantum Electronics*, Vol. 3, No. 2, pp. 366-371, 1997.
- [18]. M. J. Bohn and J. G. McInerey, "Resonant optical pumping of vertical-cavity surface emitting lasers," *Optics Communications*, Vol. 117, No. 1-2, pp. 111-115, 1995.
- [19]. A. J. Kemp, 051030 Review of 830 nm material, 2005
- [20]. A. J. Kemp, G. J. Valentine, J. M. Hopkins, J. E. Hastie, S. A. Smith, S. Calvez, M. D. Dawson, D. Burns, "Thermal management in vertical-external-cavity surface-emitting lasers: Finite-element analysis of a heatspreader approach," *IEEE Journal of Quantum Electronics*, Vol. 41, No. 2, pp. 148-155, 2005.

- [21]. R. H. Abram, K. S. Gardner, E. Riis, and A. I. Ferguson, "Narrow linewidth operation of a tunable optically pumped semiconductor laser," *Optics Express*, Vol. 12, No. 22, pp. 5434-5439, 2004.
- [22]. M. Y. A. Raja, S. R. J. Brueck, M. Osinski, C. F. Schaus, J. G. McInerney, T. M. Brennan, and B. E. Hammons, "Resonant periodic gain surface-emitting semiconductor-lasers," *IEEE Journal of Quantum Electronics*, Vol. 25, No. 6, pp. 1500-1512, 1989.
- [23]. S. McGinily, "Optically pumped semiconductor vertical external cavity surface emitting lasers," PhD thesis, University of Strathclyde, 2006.

Chapter Seven

Conclusions and Outlook

The capability of generating high output power, ultra-short pulses and narrow laser linewidth has made VECSEL an attracting device with versatile applications. High power VECSELs with near perfect beam quality can be used to pump the fiber amplifiers or used as a light source in free space communications. Ultra-short high peak power pulses from mode locked VECSELs are well suitable for two photon microscopy and nonlinear frequency conversion. While stable single frequency VECSELs can be used for laser cooling and high precision spectroscopy. Motivated by such a wide range of applications, the work contained in this thesis was carried out. Three operations, mode locking, single frequency and high power operation, associated with VECSELs operating in near infrared have been investigated. The design, development and characterisations of optically pumped VECSELs are discussed.

Based on the design principles introduced in Chapter Two, two semiconductor wafers (980nm and 850nm) were grown by a commercial MOCVD. The work in Chapter Four and Chapter Five is based on the 980nm wafer while 850nm wafer has been described in Chapter Six.

Chapter Four is concerned with the investigations of a synchronously mode locked VECSEL lasing at around 975nm. Detailed studies of the laser characteristics as a function of pump duration and cavity tuning were performed showing the potentials as well as the limitations of the synchronous pumping approach for mode-locking. The output pulses had duration of 10-40ps for ps as well as for fs pumping. This

indicates strong chirping due to the optical pumping-induced carrier generation and due to SPM by gain saturation. These processes were analyzed in some detail. The sign of the chirp of the laser pulses was found to be flipped when the laser cavity was detuned across the optimum position. Chirp compensation was effectively achieved by using either a grating-pair or a fiber. Nearly transform-limited pulses with duration of a few hundred fs with peak power ranging from 300W to 1.3kW were obtained. Thus it appears that synchronous pumping might be useful to provide ultrashort pulse sources at repetition rates of about 100MHz in spectral regions which cannot be accessed directly by other sources (mainly the Ti:Sapphire laser). In order to conquer the limitation caused by massive chirping, more efficient techniques for external pulse compression or intra-cavity dispersion will be helpful. And it would also be beneficial to combine the in-well pumping where the dynamics of the gain build-up is expected to be faster with the synchronous mode locking.

In contrast to the laser mode locking where broad laser bandwidth is essential, single frequency operation of the VECSEL demonstrated in Chapter Five is to generate narrow linewidth output. A combination of a birefringent etalon and a BRF was inserted into the laser cavity to allow single longitudinal mode to oscillate. A novel technique based on the birefringent etalon and a polarization analysing system was introduced and applied to stabilize the etalon. The laser cavity was stabilized by locking it to an external reference cavity (FPI). The stable laser operation was obtained and the laser linewidth was measured to be 45kHz. A fine tuning range of 4GHz together with 9nm coarse tuning range was achieved. The maximum output power was found to be 260mW. In future work, much narrower linewidth is expected if the electronic noises can be eliminated and a better control over the environmental conditions is obtained. Furthermore, the techniques for single frequency operation can be applied to other spectral regions, especially to visible. High power single transverse mode operation of a red VECSEL has already been developed. Hence it will be natural to develop a compact diode pumped single frequency red VECSEL

which can be used in many applications such as photodynamic therapy (PDT).

In Chapter Six, the results on an optically in-well pumped VECSEL were presented. This includes the characterizations of three new VECSEL wafers which were designed for in-well pumping. However the investigations were suspended due to the laser degradation. And an old wafer optimized for barrier pumping was used. After whole chain of characterization on an old wafer sample starting with reflectivity and photoluminescence measurements at wafer level via the optimization of the pump geometry, an output of 1W at 850nm has been demonstrated. A discussion on the ways of optimizing the laser system including pump geometry and wafer structure is also given. Future work will involve in designing a new wafer based on the same material system (GaAs/AlGaAs) with optimised structure. The successful wafer design in conjunction with in-well pumping can be applied to other interesting VECSEL wavelengths to significantly increase the output power. For example, in-well pumping of a $2.3\mu\text{m}$ GaSb based VECSEL is expected to greatly improve the laser power. High power $2.3\mu\text{m}$ VECSEL is suitable for a variety of applications such as Light Detection and Ranging (LIDAR) applications, remote sensing, as well as free-space optical communication and gas absorption.